A Measurement of the Quark Polarisations of the Nucleon.

Thesis submitted in accordance with the requirements of the University of Liverpool for the degree of Doctor of Philosophy

by

Michael Gabriel M^{c}Andrew

November 1999

Oliver Lodge Laboratory
University of Liverpool

A Measurement of the Quark Polarisations of the Nucleon.

Michael Gabriel M^{c}Andrew

Abstract

An analysis of the deep inelastic scattering of polarised positrons off polarised gas targets of ^{3}He, ^{1}H and ^{2}D is performed with the HERMES experiment at HERA. Spin cross section asymmetries for $e^{+(-)}$, h^+ and h^- are measured in the kinematic range $0.023 < x < 0.6$ and $1 < Q^2 < 10$ GeV^2. The polarised quark distributions $\Delta u_v(x)$, $\Delta d_v(x)$ and $\Delta\overline{u}(x)$ as a function of Bjorken x are derived from a fit to the measured spin asymmetries. The fractional contributions of these quarks to the proton spin are $\Delta u_v = 0.594 \pm 0.037 \pm 0.099$, $\Delta d_v = -0.130 \pm 0.041 \pm 0.174$, and $\Delta\overline{u} = 0.036 \pm 0.021 \pm 0.036$. This is the first such study from HERMES which uses data from a ^{2}D target.

To my parents.

Contents

Acknowledgements

If it were not for Prof. Erwin Gabathuler's encouragement to take up his offer of continuing my education at Liverpool, this PhD would not have come about. For this, and his consistent interest in both my work and welfare, I am very grateful. My passage through the PhD experience has been moderately unusual in that I spent the first year of my research overseas and the second year studying courses to prepare me for this. Without the experience and wisdom of my supervisor, Dr Geoff Court, who was always willing to listen to my "problem of the week", getting through in one piece would have been considerably tougher. I would also like to thank Jim Stewart for his friendly encouragement.

Thank you to the Particle Physics and Astronomy Research Council for the grant to cary out this PhD.

Perhaps understandably, my first few months working at the DESY laboratory were baffling to say the least. I would sincerely like to thank Kevin M^{c}Ilhany, for teaching me a huge amount in a short period of time. I shall remember with a smile our joint searches for hot curry in Hamburg.

Without a doubt my greatest thank you must go to fellow Liverpool HERMES member Hugh Tallini. Apart from burning an analysis trail for me to follow, his friendship over the last three years has been invaluable (I hope the all-nighters didn't prove too deadly).

I would like to thank all the HERMES collaborators for making working at DESY so stimulating, particularly Balijeet Bains, Antje Bruel, Holger Ihssen, Naomi Makins, Geoff Martin, Gregory Rakness and Michael Ruh. A special thank you to Mark Beckmann and Bryan Tipton for helping me with some last minute analysis issues.

And so I come to the shady bunch with whom (apparently) I spent most Friday nights with in Hamburg. Molly Anderson, Chris Cormack, Brian Cox, Kirstee Hewitt, Dave Milstead, Mark Smith, Paul Sutton and Hugh Tallini. Perhaps shady is the wrong word, perhaps the use of that word was brought on by the memory of a makeshift light shade fashioned from one of the above's undergarments during a certain 'Port and Cheese' evening, anyway thank you all for your friendship.

Thanks to Nick Malden for (just about) keeping me sane at the summer school and Gavin M^{c}Pherson for office hysteria.

I must also thank Mrs Maltan for her delicious onion bhajees and other savoury items, which have sustained me so well over the last year.

Thank you Sharon, the last few months in Liverpool with you have been the best.

This PhD would not have been possible without the love and encouragement of my parents, brother and sister. Maybe now I can begin to pay back some of the money I owe you.

Author's Contribution

The HERMES collaboration consists of over two hundred physicists working on a variety of physics programmes. The data whose analysis is presented here were collected as a collaborative effort. Other facets of the work presented in this thesis also, necessarily, rely on the efforts of other HERMES members.

The work presented in chapter 4 was conducted by me as part of my first year project and led to an improved understanding of the particle identification system, which is of vital importance in many HERMES analyses. The extraction and systematic study of the hydrogen spin asymmetries (presented in chapters 5 and 6) from the data collected in 1996 and 1997 has been my main responsibility over the last two years. A consensus was reached with other members of the semi-inclusive analysis group on the values of the asymmetries. The asymmetry results were then used as input to the, subsequently published, HERMES analysis of the quark polarisations, which had been developed in parallel by other collaborators. I have also aided in the extraction of asymmetries from the deuterium data collected in 1998 and 1999. This allowed me to perform an independent quark polarisation analysis (presented in chapter 7) where, for the first time, deuterium asymmetries were included. The measurement of the quark polarisations is the main physics goal of HERMES and the quark polarisation analysis presented in this thesis is the first to include the complete polarised data set collected up until April 1999.

As a member of the HERMES collaboration I spent time "on shift" where I was responsible for the smooth operation of the target system and beam polarimeters. While on shift I helped perform measurements that were used to study beam induced nuclear depolarisation effects in the target (see section 3.4.1), the results of which have been published. I played an active role in the semi-inclusive working group and have presented my analysis at various collaboration meetings, the Rutherford Appleton summer school and a departmental seminar.

Chapter 1

Introduction

A "Standard Model" (SM) has emerged where all matter is composed of point-like fermions which interact via the exchange of bosons. Although the SM of elementary particle interactions has endured close scrutiny for more than three decades, the theory contains many free parameters and as such is incomplete. Also, the field theories leading to the SM are too complex to solve for anything other than the simplest of interaction scenarios. Consequently, the SM has little to say about the interactions of more complex systems of fermions and bosons, such as the nucleon.

A natural way of developing this theory is to attempt to account for measurements made of the properties of larger systems of fermions and bosons. To this end the nucleon and it's structure is of prime interest in many particle physics experiments. Deep inelastic scattering (DIS) of high energy leptons off nucleons allows the internal nucleon structure to be probed. This work focuses on the nucleon spin structure, which is studied here via polarised DIS.

The complex structure of the nucleon can be understood in terms of the Quark Parton Model (QPM). The QPM interprets the spin half nucleon in terms of three constituent spin half quarks that give the nucleon its quantum numbers, embedded in a sea of quark anti-quark pairs. Whereas unpolarised DIS can be used to investigate the momentum distribution of the quarks, polarised DIS probes the spin distribution of the quarks. The QPM therefore, provides a common framework for understanding both polarised and unpolarised nucleon measurements.

The technical challenges of measuring spin structure are great and until recently, available measurements have only allowed the total nucleon spin due to quarks to be determined. The work presented here focuses on measurements that allow the contribution of each quark flavour to be ascertained.

In chapter 2 a theoretical overview of the nucleon spin structure will be presented together with how, in principle, the spin structure can be probed. The HERMES experimental setup will then be presented in chapter 3. Chapter 4 and 5 will discuss the analysis methods necessary to extract the spin asymmetries, which are presented at the end of chapter 5. Many detailed studies were performed on the extracted asymmetries to ensure no systematic effects due to the experimental apparatus were influencing the the asymmetry results. A review of these studies is presented in chapter 6. Finally, in chapter 7 the results for the quark polarisations and polarised parton densities are presented and discussed. The integrals of the polarised parton distributions are also presented in chapter 7, giving a measurement of the fraction of nucleon momenta carried different types of quark.

Chapter 2

Theory

2.1 Introduction

In the early seventies technological advances allowed the structure of the nucleon (i.e. proton and neutron) to be studied in earnest for the first time. The idea that the nucleon consisted of fractionally charged point-like partons held together by some sort of glue was not well established until 1973. Understanding the inner workings of the nucleon remains a challenge today. One of the toughest outstanding questions is "*From where does the nucleon acquire its spin?*".

In section 2.2 the formalism of high energy (deep) inelastic lepton-nucleon scattering will be introduced. The standard physical model used to interpret such lepton-nucleon reactions is reviewed in section 2.3. Section 2.4 will focus on polarised lepton-nucleon scattering, in particular how measurements of the scattered lepton (inclusive channel) are used to partially reveal the spin structure of the nucleon. Additional information on the nucleon spin structure may be gained from detecting other particles in conjunction with the scattered lepton (semi-inclusive channel). The semi-inclusive channel provides a powerful tool for the study of nucleon spin structure and is introduced in section 2.5. Finally section 2.6 relates the theoretical quantities of interest, spin structure functions, to measurable cross section asymmetries.

2.2 Deep Inelastic Scattering (DIS)

Deep Inelastic Scattering (DIS) is the study of lepton-hadron scattering with high momentum transfer ($> 1(\mathrm{GeV/c})^2$), where some of the particles in the final state differ from those in the initial state. The following sections will concentrate on lepton-nucleon DIS, i.e.

$$l + N \quad = \quad l' + X. \tag{2.1}$$

Inclusive measurements, where only the scattered lepton l' is detected and semi-inclusive measurements, where parts of the nucleon fragments are also detected, will be considered.

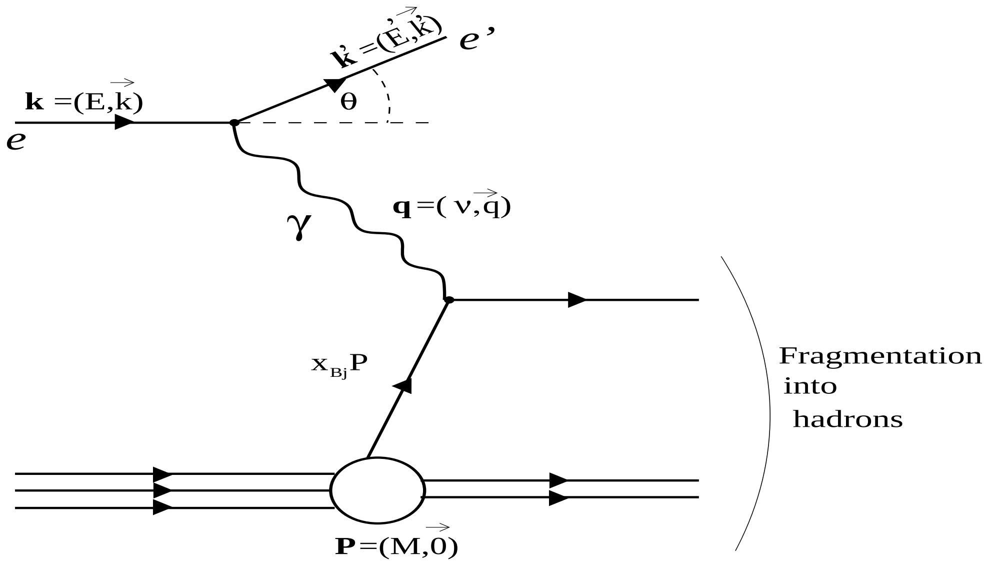

Figure 2.1: Schematic diagram of a deep inelastic scattering event.

In lowest order Quantum Electrodynamics (QED) the scattering is described by the exchange of a virtual photon. Figure 2.1 shows the deep inelastic scattering of a positron on a nucleon. The incoming positron with four-momentum $\mathbf{k}$ exchanges a virtual photon of four momentum $\mathbf{q}$ with the nucleon of four-momentum $\mathbf{P}$. The outgoing positron with four momenta $\mathbf{k}'$ is scattered by an angle θ. If the thermal motion of the target atom and the Fermi motion of the nucleons within the atom are neglected, this picture is in the rest frame of the laboratory.

The standard Lorentz-invariant inclusive DIS variables are defined below.

$$Q^2 = -\mathbf{q}^2 = -(\mathbf{k}-\mathbf{k}')^2 \quad (2.2)$$
$$\overset{\text{lab}}{=} 4EE'\sin^2\theta/2. \quad (2.3)$$

$$\nu = \frac{\mathbf{P}.\mathbf{q}}{M} \quad (2.4)$$
$$\overset{\text{lab}}{=} E - E'. \quad (2.5)$$

$$s = M^2 + 2EM + m^2. \quad (2.6)$$

$$y = \frac{\mathbf{P}.\mathbf{q}}{\mathbf{P}.\mathbf{k}} \quad (2.7)$$
$$\overset{\text{lab}}{=} \nu/E. \quad (2.8)$$

$$W^2 = (\mathbf{P}+\mathbf{q})^2 \quad (2.9)$$
$$\overset{\text{lab}}{=} M^2 + 2M\nu - Q^2. \quad (2.10)$$

where M is the rest mass of the nucleon.

$$x = -\frac{\mathbf{q}^2}{2\mathbf{P}.\mathbf{q}} \quad (2.11)$$
$$\overset{\text{lab}}{=} \frac{Q^2}{2M\nu}. \quad (2.12)$$

The amount of detail that may be resolved in the nucleon structure by the exchanged virtual photon is dependent upon its wavelength, $h/\sqrt{(Q^2+\nu)^2}$, and so the resolving power of DIS reactions increases with Q^2. ν is the absolute energy transfer from the lepton in the lab frame and s is the squared centre of mass energy. The fractional energy transfer is defined as y, and W^2 is the invariant mass of the hadronic final state. The Bjorken scaling variable x is a measure of the inelasticity in the scattering process and is discussed further in section 2.3.

2.2.1 Cross Section and Structure Functions

In QED the differential cross section, σ, for a deep inelastic reaction can be expressed in terms describing the interaction of the lepton and hadron with the exchanged virtual photon

$$\frac{d^2\sigma}{dxdy} \propto L^{\alpha\beta}W_{\alpha\beta}. \quad (2.13)$$

The lepton tensor $L^{\alpha\beta}$ is completely determined by QED, the hadronic tensor $W^{\alpha\beta}$ is not [12]. The double differential cross cross section for unpolarised DIS reactions, i.e. averaged over the spin states of the incoming and outgoing lepton, is given by

$$\frac{d^2\sigma}{dxdQ^2}(x,Q^2) = \frac{4\pi\alpha^2}{xQ^4} \left(xy^2 F_1(x,Q^2) + \left(1 - y - \tfrac{xyM}{s}\right) F_2(x,Q^2)\right), \quad (2.14)$$

where $F_{1,2}(x,Q^2)$ are the dimensionless structure functions of the nucleon. The lepton probe is assumed to be point-like and thus has no structure. The structure functions of the spatially extent nucleon must be measured as it is not yet possible to calculate them from first principles.

2.3 The Quark Parton Model (QPM)

The QPM describes the nucleon structure in terms of spin-half, point-like, quasi-free quark partons. Before delving into the formalism of the QPM, the key pieces of evidence that led to the quark parton view of the nucleon will be reviewed. The QPM interpretation of the nucleon structure functions in terms of quark number densities will then be discussed.

The nucleon structure functions only depend weakly on Q^2 in the Bjorken limit of $Q^2, \nu \to \infty$. This behaviour is known as "scaling" as one could equally say that the the structure functions are independent of the resolution of the probe. The Callan-Gross relation [1]

$$F_2(x) = 2xF_1(x), \quad (2.15)$$

for the scattering of two point-like spin half particles, was also found to be approximatly satisfied. The experimental verification of Bjorken scaling and the Callan-Gross relation in DIS gave the first compelling evidence for the existence of point-like spin $\frac{1}{2}$ quarks in the nucleon.

According to the SU(3) colour model of Gell-Mann [2], quarks carry a strong charge called colour. Isolated particles (observable in nature) must be colour-neutral. The SU(3) model interpreted mesons as quark anti-quark states while the baryons are made up of three quarks. The QPM encompasses these SU(3) ideas to form a relatively simple view of the nucleon which is also useful for explaining, at a symbolic level, the more complex quantum field theories.

In the QPM the constituent quarks which give the nucleon its quantum numbers are called *valence quarks*. In Quantum Chromodynamics (QCD), the colour charge is mediated by field bosons called *gluons*. Gluons may split into quark anti-quark pairs, which in the QPM are called *sea quarks*.

In the Bjorken limit, the Bjorken scaling variable x can be interpreted within the QPM as the fraction of the nucleon's momentum carried by the struck quark. The structure functions can then be expressed as

$$F_2(x) = 2xF_1 = \sum_q e_q^2 xq(x), \tag{2.16}$$

where q runs over all quark (anti-quark) flavours available at the given energy scale and e_q are the quark charges. The functions $q(x)$ are the number density of a quark with flavour q and momentum fraction x in the nucleon and are called Parton Density Functions (PDFs). The measured integral over all x of equation 2.16 yielded only about half the nucleon momentum [3]. In QCD the rest is assumed to be carried by gluons, which do not contribute directly to lepton-nucleon scattering as they are uncharged. The PDFs for the quarks accessible at HERMES energies are shown in figure 2.2.

Early measurements verified the Callan-Gross relation (2.15), however later results showed that the equality was not exact. In the naive QPM described above, the causes of such deviations (e.g. parton masses and transversely orientated quark spins) were neglected. The deviation is parameterised by the function $R(x, Q^2)$ and can be interpreted as the ratio of the absorption cross section for longitudinally (σ_L) and transversely (σ_T) polarised virtual photons by the nucleon:

$$R(x, Q^2) = \frac{\sigma_L}{\sigma_T} = (1+\gamma^2)\frac{F_2(x, Q^2)}{2xF_1(x, Q^2)} - 1, \tag{2.17}$$

where $\gamma^2 = \frac{Q^2}{\nu^2}$.

Precision structure function measurements show a dependence on Q^2. This scaling violation is attributed to the presence of gluons. In QCD non-scaling effects have been calculated with the Dokshitzer-Gribov-Lipatov-Altarelli-Parisi (DGLAP) equations [5, 6, 7] which are used to evolve structure functions measured at certain Q^2 to a fixed Q_0^2. However, the DGLAP equations do not predict the x dependence of the structure functions from first principles.

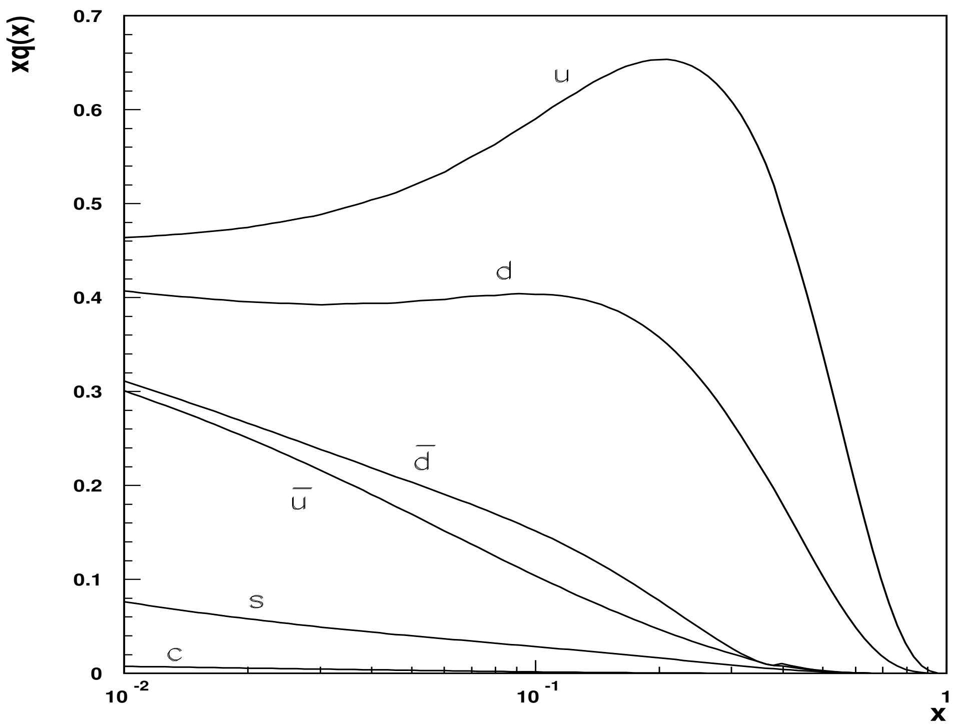

Figure 2.2: Unpolarised parton density functions. The parametrisations of data [4] were evaluated at $\langle Q^2 \rangle = 2.5$ (GeV/c)^2.

2.4 Polarised Inclusive DIS

In the case of polarised DIS where the lepton and nucleon spin orientations are specified to be either parallel ($\uparrow\uparrow$) or anti-parallel ($\uparrow\downarrow$), equation (2.14) is no longer appropriate. Instead of the spin averaged cross section, one must consider the cross section for each of the lepton-nucleon spin orientations. Taking a difference of cross sections leaves purely anti-symmetric terms and allows the spin structure to be studied:

$$\begin{aligned} \frac{d^2\sigma^{\uparrow\downarrow}}{dxdy} - \frac{d^2\sigma^{\uparrow\uparrow}}{dxdy} - \quad &= \quad \frac{8\pi\alpha^2 ME}{Q^4} \\ & \left[\left(2y - y^2 - \frac{Mxy^2}{E}\right) 2xg_1(x,Q^2) - \frac{4M}{E}x^2 y g_2(x,Q^2)\right], \end{aligned} \tag{2.18}$$

where in analogy to the structure functions $F_{1,2}(x, Q^2)$, which described the nucleons' momenta distribution, the polarised structure functions $g_{1,2}(x, Q^2)$ appear, which describe the distribution of spin in the nucleon.

To determine the polarised structure functions experimentally one measures asymmetries for two combinations of lepton-nucleon spin orientations,

$$A_{||}(x, Q^2) = \frac{d\sigma^{\uparrow\downarrow}(x, Q^2) - d\sigma^{\uparrow\uparrow}(x, Q^2)}{d\sigma^{\uparrow\downarrow}(x, Q^2) + d\sigma^{\uparrow\uparrow}(x, Q^2)},$$
$$A_{\perp}(x, Q^2) = \frac{d\sigma^{\uparrow\rightarrow}(x, Q^2) - d\sigma^{\uparrow\leftarrow}(x, Q^2)}{d\sigma^{\uparrow\rightarrow}(x, Q^2) + d\sigma^{\uparrow\leftarrow}(x, Q^2)}, \tag{2.19}$$

where $A_{\perp}$ is formed of the lepton-nucleon cross sections for transversely orientated spins ($\uparrow\leftarrow$ and $\uparrow\rightarrow$). The exchanged photon is not emitted collinear with the incoming electron, consequently measurements of $A_{||}$ or $A_{\perp}$ simultaneously probe both the longitudinal (g_1) and transverse (g_2) spin structure. The measured asymmetries are related to the virtual photon Compton scattering asymmetries $A_{1,2}$ by

$$A_{||} = D(A_1 + \eta A_2), \tag{2.20}$$

$$A_{\perp} = d(A_2 - \xi A_1). \tag{2.21}$$

Where

$$D = \frac{y(2-y)}{y^2 + 2(1-y)(1+R(x,Q^2))}, \qquad \varepsilon = \frac{1-y}{1-y+\frac{1}{2}y^2},$$
$$\gamma^2 = \frac{Q^2}{\nu^2} = \frac{4M^2x^2}{Q^2}, \qquad \eta = \frac{2\gamma(1-y)}{2-y},$$
$$d = D\sqrt{\frac{2\varepsilon}{1+\varepsilon}}, \qquad \xi = \eta\frac{1+\varepsilon}{2\varepsilon}, \tag{2.22}$$

are kinematic factors. The structure functions can now be related to A_1 and A_2 by

$$A_1 = \frac{g_1 - \gamma^2 g_2}{F_1}, \tag{2.23}$$

$$A_2 = \gamma\frac{g_1 + g_2}{F_1}. \tag{2.24}$$

In the Bjorken limit $Q^2 \to \infty$ and the kinematic factor $\gamma^2 \to 0$ as $Q^2 \gg 4M^2x^2$. Equations 2.23, 2.24 and 2.20 are used to derive an expression that relates the measured asymmetry, $A_{\|}/\mathrm{D}$, to the polarised and unpolarised structure functions, giving

$$\frac{g_1}{F_2} 2x \frac{(1+R)}{(1+\gamma^2)} \approx \frac{A_{\|}(x,Q^2)}{D(x,Q^2)} + (\gamma - \eta) A_2(x). \tag{2.25}$$

Equation (2.25) shows that g_1 may be determined from a measurement of $A_{\|}/D$, with a correction of $(\gamma - \eta)A_2$, combined with information on the unpolarised structure function F_2.

To extract the polarised structure functions some information about A_2 is required. The first measurements of A_2 from SMC [8] showed that it was consistent with zero. However, as figure 2.3 shows, recent measurements from E143 [9] and E155 [10], which are of greater statistical precision show that A_2 is small but non zero.

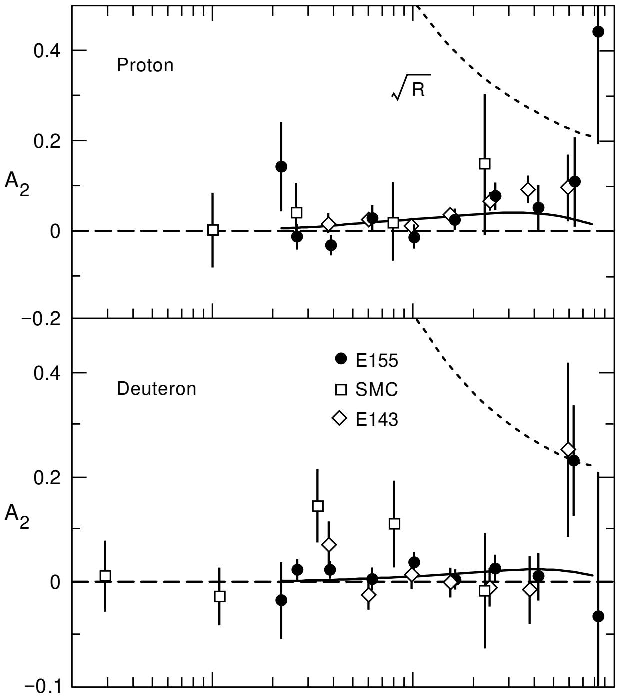

Figure 2.3: The asymmetry A_2 as measured by E155 [10], E143 [9] and SMC [8]. The solid line is a theoretical prediction (see [10] for details) and the dashed line indicates the positivity limit $\sqrt{R}$. The asymmetry and positivity limit have been evaluated at the mean Q^2 for each x bin of the E155 data.

2.4.1 QPM interpretation

The QPM can now be extended to the polarised case. The polarised PDFs $\Delta q(x)$ and the unpolarised PDFs $q(x)$ are now defined in terms of the probability that a quark spin is parallel $q^{\uparrow}(x)$ or anti-parallel $q^{\downarrow}(x)$ to the spin of the parent nucleon, such that

$$\begin{aligned} q(x) &= q^{\uparrow}(x) + q^{\downarrow}(x), \\ \Delta q(x) &= q^{\uparrow}(x) - q^{\downarrow}(x). \end{aligned} \tag{2.26}$$

The polarised structure function $g_1(x)$ is then interpreted as

$$g_1(x) = \frac{1}{2}\sum_i e_q^2 \Delta q(x). \tag{2.27}$$

2.4.2 Sum Rules

Theoretical models are unable to make precise predictions for the x dependence of the PDFs unless profound theoretical assumptions are made. Predictions do exist however for various combinations of the moments of the polarised and unpolarised PDFs. Such predictions are known as Sum Rules. By comparing a theoretical prediction with the measured value, the validity of the model used, and any assumptions made therein, is tested. The Gottfried, Bjorken and Ellis-Jaffe Sum Rules will now be discussed.

Gottfried Sum Rule

The Gottfried sum rule is important for describing the behaviour of the unpolarised sea quarks' PDFs. Assuming iso-spin symmetry, it can be derived from (2.16) and for the proton is given by

$$S_G = \int_0^1 \frac{1}{x}(F_2^p(x) - F_2^n(x))dx, \tag{2.28}$$

$$= \frac{1}{3} + \frac{2}{3}\int_0^1 (u_s(x) - d_s(x))dx. \tag{2.29}$$

S_G has a value of $\frac{1}{3}$ in the QPM. The measured value of $S_G = 0.235 \pm 0.026$ [11] shows that there is a flavour asymmetry in quark sea. The difference between $\overline{u}(x)$, $\overline{d}(x)$ and $s(x)$ distributions is also seen in figure 2.2. The cause of flavour asymmetry in the sea is not quantitatively understood at present and is presented here as it may impact on the polarised case (see section 7.3).

Bjorken Sum Rule

If only sea quarks of flavour u, d and s are considered (a good approximation at HERMES energy as figure 2.2 suggests), assuming SU(2) iso-spin symmetry allows the first moment of the inclusive structure functions g_1 to be written as

$$\Gamma_1^{p,n} = \int_0^1 g_1^{p,n} dx = \frac{1}{9}a_0 \pm \frac{1}{12}a_3 + \frac{1}{36}a_8, \tag{2.30}$$

where a_0, a_3 and a_8 are the SU(3) flavour singlet, octet isotriplet and octet isosinglet combinations of the first moments of the quark distributions [12]:

$$\begin{aligned} a_0 = &\quad \eta_u + \eta_d + \eta_s, \\ a_3 = &\quad \eta_u - \eta_d, \\ a_8 = &\quad \eta_u + \eta_d - 2\eta_s \quad , \end{aligned} \tag{2.31}$$

with the net spin carried by a particular quark flavour ($= \int_0^1 dx[\Delta q(x) + \Delta\overline{q}(x)]$) being denoted as η_q, where $q = u,d,s$.

The triplet combination a_3 is related to measurable matrix elements, g_A and g_V in neutron β-decay [13]. This allows a prediction for the difference in the first moments of the proton and neutron spin structure functions. This is known as the Bjorken sum rule, given by [14]

$$\Gamma_1^p - \Gamma_1^n = \frac{1}{6}a_3 = \frac{1}{6}\left|\frac{g_A}{g_V}\right| = 0.209 \pm 0.001. \tag{2.32}$$

In practice perturbative QCD corrections must be applied, but have been neglected here for simplicity. The Bjorken sum rule is a fundamental prediction of QCD and has been verified experimentally [15, 16].

Ellis-Jaffe Sum Rule

Values for a_3 and a_8 can be obtained from weak decays of the hyperons in the spin-$\frac{1}{2}$ octet [17]. When SU(3) flavour symmetry is assumed, the axial currents are then given by two decay constants, F and D, and have been determined experimentally as [18]

$$\begin{aligned} a_3 &= F + D = 1.257 \pm 0.003, \\ a_8 &= 3F - D = 0.58 \pm 0.02. \end{aligned} \tag{2.33}$$

If additional assumptions about a_0 are made, then separate sum rules for the proton and the neutron can be derived. Ellis and Jaffe [19] assumed that the strange quarks are unpolarised [1], $\Delta s + \Delta\overline{s} \equiv 0$, which leads to the following sum rules

$$\Gamma_1^p = \tfrac{1}{18}(9F - D) = 0.185 \pm 0.003, \quad (2.34)$$

$$\Gamma_1^n = \tfrac{1}{18}(6F - 4D) = -0.024 \pm 0.003, \quad (2.35)$$

These predictions are not in agreement with the experimental values, even after QCD corrections. The implications of this violation are discussed in section 2.4.3.

2.4.3 Implications of the Inclusive Measurements

In the Quark Parton Model the singlet combination a_0 corresponds to the fraction of the nucleon spin carried by all quarks $\Delta\Sigma$:

$$a_0 = \Delta u + \Delta\overline{u} + \Delta d + \Delta\overline{d} + \Delta s + \Delta\overline{s} = \Delta\Sigma. \quad (2.36)$$

Naively, it is reasonable to expect the nucleon's quark spins to add vectorialy, to give the nucleon its spin of $\frac{1}{2}$, so that $\Delta\Sigma = 1$.

Some of the first data from SLAC [20] on the proton structure function $g_1^p(x)$ were consistant with this naive picture. However, futher measurments from EMC [21], made over a larger x range, revealed that the Ellis-Jaffe sum rule was violated For example SMC [22] measured the the Ellis-Jaffe Sum Rule (cf. equation 2.34) to be

$$\Gamma_1^p = 0.142 \pm 0.008 \pm 0.011. \quad (2.37)$$

The discrepancy could be due to a non-zero polarisation of the strange sea quarks, and/or a broken SU(3) flavour asymmetry. Assuming the validity of the Bjorken sum rule and the predicted value of a_8 (and thus SU(3)), the contribution of each quark flavour to the nucleon spin was determined from Γ_1^p [21], giving

$$\begin{aligned} \frac{1}{2}\Delta u + \Delta\overline{u} &= 0.391 \pm 0.016 \pm 0.023 \\ \frac{1}{2}\Delta d + \Delta\overline{d} &= -0.236 \pm 0.016 \pm 0.023 \\ \frac{1}{2}\Delta s + \Delta\overline{s} &= -0.095 \pm 0.016 \pm 0.023. \end{aligned} \quad (2.38)$$

[1] The assumption, used in the derivation of the Ellis-Jaffe Sum Rule, $\Delta s + \Delta\overline{s} \equiv 0$, leads to $a_0 = a_8$. The Ellis-Jaffe assumption could be viewed as a special form of SU(3) flavour symmetry breaking for strange quarks only.

and

$$\frac{1}{2}\Delta\Sigma = +0.060 \pm 0.047 \pm 0.069. \tag{2.39}$$

This unexpected result shows that the quarks only carry a very small fraction of the nucleon spin and is often referred to as the "spin puzzle". An improved QPM allows for additional contributions to the nucleon spin $\langle s_z \rangle$ from gluons ΔG and orbital angular momentum of both quarks L_z^{q} and gluons L_z^{G} such that

$$\langle s_z \rangle = \frac{1}{2}\Delta\Sigma + \Delta G + L_z^{\mathrm{q}} + L_z^{\mathrm{G}} = \frac{1}{2}. \tag{2.40}$$

The value of ΔG is not well constrained by theoretical considerations, although recent results from HERMES [23] suggest it may be large and positive. At present no experimental technique exists to determine the role of orbital angular momentum and theoretical predictions vary widely [24, 25, 26].

Determining the contribution of different flavours to $\Delta\Sigma$ (equation 2.38) is only possible if SU(3) flavour symmetry assumptions are made. Also no information about the x dependence of the polarised PDFs is gained from inclusive DIS. The semi-inclusive channel provides additional information, which allows the quark spin structure for each flavour to be unravelled.

2.5 Semi-Inclusive DIS

A semi-inclusive DIS process, as shown in figure 2.4, can be expressed generally as

$$l + N \quad = \quad l' + h + X, \tag{2.41}$$

where N is the target nucleon, l the lepton probe, h is one or more hadrons and X is any final-state particles that were not detected. The semi-inclusive kinematic variables are defined in table 2.1

The inclusive channel is insensitive to the flavour of the struck quark, while semi-inclusive hadrons are not. The QPM interpretation of the semi-inclusive interaction shown in figure 2.4 has the virtual photon interacting with a single quark within the nucleon. In a DIS event, the energy transfer to the nucleon

Semi-Inclusive Observables		
Variable		Name
E_h		Hadron Energy
$\mathbf{p}_h$		Hadron 3-momentum
Derived Variables		
Variable	Definition	Name
z	E_h/ν	Fractional hadron energy
$\mathbf{p}_{\|\|}$	$\frac{\mathbf{p}_h \mathbf{q}}{\sqrt{\mathbf{q}^2}}$	Parallel and transverse momentum
$\mathbf{p}_T$	$\mathbf{p}_h - \mathbf{p}_{\|\|}$	of hadron in γN frame w.r.t. $\mathbf{q}$
x_F	$(2\|\mathbf{p}_{\|\|}^2\|/\sqrt{W^2})_{cm}$	Feynman's scaling variable

Table 2.1: Semi-inclusive kinematic variables.

system is sufficient to cause it to fragment into hadrons. Hadrons in the "target fragmentation region" are associated with the nucleon remnant, whereas hadrons in the "current fragmentation region" are associated with the struck quark.

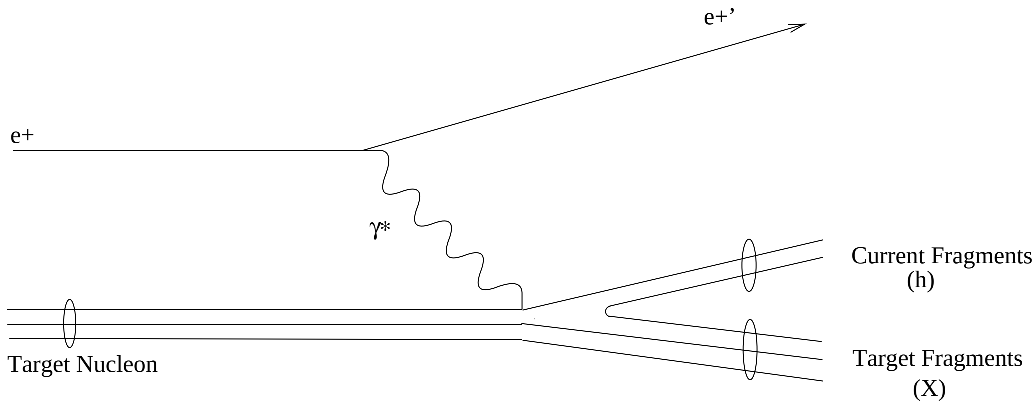

Figure 2.4: Schematic diagram of a semi-inclusive DIS event. The struck quark fragments to the 'current region', while the target remnant fragments to the 'target region'.

2.5.1 Fragmentation Functions

Fragmentation functions $D_q^h(z)$ give the probability that a struck quark of flavour q forms a hadron h with energy fraction z. Implicit to this definition is the assumption of factorisation, where the fragmentation functions are assumed to be independent of the scattering process (e.g. on x and Q^2) and are only functions of z. From the definition of the fragmentation functions it follows that the cross section for a semi-inclusive process with a hadron h in the final state is given by

$$\frac{d^3\sigma^h}{dxdQ^2dz}(x,Q^2,z) = \frac{\sum_q e_q^2 q(x) D_q^h(z)}{\sum_q e_q^2 q(x)} \frac{d^2\sigma}{dxdQ^2}(x,Q^2). \tag{2.42}$$

There are 12 fragmentation functions for the three lightest quarks to fragment into charged pions. However, this number may be reduced by applying iso-spin and charge conjugation symmetries. Such that

$$D^+(z) = D_u^{\pi^+} = D_d^{\pi^-} = D_{\bar{d}}^{\pi^+} = D_{\bar{u}}^{\pi^-}, \tag{2.43}$$
$$D^-(z) = D_d^{\pi^+} = D_u^{\pi^-} = D_{\bar{u}}^{\pi^+} = D_{\bar{d}}^{\pi^-}, \tag{2.44}$$
$$D_s(z) = D_s^{\pi^+} = D_s^{\pi^-} = D_{\bar{s}}^{\pi^+} = D_{\bar{s}}^{\pi^-}, \tag{2.45}$$

where $D^+(z)$ and $D^-(z)$ are called favoured and unfavoured fragmentation functions and $D_s(z)$ is the strange fragmentation function. Fragmentation functions have been measured by EMC [27] and by HERMES [28]. The measured ratio of unfavoured to favoured fragmentation functions η is shown in figure 2.5. This figure shows that $\eta \to 1$ as $z \to 0$. At low z the current region fragments are contaminated with the target region fragments. As the target region fragments are not correlated with the struck quark, the low z pions are equally likely to have originated from a u or d quark.

2.5.2 Fragmentation Models

The fragmentation functions are not calculable with perturbative QCD as the strong forces act at long range in the fragmentation process. To model the fragmentation, a phenomenological approach is taken that may be implemented within Monte Carlo programs. Various models exist with different physical motivations. Most models have free parameters that must be optimised to achieve good agreement with the observed data.

Independent Fragmentation Model

The independent fragmentation model [29] describes the fragmentation process as cascades of parton fragments that pick up $q\bar{q}$-pairs from the vacuum until a

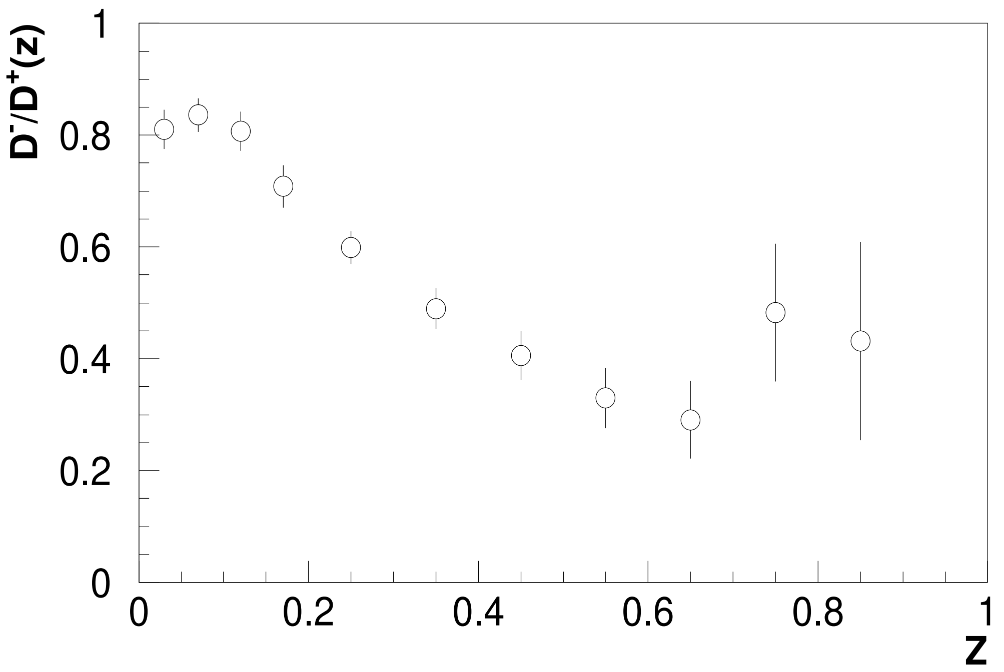

Figure 2.5: Ratio of unfavoured to favoured pion fragmentation functions as measured at EMC.

certain energy threshold is reached. It has one free parameter that controls the probability that an energy fraction z is left to the remaining cascade after $q\overline{q}$-pair produced has taken place. This early attempt to model fragmentation describes many features observed in experimental data but does not conserve all quantum numbers and is not Lorentz invariant.

The LUND String Model

The LUND string model [30] has the quarks connected via colour tubes, formed from gluons, called strings. If the energy of the string exceeds the mass of a $q\overline{q}$-pair, the pair is produced and the string is divided in two. The substrings continue to fragment independently until a hadron is produced on its mass shell. The LUND string model, as implemented in the JETSET [31] program libraries, has been used for the Monte Carlo studies in this work. It is Lorentz invariant and conserves all quantum numbers. The main tunable parameters for this model are variables controlling the string breaking probabilities and the width of the $p_\perp$ distribution. The tuning of these variables to the HERMES data is described in

[32].

The Cluster Fragmentation Model

Cluster fragmentation has the advantage that it is more theory driven and does not require ad-hoc parameterisations. However it has not yet been possible to tune this model to describe the hadron distributions observed at HERMES energies [33].

2.5.3 Semi-Inclusive Asymmetries

The formalism for the semi-inclusive asymmetries may be expressed as an extension of the inclusive case. For a semi-inclusive hadron h

$$A_{\|}^{h} = \frac{\sigma_h^{\uparrow\uparrow}(x,z) - \sigma_h^{\uparrow\downarrow}(x,z)}{\sigma_h^{\uparrow\uparrow}(x,z) + \sigma_h^{\uparrow\downarrow}(x,z)}. \tag{2.46}$$

Defining

$$g_1^h(x,z) = \frac{1}{2}\sum_q e_q^2 D_q^h(z)\Delta q(x) \tag{2.47}$$

$$F_2^h(x,z) = \sum_q e_q^2 D_q^h(z) x q(x), \tag{2.48}$$

allows the measured semi-inclusive asymmetries to be expressed in terms of the polarised and unpolarised PDFs and fragmentation functions:

$$\begin{aligned} A^h(x,z) &= \frac{A_{\|}^h(x,z)}{D} + (\gamma - \eta)A_2^h \\ &\approx \frac{g_1^h}{F_2^h} 2x \frac{(1+R)}{(1+\gamma^2)} = \frac{\sum_q e_q^2 D_q^h \Delta q(x)}{\sum_{q'} e_{q'}^2 D_{q'}^h q'(x)} \frac{(1+R)}{(1+\gamma^2)}, \end{aligned} \tag{2.49}$$

which has the same form as the inclusive case.

2.6 Purity Method for Extracting the Polarised Quark Distributions

Equation (2.49) can be written as

$$A^h(x,z) = \frac{(1+R)}{(1+\gamma^2)} \sum_q \frac{e_q^2 D_q^h(z) q(x)}{\sum_{q'} e_{q'}^2 D_{q'}^h(z) q'(x)} \frac{\Delta q(x)}{q(x)}, \tag{2.50}$$

which leads to the definition of the hadron "purity" $P_q^h(x,z)$ as

$$P_q^h(x,z) = \frac{e_q^2 D_q^h(z) q(x)}{\sum_{q'} e_{q'}^2 D_{q'}^h(z) q'(x)}. \tag{2.51}$$

The measured asymmetries may now be related to the ratio of polarised to unpolarised PDFs [2] as a linear combination of each flavour:

$$A^h(x,z) = \frac{(1+R)}{(1+\gamma^2)} \sum_q P_q^h(x,z) \frac{\Delta q(x)}{q(x)}. \tag{2.52}$$

The inclusive channel is included in this formalism by defining a pseudo-purity $P_q^{e^+}$, with $D_q^{e^-} \equiv 1$.

If a combination of asymmetries are measured, a system of coupled equations may be defined

$$\mathbf{A} = \frac{(1+R)}{(1+\gamma^2)} \mathbf{PQ}, \tag{2.53}$$

for each measured bin, where

$$\mathbf{A} = \begin{pmatrix} A^{h_1}(x) \\ \vdots \\ A^{h_m}(x) \end{pmatrix}, \mathbf{Q} = \begin{pmatrix} \Delta q_1(x)/q_1(x) \\ \vdots \\ \Delta q_n(x)/q_n(x) \end{pmatrix}, \mathbf{P} = \begin{pmatrix} P_{q_1}^{h_1}(x) & \ldots & P_{q_n}^{h_1}(x) \\ \vdots & & \vdots \\ P_{q_1}^{h_m}(x) & \ldots & P_{q_n}^{h_m}(x) \end{pmatrix}, \tag{2.54}$$

Here $\mathbf{A}$ is a vector formed from the measured particle asymmetries, $\mathbf{Q}$ is a vector of quark polarisations for various flavours and $\mathbf{P}$ is the purity matrix. The quark polarisations are obtained by inverting equation 2.53. If there are more measured asymmetries than quark flavours, then 2.53 is over-determined and can be solved for the quark polarisations by minimising

$$\chi^2 = (\mathbf{A} - \frac{(1+R)}{(1+\gamma^2)} \mathbf{PQ})^T C_A^{-1} (\mathbf{A} - \frac{(1+R)}{(1+\gamma^2)} \mathbf{PQ}), \tag{2.55}$$

where the covariance matrix $[\mathbf{C}_A]_{ij} = Cov(\mathbf{A_i}, \mathbf{A_j})$ is introduced to account for correlations between the particle asymmetries and their errors (see Appendix A for further information).

In chapter 7 this method is used to extract the quark polarisations from asymmetries measured at HERMES with purities determined from Monte Carlo simulation.

[2] In this thesis the ratio $\Delta q(x)/q(x)$ will be referred to as the quark polarisation.

2.7 Summary

In this chapter the origin of the nucleon's spin was discussed in terms of the Quark Parton Model. Sum rules for the moments of the spin structure functions provide powerful tests of the underlying theories and show that the simple Quark Parton Model picture of the nucleon does not describe the spin structure adequately. The semi-inclusive channel allows a deeper investigation of the nucleon spin structure than is possible from the inclusive channel alone. In this thesis the purity method will be used to determine the x dependence of the nucleon's spin structure for valence and sea quarks of different flavours.

Chapter 3

HERA and the HERMES Experiment

3.1 Introduction

The measurement of spin dependent cross sections of the nucleon require both nucleon and leptonic probe to be polarised. Access to the largest possible kinematic region, for the beam energies currently available, could be achieved by colliding a beam of polarised leptons off a beam of polarised protons or neutrons. A major obstacle prevents this however. The delivery of a high intensity beam of neutrons is practically impossible due to the short life time of free neutrons (about 9 minutes). Work on polarising a proton beam is well underway [34] [35], but at present no facility exists with both polarised lepton and proton beams. These restrictions necessitate the use of polarised lepton beams on polarised fixed targets. The DESY laboratory, situated in Hamburg, Germany, has a suitable polarised lepton beam.

The HERA positron-proton collider forms a major part of the DESY complex. The HERA machine accelerates a 27.5 GeV beam of positrons (or electrons) in a clockwise direction around a ring with a circumference of 6.3 km. The 820 GeV proton beam is also situated within the HERA tunnel and circulates in a counter-clockwise direction. Four experiments use the HERA accelerator, as shown in figure 3.1. The H1 and ZEUS experiments are situated at the North and South experimental Halls respectively, where the beams are brought into collision. HERA-B (West Hall) and HERMES (East Hall) are fixed target experiments and only require the proton and positron beams respectively for their physics programmes. This chapter summarises the operation of the HERA positron beam, beam polarimeters, the HERMES polarised targets and the HERMES spectrometer.

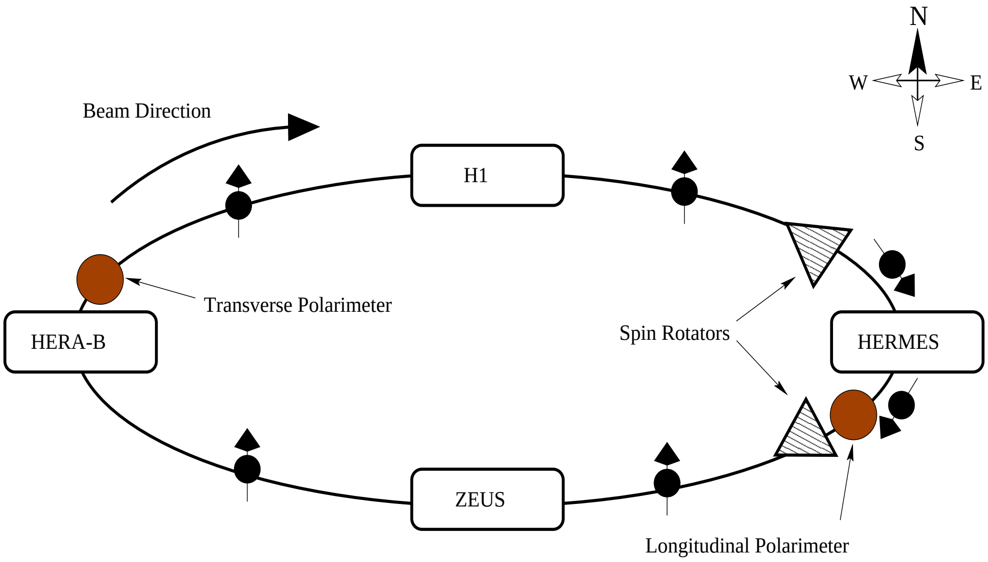

Figure 3.1: Layout of the HERA positron/electron storage ring. The HERMES experiment and longitudinal polarimeter are situated in the East. Spin rotators cause the beam polarisation to be orientated longitudinally to the beam momentum at the HERMES beam-target interaction point. The unpolarised proton beam which also resides in the HERA tunnel is not shown.

3.2 The HERA Polarised Positron/Electron Beam

The HERA machine has been used to accelerate both positrons and electrons (see figure 3.1). Whether positrons or electrons are used makes no difference to the leading order physics processes studied at HERMES and hereinafter both will be referred to as positrons unless explicitly stated.

The HERA stored positron beam becomes transversely polarised via the Sokolov-Ternov effect [36]: the accelerated positrons' synchrotron radiation emission process contains a small asymmetric spin-flip amplitude that enhances the

Beam Parameters				
Quantity	1995	1996	1997	1998
particle	e^+	e^+	e^+	e^-
I_{max}	35 mA	35 mA	40 mA	28 mA
time constant	8 h	9 h	9 h	6 h
Helicity at IP	+1	+1	both	-1

Table 3.1: Summary of positron beam parameters since 1995.

polarisation state anti-parallel to the magnetic fields of the bending magnets. The polarisation of the beam builds up due to this process with a time constant of about 40 minutes (see figure 3.2). Theoretically, polarisations of 92.4% are possible at HERA. In practice, due to factors such as the presence of spin rotators (see below) and machine imperfections, the maximum polarisation is typically about $P_{beam} = 60\%$. The positron spin orientation is rotated from the transverse direction to be either parallel or anti-parallel to the beam momentum (i.e. the helicity is chosen to be either +1 or -1) before reaching the HERMES target. This is achieved via a series of dipole bending magnets known as a *spin rotator*. Upon leaving the HERMES interaction region the spin is rotated back to the transverse orientation using the same technique.

The HERA positron beam consists of 220 bunches with a length of 27 ps, these are separated by a time interval of 96 ns. The beam cross section at the HERMES target region is elliptical with a height of 0.07 mm and a width of 0.31 mm. The current after injection is typically 35-40 mA. The current decays over a number of hours due to beam loss processes such as interactions with residual gas in the ring vacuum. To optimise luminosity for the collider experiments the beam is dumped once the current has fallen to about 10 mA and a new fill injected [37].

3.3 The Beam Polarimeters

To determine the transverse beam polarisation a transverse polarimeter (TPOL) situated in the HERA West Hall is used. Since 1997 a longitudinal polarimeter (LPOL), situated 50 m downstream from the HERMES interaction point between the spin rotators, is also used. Both are Compton-laser polarimeters which utilise the spin-dependent cross section for Compton scattering of circularly polarised photons on positrons [38].

The TPOL measures the backscattered photon up-down asymmetry in a position sensitive calorimeter. The up-down asymmetry is due to an azimuthal dependence of the photons scattering angle which is proportional to the positron beam polarisation. The measurement of the longitudinal polarisation (by the LPOL) is based on the asymmetry in the energy distribution of the scattered photons. The energy weighted spin asymmetry is then used to deduce the longitudinal polarisation.

The polarimeters are calibrated from studies of the rise in beam polarisation over time. The polarisation rise-time constant is determined with the spin rotators turned off, so that the depolarising effects are smaller. The Sokolov-Ternov equations and the rise-time constant are used to predict the polarisation of the beam over time. This provides an independent measurement with which the polarimeters are calibrated [40, 64].

The sources of systematic error for the TPOL and LPOL are quite different due to their different measuring requirements. Combining the measurements of both polarimeters reduces the systematic error on the final physics results substantially. Using both polarimeters in conjunction with each other allows the effect of the spin rotators on the beam particle's spin orientation to be determined.

3.4 The Gaseous Target

The HERMES gaseous storage cell target is situated within the positron storage ring, 80 cm upstream of the first spectrometer components. Since 1995 HERMES has collected mostly polarised data with various target gases. The sources and monitoring techniques required for each of the polarised target gases are summarised in table 3.2. The fluxes obtainable from sources of polarised gaseous atoms are insufficient to supply a usefully dense target as a free beam. The windowless storage cell technique solves this problem by confining the gas to the region of the beam and is a common element of all the polarised targets.

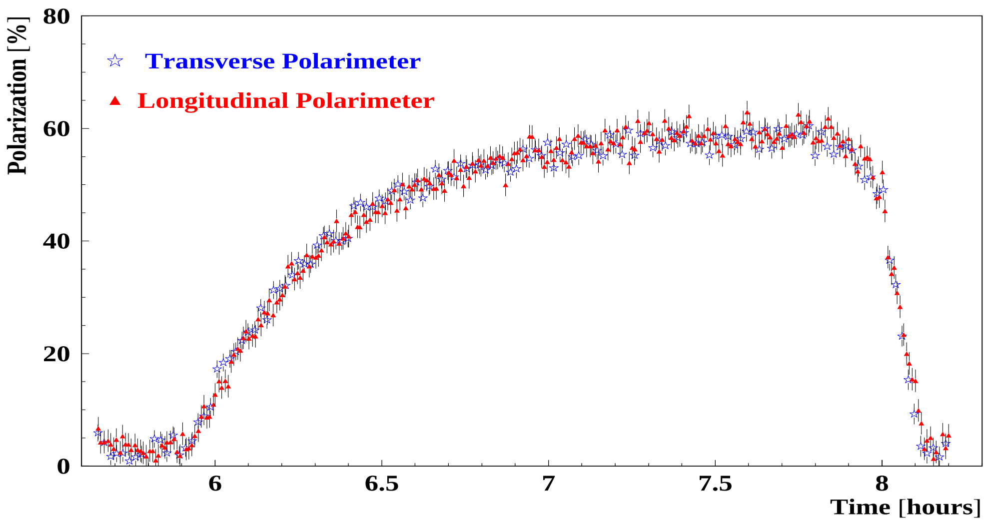

Figure 3.2: Typical build up of positron beam polarisation over the course of an accelerator fill, as measured by the longitudinal and transverse polarimeters.

3.4.1 The Storage Cells

The storage cell is mounted coaxially to the positron beam within the target chamber as shown in figure 3.3. The design of the cell increases the target thickness by about a factor of 100 [43] while allowing beam particles that do not interact with the target gas to pass through the target region and continue round the storage ring. Two collimators, C1 and C2, are positioned 2 m upstream of the target chamber and at the upstream end of the target chamber respectively. C1 shields C2 from direct synchrotron radiation and C2 shields the target cell from any indirect synchrotron radiation scattered off C1 [45]. To minimise multiple scattering from the target structure, the cell is made of 100 μm thick aluminium.

To reduce "wake field" effects [39] caused by the beam bunches passing through an abrupt change in the cross section of the beam enclosure, the gaps between C2 and the upstream end of the cell, and the downstream beam-pipe and the downstream end of the cell, are bridged by "wake field suppressors" [32]. The design of the wake field suppressors also minimises the thermal contact between the cell and collimator/beam pipe, in order to prevent heating of the cooled cell (see below).

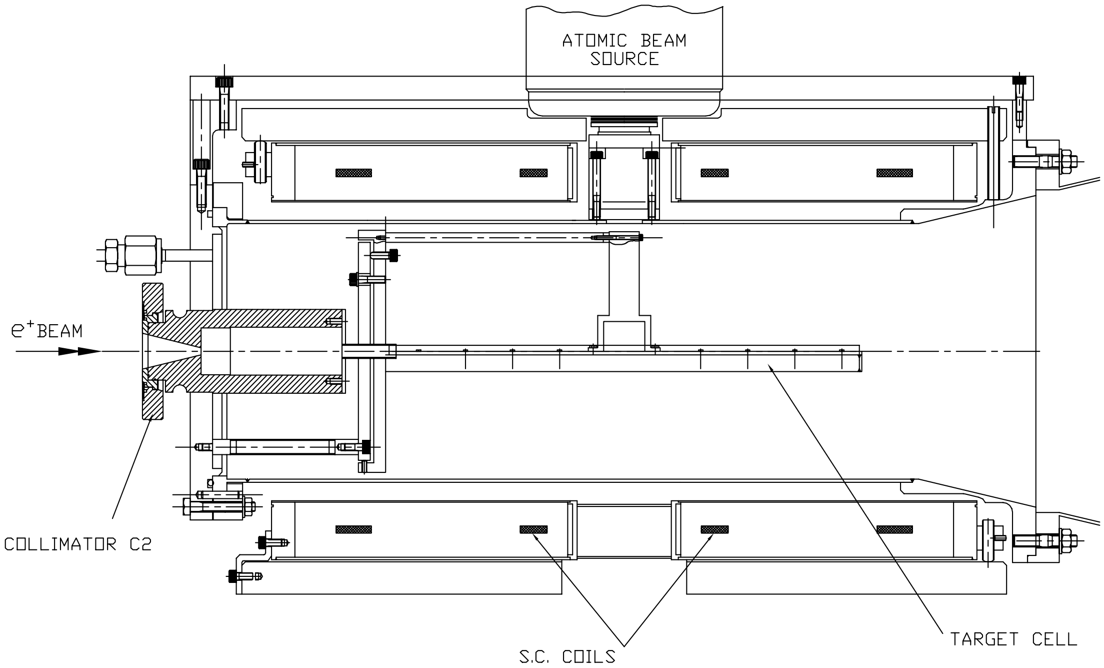

Figure 3.3: Layout of the HERMES target chamber. The target cell is 200 mm in length. For the ^{3}He target an optical pumping method, rather than an atomic beam, was used for the polarised source.

The Polarised Targets			
Gas	^{3}He	^{1}H	^{2}D
Year of operation	1995	1996/ 1997	1998
Source Working Principle	Optical Pumping	Stern-Gerlach Separation	
Source Flux (atoms/s)	$1 \cdot 10^{17}$	$6 \cdot 10^{16}$	$5 \cdot 10^{16}$
Target Thickness	$1 \cdot 10^{15}$ nucleons/cm^2	$3.5 \cdot 10^{14}$ atoms/cm^2	$7.0 \cdot 10^{14}$ atoms/cm^2
Polarimeter	Optical	Breit-Rabi	
Nuclear Pol. (%)	46	92	94
Cell Temperature (K)	15	100	85
Holding Field (mT)	3.2	335	335
Spin Flip Interval (s)	600	45	
Cell Coating	-	Drifilm	

Table 3.2: Summary of the properties of the polarised gaseous target since 1995. See text for explanation.

The Hydrogen and Deuterium Cells

The hydrogen and deuterium storage cell is a 29×9.8 mm elliptical tube, 400 mm in length. figure 3.4 shows the hydrogen cell. Polarised gas from the source is injected into the cell at the middle of its length and diffuses out to the ends where it is removed from the beam ring vacuum by a high capacity differential pumping system. The number of molecules in the cell must be minimised as the molecular polarisation is not measured directly. The injected atoms can recombine at the surface of the cell, so its surface is coated in a layer of inert plastic material [48]; this reduces the possibility of recombination. The cell is cooled, using helium gas as the cooling agent, to increase the target thickness which increases as $1/\sqrt{T}$. As recombination is enhanced at low temperatures, an optimum temperature of 100 K is chosen which maximises target density while minimising recombination.

A static holding field over the effective target volume provides a quantisation axis for the nuclear polarisation. Depolarisation effects can take place if transient magnetic fields generated by the beam pulse structure interact with the hyperfine structure of the polarised atoms and change their spin state. This resonant effect is greatest when the frequency of any large amplitude harmonic in the frequency spectrum of the magnetic field produced by the beam pulse structure coincides with an atomic hyperfine transition. The atom's hyperfine transition frequency

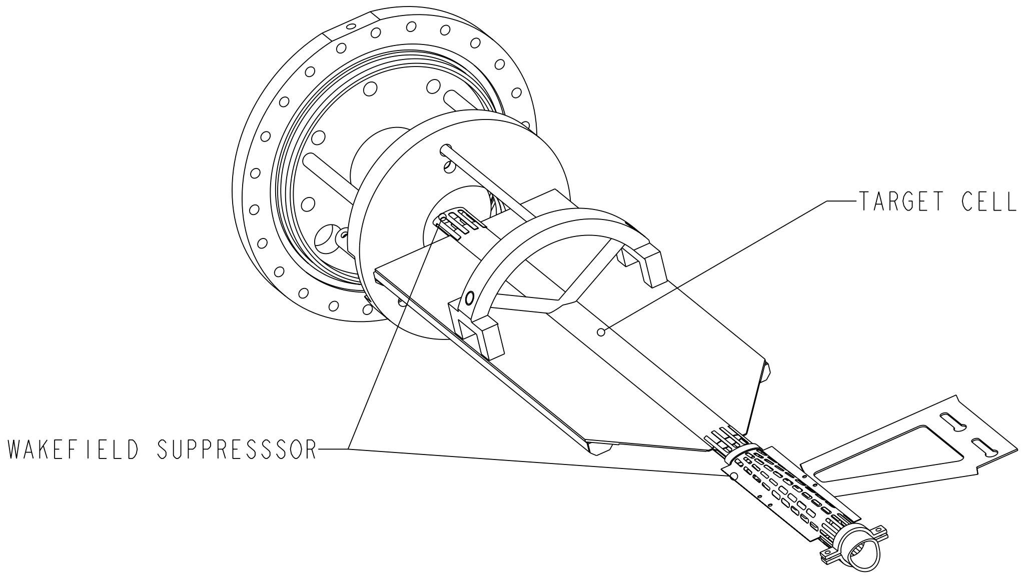

Figure 3.4: The Hydrogen target cell with the wake field suppressors shown in position. The target cell and mounting flange pictured here are inserted into the target chamber enclosure. The cell cooling rails and the inlet and outlet tubes for the polarised source and polarimeter can also be seen.

is a function of the static field strength. To minimise depolarisation effects it is therefore necessary to provide homogeneous static magnetic field conditions which ensure that no such resonant effects occur. Measurements have shown that 335 mT is a suitable choice for the static holding field in the HERMES hydrogen and deuterium targets [37]. With this setting, no depolarisation effects are observed. The holding field is provided by a super conducting magnet, as shown in figure 3.3.

The ^{3}He Cell

The operation of the ^{3}He target is different because the ^{3}He atoms contain two paired electrons. This allows the target density to be optimised by cooling the cell to 15 K. Temperatures below this are avoided as nuclear depolarisation, due to collisions with the cell walls, becomes significant. Depolarisation effects due to transient beam fields are also much smaller in ^{3}He as there is no atomic magnetic moment. Therefore a 3.2 mT magnetic holding field, produced with a pair Helmholtz coils, is adequate to define the spin orientation.

3.4.2 The Atomic Beam Source for Polarised H and D.

The polarised hydrogen (deuterium) source is based on the Stern-Gerlach separation of dissociated hydrogen (deuterium) beams. The Atomic Beam Source (ABS) uses a sextupole magnet system to select particular electron spin states. Radio frequency (RF) fields induce transitions of the hyperfine states such that the required nuclear state is populated.

Atoms from the ABS are injected into the cell at a point equidistant from the ends. The orientation of the polarisation axis may be flipped rapidly by selecting a different series of RF transitions. So as to impose a minimal systematic bias on the data the orientation of the polarisation was selected randomly.

3.4.3 The Polarised ^{3}He Source

The ^{3}He source utilises the optical pumping technique to produce a much higher flux of polarised atoms than is possible with the ABS. In practice the ^{3}He flux used is limited to $1 \cdot 10^{17}$ atoms/s so as to provide a target density that will not have severely adverse effect on the beam lifetime.

The polarised ^{3}He source consists of a pumping cell where an electrical discharge is used to convert a small fraction of atoms to a meta-stable state (2^3S_1). The atoms are then excited to a 2^3P_0 state by optically pumping them with circularly polarised light, the direction of which determines the orientation of the polarisation. The atoms become polarised as they radiate a photon and return to the 2^3S_1 state, due to angular momentum conservation. Polarisation is then transfered, through meta-stability exchange collisions, to the ground state. The polarisation axis is reversed every 10 minutes by reversing the direction of the circularly polarised light in the pumping cell.

3.4.4 The ^{3}He Target Monitors

The Pumping Cell Polarimeter (PCP)

The PCP measures the polarisation of the ^{3}He atoms in the pumping cell. Deexciting ^{3}He atoms emit circularly polarised photons with a wavelength of 667 nm. The nuclear polarisation is then obtained from measurements of the degree of circular polarisation (with the PCP having been calibrated previously)[42].

The Target Optical Monitor (TOM)

The TOM provides an independent measurement of the ^{3}He atoms polarisation inside the storage cell. Atoms excited by the HERA beam, emitting circularly polarised light as they de-excite. The light is directed by mirrors to an polarisation analyser. As for the PCP the degree of circularly polarisation is related to the nuclear polarisation.

No significant differences between the PCP and TOM measurements have been observed, confirming that beam depolarisation and cell wall collisions are negligible.

3.4.5 The Hydrogen and Deuterium Target Monitors

The Breit-Rabi Polarimeter (BRP)

A BRP is used to determine the atomic polarisation of the hydrogen and deuterium targets. Gas is sampled through a tube mounted off-axis to the ABS injection tube so that no atoms enter the BRP directly from the ABS. A combination of RF transitions and sextupole magnets differentiate atoms with different electron or nuclear polarisation states. The occupancy of selected states is then counted with a mass spectrometer. With 60 s sampling time a statistical accuracy of about 0.01% can be achieved [43]; this allows changes in the target polarisation to be monitored in real time.

The Target Gas Analyser (TGA)

The fraction of atoms contained in a molecular form within the target cell is measured with the TGA. The ratio of molecules to atoms is determined by mass spectroscopy of the target gas taken from the Breit-Rabi polarimeter's sampling tube. This information is used to determine the final target polarisation.

3.5 The Spectrometer

The HERMES spectrometer is required to have an acceptance that covers inclusive and semi-inclusive processes. A wide angle "forward" spectrometer, positioned downstream of the target, is sufficient to cover the kinematic region of interest as the scattered positron and target fragments are Lorentz boosted in the direction of the incoming positron momenta.

In this chapter the working principles of the spectrometer, which has unique Particle Identification (PID) capabilities, will be summarised. The details are described elsewhere [45, 46]. The algorithms used to determine the identity of particles are discussed in chapter 4.

Both the positron *and* proton beams unavoidably pass through the HERMES spectrometer. At the East Hall the proton beam is displaced by only 714 mm (in the machine plane) from the positron beam. The beam lines are shielded from the spectrometer's magnetic field by an iron septum plate containing coils that compensate for the residual magnetic field inside the iron. The spectrometer is consequently split into two identical halfs positioned above and below the septum plate.

The layout of the HERMES spectrometer is shown in figure 3.5. Here the spectrometer is considered in three parts. The region in front of the spectrometer magnet (*front region*) contains tracking chambers. The *magnet region* contains the spectrometer magnet and magnet proportional chambers. The *back region* contains the PID detectors, some of which are used to form the DIS event trigger, as well as further tracking chambers.

3.5.1 The Spectrometer Magnet and Tracking System

The HERMES spectrometer magnet is used in conjunction with particle tracking systems to determine the momenta of charged tracks. The dipole magnet produces a 1.3 T·m field which varies less than 10% within the acceptance. Field clamps ensure that the magnetic field in the drift chambers adjacent to the magnet, which rely on their own internal electromagnetic field, is below 0.1 T·m. The gap between the magnet's tapered pole faces encloses the geometrical acceptance

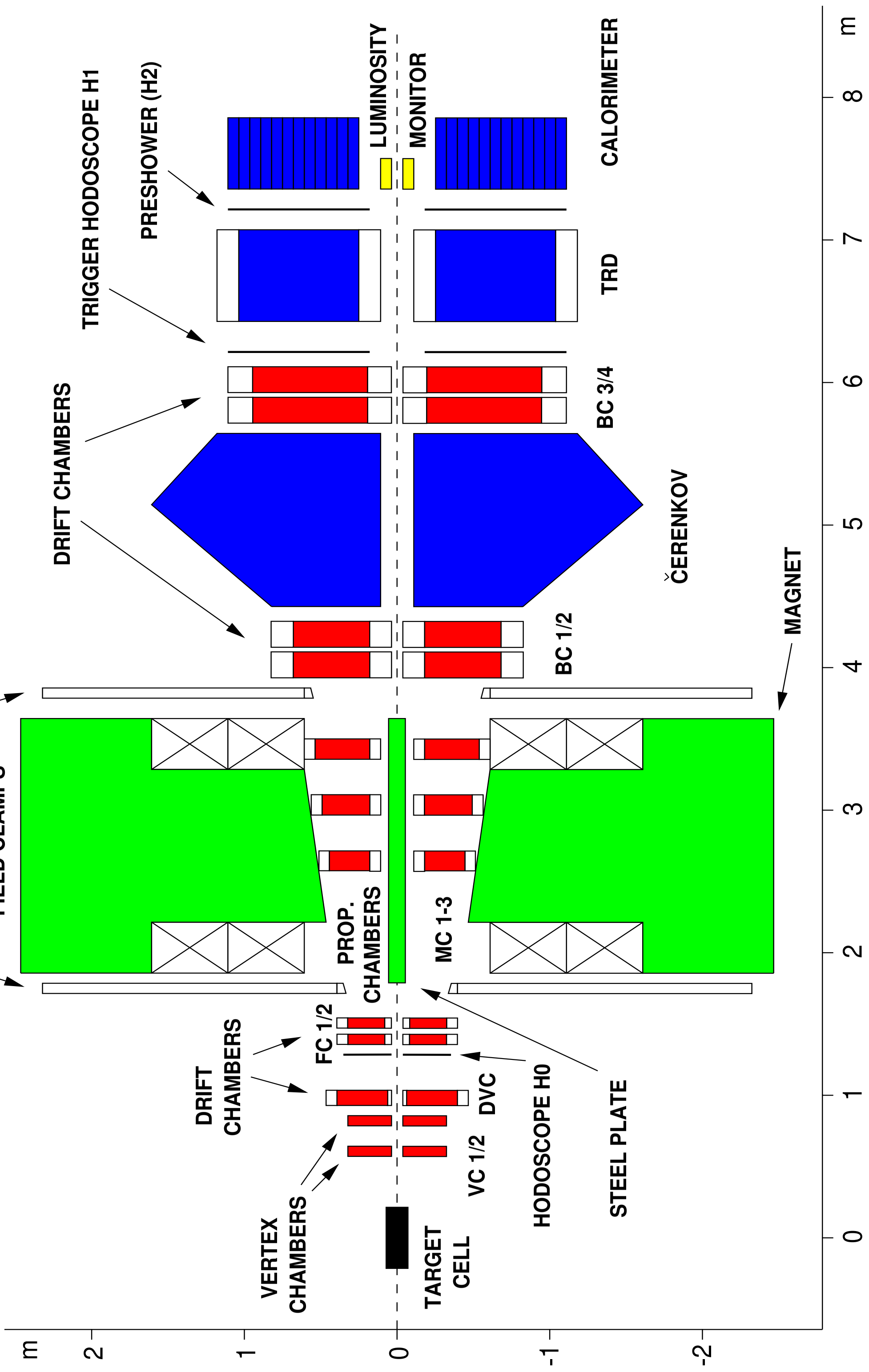

Figure 3.5: Side view cross section of the HERMES spectrometer.

of $\pm(40..140)$ and $\pm(270)$ mrad in the vertical and horizontal plane respectively. The minimum horizontal acceptance is determined by the septum plate.

The tracking system serves several functions:

- To determine the event vertex.
- To measure the scattering angles for kinematic reconstruction.
- To measuring charged particle momenta from their deflection in the magnet field.
- To identify which hits in the PID detectors are associated with each track.

Vertex reconstruction and definition of the scattering angles in the front region is determined using information from the microstrip gas counters (VC1/2), drift vertex chambers (DVC) and front drift chambers (FC). The event vertex is needed to discriminate against events not originating from within the target cell.

The role of the tracking chambers in the back region is to measure the deflection of tracks that have passed through the magnetic field and associate cells in the PID detectors with each track. Back drift chambers (BC) are used for both these roles. The magnet chambers (MC) match tracks in the forward and back regions and are used to reconstruct low momenta tracks that are deflected out of the acceptance before entering the back region.

The ability of the spectrometer to resolve particles' momentum and scattering angles determines the resolution of the physics quantities of interest. Typical values for HERMES data, deduced from Monte Carlo studies, are given in table 3.3.

3.5.2 The Particle Identification Detectors

The PID system consists of four sub-systems: a threshold Čerenkov detector, a transition radiation detector, two plastic scintillator hodoscopes, one of which is preceded by two radiation lengths of lead and acts as a preshower detector and a lead glass calorimeter (see figure 3.5). The threshold Čerenkov detector was upgraded to a Ring Imaging Čerenkov (RICH) in 1998.

Typical e^+ resolutions		
Quantity	Resolution	Units
ΔP/P	0.01	-
$\Delta\Theta$	0.4	mrad
$\Delta x_{Bj}/x_{Bj}$	0.06	-
$\Delta Q^2/Q^2$	0.02	-

Table 3.3: Typical e^+ resolutions achieved with the HERMES spectrometer for a similar data set as that used in the analysis presented in chapter 5.

Čerenkov Detector

Pion identification is provided by a threshold Čerenkov counter. Charged particles produce Čerenkov radiation if their velocity in the detector's radiator is greater than the speed of light. Therefore, the Čerenkov counter gives a measurement of β (=v/c).

An array of 20 spherical mirrors mounted at the rear of the detector focuses the Čerenkov light onto a corresponding array of phototubes, which are fitted with Winston light cones [46] to maximise light collection. In the 1995 run, the radiator was pure nitrogen which gave a pion identification threshold of 5.8 GeV. In 1996-97, a gas mixture of 70% nitrogen and 30% perfluorobutane (C_4F_{10}) was used and the pion identification threshold was 3.6 GeV.

Figure 3.6a shows the distribution of the number of photoelectrons recorded per track for a sample of data taken in 1997. The main features of this distribution are:

- As the momentum threshold for triggering is dependent on the mass of the particle, the peak at zero is predominantly due to hadrons with velocities less than the threshold.
- Above 0.25 photoelectrons the distribution is mainly due to positrons.
- The hadrons producing more than 0.15 photoelectrons are identified as pions if their momentum lies between the Čerenkov threshold for pions and kaons (5.6 – 19.8 in 1995 and 3.6 – 13.6 GeV since 1996).

Transition Radiation Detector

Downstream of the Čerenkov detector is a Transition Radiation Detector (TRD). This detector helps distinguish leptons from hadrons. In the HERMES energy regime only positrons produce transition radiation (X-rays) as they cross interfaces within the TRD of media with different dielectric properties [46]. The TRD is sensitive to the particles Lorentz factor γ $(= 1/(\sqrt{1-(v/c)^2}))$. The presence of, distinctively high energy, transition radiation is used to separate positrons from hadrons.

The TRD consists of 6 modules both above and below the beam line. Each module contains a polythene radiator and Xe/CH_4 filled proportional wire chamber. A potential of +3100 V is applied to the anode wires, with the cathodes at ground potential, to produce an electric field of sufficient strength to collect the ionisation electrons within the 1 μs gate of the readout electronics.

Figure 3.6b shows the distribution of transition radiation energy detected for a set of tracks in 1997. The important features of the TRD response distribution are:

- The intensity of the detected transition radiation is dependent on γ, thereby giving a measurement independent of the Čerenkov detector.
- The peak at 15 Kev is due to hadrons, with positrons forming a wider overlying distribution centred above this value.

Preshower Detector

A preshower counter aids in the separation of positrons from hadrons. It consists of an 11mm thick sheet of lead in front of 84 vertical plastic scintillator modules. The leptons develop large showers in the lead and consequently their photonic signature in the hodoscope is generally greater than the hadrons. Hadrons have a longer radiation length and only deposit the minimum ionising energy in the scintillator. Transitions in the scintillator molecule's energy levels, cause the production of photons of visible wavelength. The visible photons travel to a photo-multiplier tube (PMT) by way of a light guide.

Figure 3.6c shows the distribution of energy recorded in the preshower detector for a sample of tracks from the 1997 data. Important features are:

- The peak of the distribution at very low energy (2 Mev) is due to minimum ionising hadrons.
- Positrons develop large showers in the lead, producing a higher energy electro-magnetic signature in the hodoscope.

Electromagnetic Calorimeter

The lead-glass calorimeter is the furthest downstream of all the components in the spectrometer. It provides information that helps separate positrons from hadrons and forms part of the first level trigger (see section 3.6.1). When the positrons finally reach the calorimeter they deposit essentially all their kinetic energy in the form of detectable radiation. Hadrons may have strong interactions with the nuclei of the calorimeter, in this case only a fraction of the energy deposited is in a detectable form.

The electromagnetic calorimeter consists of 420 lead-glass blocks positioned both above and below the beam line. PMTs are used to detect the radiation and form a signal. The energy resolution has been measured to be σ(E)/E[%] $=(5.1 \pm 1.1)/\sqrt{(E[GeV])} \bigoplus (1.5 \pm 0.5)$.

The calorimeter alone does not clearly distinguish positrons and hadrons as both deposit a range of energies. However, positrons and hadrons do deposit a different *fraction* of their total energy in a detectable form, a better distinction of particle type is made from the particle's deposited energy divided by the momentum.

Figure 3.6d shows the ratio of energy deposited in the calorimeter divided by the tracks momentum for tracks in the 1997 data. Important features are:

- Positrons form a peak in the region where the ratio is equal to one, hadrons have mostly lower values.
- Values of the ratio greater than one are due to the finite resolution spectrometer.

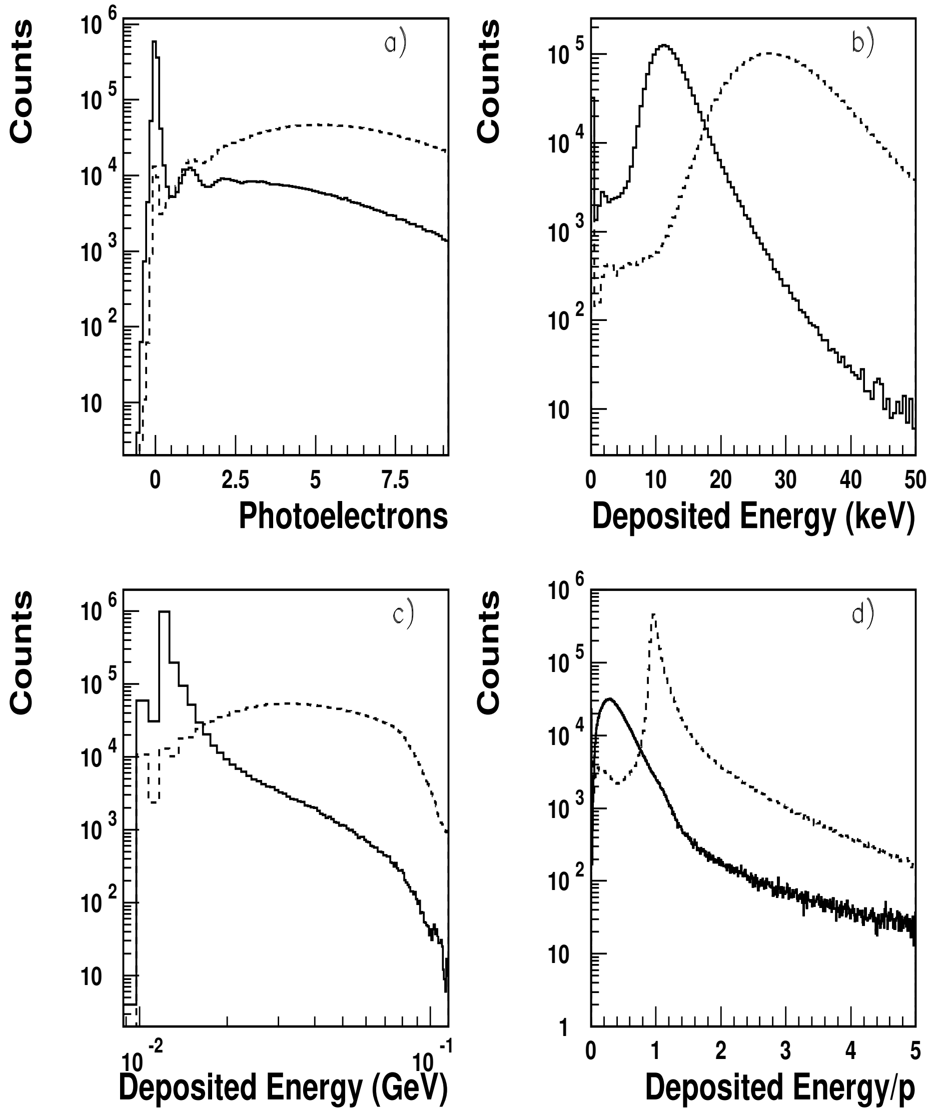

Figure 3.6: Responses of the PID detectors to identified hadrons (full line) and positrons (dashed line) from the 1997 data. a)Top left, number of recorded photoelectrons in the Čerenkov detector. b) Top right, Energy of the TRD signal. c) Bottom left, energy deposited in the Preshower detector. d) Bottom right, energy deposited in the calorimeter divided by momentum.

3.5.3 The Luminosity Monitor

The HERMES luminosity measurement is obtained by monitoring the rate of Bhabba/Möller scattering ($e^+e^- \rightarrow e^+e^-$) and annihilation interactions ($e^+e^- \rightarrow \gamma\gamma$) between the beam positrons/electrons and target electrons. The rates of these reactions are precisely calculated using Quantum Electrodynamics. The measured rates can therefore be used to calculate the absolute lumininosity. However, for spin asymmetry measurements only the relative lumininosity in each spin state is required.

The measurement of the interaction rates discussed above is performed with two radiation hard calorimeters, placed either side of the beam in the horizontal plane, 7.2 meters downstream of the target cell. The calorimeter consists $22 \times 22 \times 200$ mm^3 Čerenkov crystals made of NaBi$(WO_4)_2$ with photomultiplier tubes to detect the emitted light. Requiring coincident signals in each calorimeter reduced unwanted background.

3.6 Data Acquisition

3.6.1 The Trigger

The role of the physics trigger is to determine when a DIS event has occurred in order that it may be read out and recorded. To prevent false triggers from unwanted (mostly hadronic) background, hits are required in the three scintillator hodoscopes H0, H1 and H2 (only H1 and H2 in 1995), together with a set minimum energy deposited in two adjacent columns of the calorimeter. The background is also reduced by placing a time window on the trigger which requires that bunches of beam positrons are traversing the experiment.

In 1995 the energy threshold in the calorimeter for triggering was 3.5 GeV, in subsequent years the calorimeter energy threshold was lowered to 1.4 Gev to improve the acceptance for semi-inclusive particles. The trigger rate at typical luminosities of 5×10^{32} nucleons/cm^2/sec is about 50 Hz

3.6.2 The Data Acquisition System

The Data Acquisition System (DAQ) reads out information from the numerous experimental subsystems and directs the data on to permanent storage media. A system of readout electronics and interfaces process the data so that the information may be collated on a local work station.

As well as event by event information, so called "*slow control*" information is gathered. The slow control contains information, such as the target and beam polarisation, which is used to monitor the performance of the experiment. Slow control variables are assumed to be constant over the period of a few seconds called a burst. After about 10 minutes of bursts have been collected, a file called a "*run*" is produced, which is written to magnetic tape.

Data Production

Once the data have been recorded the information for each run is decoded and reconstructed before being stored as Data Summary Tapes (DSTs). The slow control information is processed in parallel and put into time ordered form. The next stage in the production chain combines the ordered slow control with the event information in the DSTs to produce the μDSTs which are used for general analysis.

3.6.3 Event Reconstruction

The HERMES reconstruction algorithm (HRC) [47] finds tracks in the front and back regions of the spectrometer, matches the partial tracks to make full tracks and finally determines the track momentum. HRC is fast as it combines fast pattern recognition and momentum look-up algorithms, so minimising the computing requirements needed to reconstruct the data.

The Fast Pattern Recognition Algorithm

To reconstruct the partial tracks in the front and back of the spectrometer a fast pattern recognition algorithm is used. The whole hit pattern of the detectors is considered, initially at a resolution much less (coarser) than the detector resolution, and possible tracks found. The resolution is then doubled (made more fine) and tracks are sought for all possible configurations allowed by the previous iteration. After about 11 iterations, tracks have been located with resolutions approaching that of the detectors. The algorithm is very fast because only look-up tables of possible track patterns are used.

The Momentum Look-Up Algorithms

HRC also makes use of a very fast method to determine the momentum of the track, from the deflection in the inhomogeneous field of the spectrometer magnet. Instead of tracking the particles through the magnetic field, which is very CPU intensive, a look-up table containing the momentum of a given track as a function of track parameters in front and behind the magnet is used. The relevant track parameters are the position and slope of the track in front of the magnet and the horizontal slope behind the magnet. This is an efficient method which contributes less than Δp/p= 0.5% to the uncertainty in the determination of the track momentum.

Tracking without the Vertex Chambers (VC)

In 1995 the performance of the VC was not deemed sufficient to be included in the tracking. The DVC were installed later and have been available since 1997. For the reconstruction of 1995 and 1996 data an alternative track reconstruction method was developed using only drift chamber data. The front and back partial tracks are generated as usual, except only FC information is used for front track reconstruction. For matching pairs of front-back tracks the match point at the centre of the magnet, defined by the back partial track is used to redefine the front partial track by pivoting it about a conserved space point midway between FC1 and FC2. The front partial track is now forced to agree at the magnetic midpoint with higher quality information from the back partial track. The exclusion of good VC information from the so called *force bridge* method of reconstruction used in 1995 and 1996, causes approximately a factor of two loss of angular resolution.

Chapter 4

Particle Identification (PID)

4.1 Introduction

Particle Identification (PID) is vitally important for distinguishing inclusive positrons from semi-inclusive hadrons. Contamination in the positron or hadron samples can potentially cause significant distortions or dilutions in the measured asymmetries. At HERMES problems of this kind are avoided by ensuring the spectrometer has strong PID capabilities (see section 3.5.2 for a description of the PID detectors). This chapter will describe how information from each of the PID detectors is combined so that the identity of each track can be determined.

After reviewing some principles of probability analysis, the likelihood method used in the HERMES PID scheme will be presented. Input to the PID algorithms called *parent distributions* give the probability a detector response was due to a certain particle type and are vitally important. A Monte Carlo simulation of the PID detector responses was developed so that the parent distributions could be validated by comparison to data and adjustments made (*tuned*) where necessary. The improved parent distributions from this work were implemented into the HERMES Reconstruction Code and have been used to determine particle identity for data taken from 1996 onwards.

4.2 Analysis using a Likelihood Method

When doing a likelihood analysis a probability is defined for each hypothesis under investigation. Once the probabilities have been defined the likelihood is a measure of the relative strength of each hypothesis. In this manner, several hypothesis can be analysed.

For each degree of freedom, n, in a data set, the values have a probability associated with a hypothesis ‘A‘, and another one for hypothesis ‘B‘ and so on for each hypothesis. The total probability that a given set of of values originates from hypothesis A is the product sum of the individual probabilities for each degree of freedom (equation 4.1). In a similar way, the total probability for hypothesis B is defined (equation 4.2).

$$\text{Total probability for } A \quad P_A = \prod_{i=1}^{n} A\mathrm{p}_i, \tag{4.1}$$

$$\text{total probability for } B \quad P_B = \prod_{i=1}^{n} B\mathrm{p}_i. \tag{4.2}$$

For the n degrees of freedom with values y_1, y_2, $y_3 ... y_n$, a histogram for the values y_i is created and the probabilities, p_i are defined as the number of counts in each bin divided by the total number of counts, giving $p_i = \frac{N_{bin}}{N_{total}}$. In order to obtain the individual probabilities, a set of data known to originate from hypothesis A is used. This procedure is repeated for hypothesis B. The PID likelihood parameter is defined as the logarithm of the ratio of the total probabilities (defined in equations 4.1 and 4.2) for each hypothesis

$$PID = log10\left(\frac{P_A}{P_B}\right). \tag{4.3}$$

The log_{10} scale in this definition also allows for easy viewing of the likelihood parameter if the probabilities for A or B tend to extreme values. Also the value of zero in this parameter is the point at which each hypothesis is equally favoured.

4.3 Particle Identification

The majority of particles detected in the spectrometer are actually DIS positrons (electrons in 1998) or pions. In line with the rest of this work, the particle identities will be regarded here as either positrons or hadrons. Unique identification of actual particle type can subsequently be found by further cuts on the data, for example the sign of particle's charge.

At HERMES, the likelihood method discussed in section 4.2 is used to distinguish positrons from hadrons. The response of each detector to positrons and hadrons must be known so that the probability distributions or *parent distributions* can be calculated. Test beam data for the calorimeter and preshower detectors was taken at CERN in 1994 using pions and positrons of various momenta. The response of the Čerenkov is simulated theoretically [49] and the probability distributions of the TRD are taken from a Monte Carlo study [50].

The "PID3" likelihood parameter is calculated for all tracks with hits in the Čerenkov, Preshower and Calorimeter detectors. It is defined as

$$PID3 = log10\left(\frac{P_{e^+}(\text{Čerenkov})P_{e^+}(\text{preshower})P_{e^+}(\text{calorimeter})}{P_h(\text{Čerenkov})P_h(\text{preshower})P_h(\text{calorimeter})}\right), \tag{4.4}$$

where P_{e^+}(detector) is the probability of a positron and P_h(detector) the probability for a hadron in each detector.

The ability of the TRD to separate positrons from hadrons is comparable to the rest of the PID detectors acting in conjunction. Therefore, for the purposes of systematic studies it is useful to define a separate likelihood parameter solely for the TRD,

$$PID5 = log10\left(\frac{P_{e^+}(\text{TRD})}{P_h(\text{TRD})}\right). \tag{4.5}$$

Plotting PID3 against the TRD response to each particle graphically shows how well the data is resolved into positrons or hadrons (figure 4.1a).

The final likelihood, with information from all PID detectors is then

$$PID_{Tot} = PID3 + PID5. \tag{4.6}$$

figure 4.1b shows a histogram of PID_{Tot} for 1995 data. The most obvious cut on the PID_{Tot} likelihood to distinguish the particle types is placed at $PID_{Tot} = 0$. Particles above this cut are most likely to be positrons, below are more likely to be hadrons.

Alternatively particle types may be identified by placing cuts at fixed values of the detector responses. This will be referred to as "*straight*" cuts; a particle

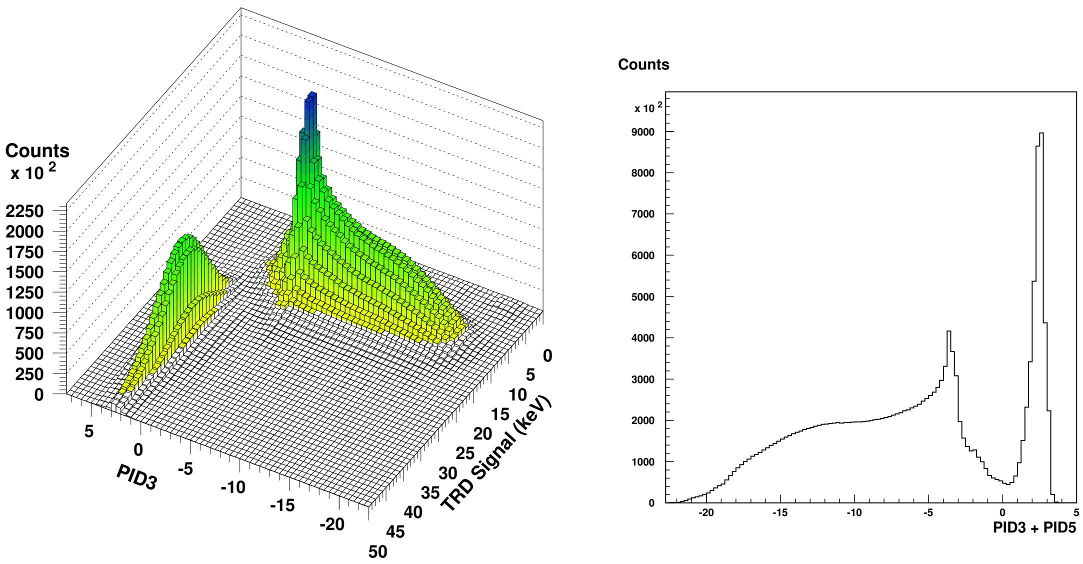

(a) (b)

Figure 4.1: a) Histogram of PID3 likelihood parameter versus TRD response for 1995 data. b) Histogram of PID_{Tot} (=PID3+PID5) likelihood parameter for 1995 data.

passing all straight cuts is accepted into the identified sample. The main benefits of PID with straight cuts are that pure samples of a particular particle type may be identified allowing detector resolution to be studied (see section 6.5.1). The drawback of a straight cut scheme is that ambiguously identified particles which a multidimensional cut could resolve are usually excluded. Consequently, the PID scheme used by HERMES as outlined here identifies 10% more particles than straight cuts alone.

The method of identification outlined is of limited use unless the quality of identified samples is known. Much work is needed to quantify the quality of a likelihood technique. Monte Carlo simulation provides a method for studying the performance of the PID and also allows the validity of the input parent distributions to be checked.

4.4 Modelling the Response of the Spectrometer

The official HERMES Monte Carlo (HMC) uses event generators to simulate the particle interactions at the target. The generated particles are propagated through the simulated model of the HERMES detector, physical components and geometrical acceptance of the detectors are included, with digitisation algorithms to simulate the subsequent detector responses. The full simulation of the HMC is extremely CPU intensive, making it impractical for systematic studies where large samples of events have to be regenerated many times. The simplified Monte Carlo used in this investigation to simulate the response of the PID detectors is the same as that used by HMC if a "fast digitisation" option is specified. The algorithm is referred to as the "toy" Monte Carlo (TMC) and can generate thousands of simulated events per minute. The TMC utilises the same parent distributions as used in the HERMES reconstruction code calculation of the likelihood parameter. This allows the effect of varying the parent distributions to be simulated and by comparing the TMC output with data the validity of the parent distributions can be cross-checked.

4.4.1 The Rejection Method

The rejection method is used to model the response of the PID detectors to positrons and hadrons. Random events are generated with a full range of detector responses and are mapped onto the various probability distributions. Each event is assigned two random coordinates, the first is the parameter being modelled, for example the number of photons seen in the Čerenkov, the second is a random number between zero and the height of the tallest bin of the probability histogram. If an event falls within the distribution it is accepted, if not the event is *rejected*, the 'dice' are rolled again and two new coordinates assigned. The event is again tested and so on until a parameter value is found. Figure 4.2 illustrates this process. If the particle passes it may pass to the next rejection test on the next probability distribution. Once a particle has passed all rejection tests it is added to the data set. Figure 4.3 illustrates the steps taken in the generation of a single event.

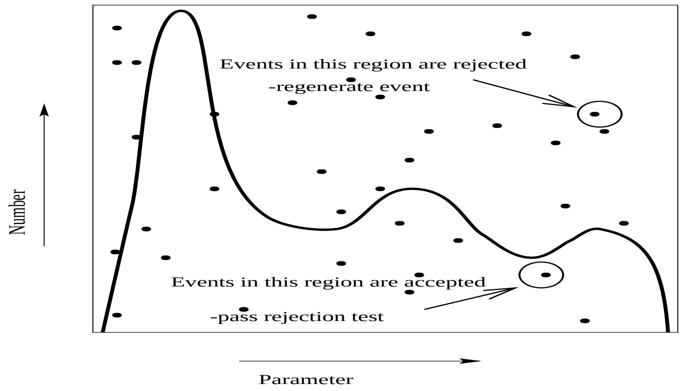

Figure 4.2: Illustration of the rejection method. See text for explanation.

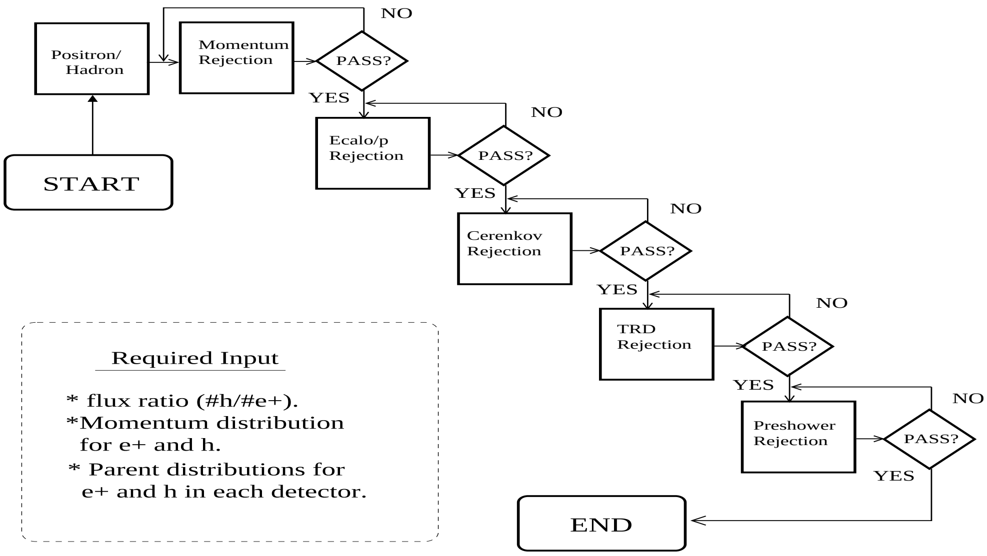

Figure 4.3: Logic Block diagram of the generation of an event in the TMC. The flux ratio is used to set the relative number of positrons and hadrons. A series of rejection tests are then performed. The event generation is concluded once the particle type, momentum and response in each of the PID detectors have been simulated.

4.4.2 Tuning The Monte Carlo

Referring to equations 4.4 and 4.5, the definition of the PID_{Tot} parameter requires knowledge of eight sets of probability distributions, one for each particle type in each detector. These distributions must be correct before a correct simulation of the data can be achieved. The parent distribution for the calorimeter response

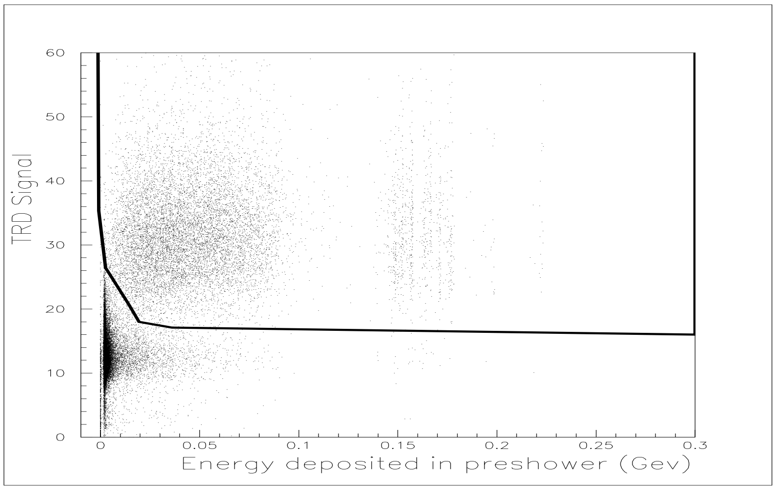

Figure 4.4: TRD signal versus deposited preshower energy, with the graphical cut used to identify positrons.

due to hadrons was known to be incorrect. At the time the test beam data was taken, the calorimeter had no triggering threshold. The triggering threshold in 1995 was 3.5 Gev and in 1996 was lowered several times, eventually to 1.4 Gev. The TMC, using parameterisations of the test beam, produces below threshold events that are not seen in the calorimeter. Detailed study showed that the parameterisations forming the other seven probability distributions also failed in some regions to resemble the response of the detectors. To address these problems the parameterisations were adjusted so that the TMC output was in agreement with the data, a process referred to here as *tuning*.

To model the trigger behaviour of the calorimeter, samples of positrons and hadrons were created using the TRD and preshower, the two detectors which best separate positrons from hadrons. It was assumed that correlations between signals in the TRD and preshower with the calorimeter were negligible [51]. The graphical cut placed on the TRD-preshower plane is shown in figure 4.4, contour mapping this plot assisted the eye in placing the cut at the "valley" point.

The momentum distribution of positrons and hadrons identified by the TRD-preshower cut was then divided into 30 equal bins, from 0 to 30 GeV, and stored. For each particle type histograms of calorimeter energy divided by momentum, E/p, in each of the momentum bins were also stored.

The momentum of each particle generated in the TMC was then found by rejecting from the stored momentum distribution. A value for E/p for the generated particle was then found by a further rejection test using the stored E/p histogram relevant to the particles momentum. Finally, the calorimeter energy is found by multiplying the accepted value of E/p by the particle's momenta. In this way a natural suppression of events below the calorimeter threshold was achieved.

The number of particles found in each bin of the preshower distribution varies by several orders of magnitude, so achieving an accurate parameterisation is not trivial. Consequently, some deviations of the original parameterisation from the test beam data existed and were addressed. The agreement of the preshower hadrons parent distribution with data was improved by adding an overlying Gaussian distribution to the original parameterisation. The effect of this was to increase the value of the parameterisation in a region where previously the agreement of the TMC output to data was poor. The tail of the generated preshower distribution was found to contain an excess of events. By examination of the data, using the same TRD-preshower cut, it was found that 8.7% of the positrons and 0.4% of the hadrons were located in the preshower overflow bins. This effect was modelled by ensuring that the correct fraction of events, taken randomly, were placed in an overflow channel.

For comparisons to be made between the TMC and data, the flux ratio of positrons to hadrons is vitally important. Once the TMC modelled the shapes of the distributions correctly, the integrated flux over all momenta (the ratio of hadrons to positrons) used to generate the events was altered until the peaks of the TRD distribution (being the detector which gives clearest definition of particle type) agreed with the data. This gave a final ratio of 3.0 hadrons to one positron. After tuning the the TMC output agreed well with the data, figure 4.5 show comparisons between the TMC output and 1995 data.

4.5 Definition of Contamination and Efficiency

The Monte Carlo simulation of the detector responses confirms the validity of individual probability distributions and allows the quality of cuts on the PID likelihood to be calculated. The ability of a cut to resolve positrons can be

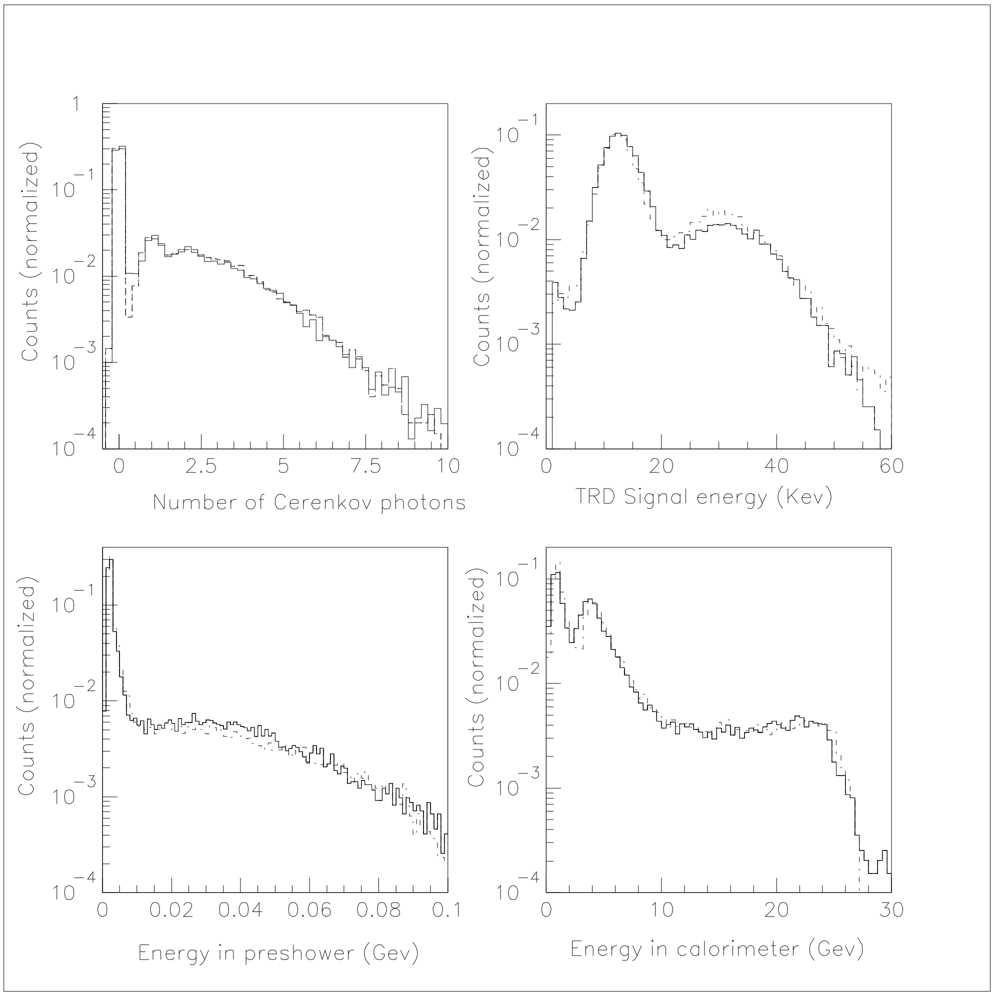

Figure 4.5: Comparison of 1995 PID detector responses to the output of the TMC after the improvements discussed in the text were applied. The TMC is shown with the dark line, the data is shown with a dashed line. All distributions are normalised to one.

described in term of the cut efficiency and the contamination in the resulting samples. The efficiency of a cut on positrons for a given distribution is defined as

$$Eff_{e^+} = \frac{N_{e^+} > cut}{TotalN_{e^+}}. \tag{4.7}$$

Where $N_{e^+} > cut$ is the number of positrons that have a likelihood value greater than the cut and $TotalN_{e^+}$ being the total number of positrons in the data set. The contamination in the positron sample due to hadrons for this cut is defined

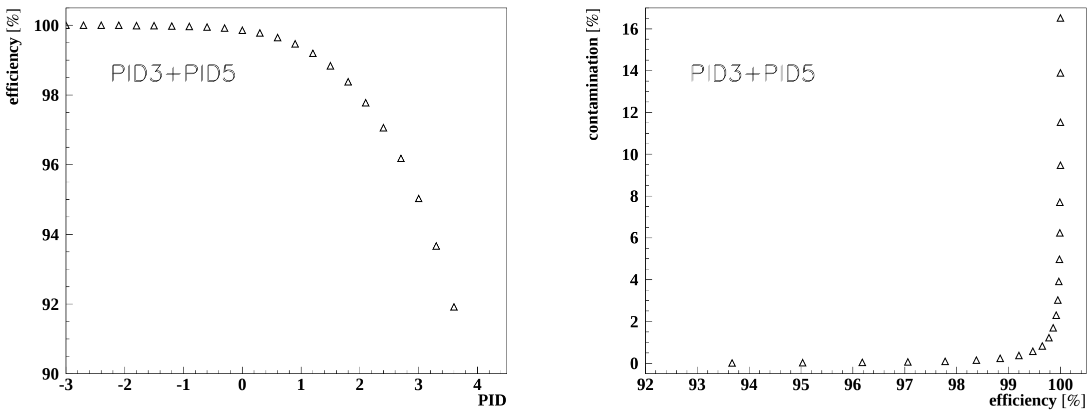

(a) (b)

Figure 4.6: The efficiency of cuts on the PID_{Tot} (=PID3+PID5) likelihood parameter to identify positrons is shown in (a). The dependence of the (hadron) contamination on the positron efficiency for cuts on PID_{Tot} likelihood parameter is shown in (b).

as

$$Cont_h = \frac{N_h > cut}{N_{Total} > cut}. \tag{4.8}$$

$N_h > cut$ is the number of hadrons greater than the cut and

$$N_{Total} > cut = N_{e^+} > cut + N_h > cut. \tag{4.9}$$

The efficiency and contamination for the cut with regard to hadrons, or any other particle that is included in the likelihood, can be found in the same way. With these definitions and the TMC, the ability of cuts on the PID likelihood parameter to resolve positrons and hadrons is determined in a quantitative way.

The TMC was also used in the work of [51], where all the parent distributions were obtained from the data. The efficiency of successive cuts on PID_{Tot} to identify positrons from this method is shown in figure 4.6(a). Figure 4.6(b) shows the efficiency-contamination plane for these cuts. In both studies it found that, for the analysis described in chapter 5, the contamination of identified particles was sufficiently low (less that 0.5%) for the effect on the measured asymmetries to be neglected [52].

Chapter 5

Extraction of the Asymmetries

5.1 Introduction

In this chapter the process of DIS event selection and, as semi-inclusive processes are to be studied, coincident track selection is discussed. An event is defined here as a family of tracks observed in the detector at the time the DIS trigger was tripped. Through the application of this process the final particle count-rates and normalisation factors that allow the various spin asymmetries to be calculated are determined.

There are three sequential stages of data selection. The first determines when the experimental apparatus was under "normal" operation. Once a data set of good quality has been extracted the second level of data selection determines which events have DIS candidates suitable for analysis. For tracks in each analysed DIS event, further requirements locate any semi-inclusive hadrons. The final stage of data selection places certain requirements on the statistical behaviour of the data in each run. The complete HERMES polarised data sets for ^{3}He, and hydrogen were analysed. The analysed deuterium data set was collected from 1998 up until Easter 1999.

5.2 Data Quality

When calculating spin asymmetries, the track detection efficiency for each spin state is assumed to be equal and so cancel when the asymmetry is calculated. It is therefore imperative that data are only analysed if all detector, target and polarimeter subsystems are operational at times when the beam quality is deemed good.

An interval of approximately 10 minutes is used to divide up the raw data into runs at the time of recording. The runs are subdivided into time periods of about 10 seconds (called a burst). Various quantities reporting the status of the apparatus at the end of the burst are then used to determine whether the burst is analysable. Ideally the length of the bursts would be as short as possible to reduce the possible systematic error from changes in the apparatus over time. However, due to the statistical nature of many of the calibrating measurements, a compromise is required.

The main burst quality criteria are given in table 5.1. In the following subsections some aspects of the burst level quality are discussed in more detail.

Burst Quality Criterion			
Criterion	95	96/97	98
Beam current (mA)	$8 < I_e < 32$	$8 < I_e < 50$	$8 < I_e < 50$
Beam polarisation	$0.4 < P_b < 0.7$	$0.3 < P_b < 0.7$	$0.4 < P_b < 0.7$
Target Polarisation	$0.3 < P_t < 0.6$	$0.6 < P_t < 1.05$	$0.6 < P_t < 1.05$
Target Density $\frac{Nucl}{cm^2}$	$.85E15 < n < 1.4E15$	-	-
Plane Eff. FC	$.8 < \varepsilon_{FC} < 1$	-	-
Plane Eff. BC	$.94 < \varepsilon_{FC} < 1$	-	-
Lumi Rate (Bq)	$40 < R_{Lumi} < 210$	$5 < R^{fit}_{Lumi} < 60$	$5 < R_{Lumi} < 60$
Trigger Live-time	$\varepsilon_{DAQ} > 0.5$	$\varepsilon_{DAQ} > 0.8$	$\varepsilon_{DAQ} > 0.8$
Burst Length (s)	$9 < T_{burst} < 11$	$0 < T_{burst} < 11$	$0 < T_{burst} < 11$
Proton Veto rate (Hz)	Pveto < 1500	-	-
Reconstruction Method	NOVC	NOVC(96)/VC(97)	NOVC

Table 5.1: List of Burst Quality Criterion. See text for explanation.

5.2.1 Beam Quality

The weight of each event to the final asymmetry is directly proportional to the beam polarisation. By placing a lower cut on the beam polarisation, data with low weights may be excluded from the analysis. In the 1995 data taking period a lower beam polarisation cut is made at 40%, in the 1996 and 1997 data taking periods the value of this cut is 30%.

A minimum beam current is needed as the beam polarimeters are required to have a reasonable statistical accuracy before reliable quality checks can be made.

5.2.2 Target Quality

Much of the target data quality is performed off-line by experts who supply target quality parameters for inclusion in the μDSTs. These parameters ensure that the target was operating normally for polarised measurements. A lower cut was placed on the target polarisation to exclude data with low weights (see table 5.1).

5.2.3 Tracking Quality

It is vital that the acceptance of the spectrometer does not change significantly over time. The most common cause for such a change in the spectrometers acceptance is that a part of the tracking system is not fully operational. To exclude data taken at these times the high voltage supply to the tracking chambers is monitored. If the high voltage drops, for example because of high background conditions, a plane will show fewer hits than its neighbours. In this case the bursts preceding and following the trip, as well as the burst containing the trip, are not analysed.

Long term changes in the tracking efficiency are assumed to cancel in the measurement of the asymmetry as these are on a time scale which is much longer than that of the target spin flipping.

5.2.4 PID Quality

The PID algorithms used to calculate the likelihood parameters are only meaningful if the parent distributions accurately reflect the responses of each PID detector to electrons (positrons) and hadrons. It is therefore essential that the calibration of the PID detectors is included in the likelihood calculation and that the PID detectors are operating normally.

The normal operation of the PID detectors is determined off-line by experts who supply PID quality parameters for inclusion in the μDSTs.

The analysed 1998 deuterium data is from an HRC "a" production, where default calibrations are used for a first look at the data. Consequently, the PID algorithms are not reliable. Instead, straight cuts on the individual PID detector responses were used. The value of the cuts used are the same as described in section 6.5.1.

5.2.5 Other Quality Criteria

Data contained in the first three or last bursts of a run are excluded from the analysis because the DAQ system is inititiating, which has effects on the tracking efficiency and time synchronisation [77].

5.3 Event Selection

Events containing potential DIS candidates are required to pass the DIS trigger requirements (see section 3.6.1). Further track requirements are then placed on the DIS candidates in each event before the event is deemed worth analysing, i.e. does it contain a good DIS particle, in the semi-inclusive track selection phase.

DIS candidates are required to pass the DIS kinematic cuts and the geometrical cuts listed in table 5.2. Only identified electron/positron tracks (see table 5.3 for PID cuts) are considered to be DIS candidates.

Geometric Track Cuts		
Quantity	Range	Unit
$\lvert\theta_y\rvert$	40,140	mrad
Horizontal Position at Calorimeter	-175,175	cm
Vertical Position at Calorimeter	30,100	cm
Longitudinal Vertex Position	-18,+18	cm
Lateral Vertex Position	0,0.75	cm
Momentum	≥ 0.5	GeV/c
DIS Kinematic Cuts		
Q^2	≥ 1	$(\mathrm{GeV/c})^2$
W^2	≥ 10	GeV^2
y	$0, 0.85$	
E Calorimeter	≥ 3.5	GeV
Hadron Kinematic Cuts		
z	0.2,1	
x_F (π only)	0.1,1	

Table 5.2: List of geometric and kinematic track cuts.

Particle Identities				
	PID		Momentum	
Identity	1995	1996(97)	1995	1996(97)
Lepton	> 2	> 0	-	-
Hadron	< -1	< -2	-	-
$\pi^{\pm}$	< -1	< -2	6-21 GeV/c	4-13.3 Gev/c

Table 5.3: Particle identities. Note that straight cuts were used to define the particle identities in 1998 (see section 6.5.1 for the cuts applied).

5.4 Track selection

In the track selection phase semi-inclusive hadron tracks to accompany the DIS candidate are sought. The kinematic and geometric cuts listed in table 5.2 are applied to tracks determined to be hadrons. The particle identities are determined with the PID parameter as summarised in table 5.3.

5.5 Off-line Quality Criteria

Finally requirements are made on the overall quality of the analysed runs and fills.

- For a run to be included quality, at least 40% of bursts had to be good.
- For a fill to be of included, at least 100 good bursts are required.

After a preliminary analysis of the data it is possible to search for periods in the data that exhibit nonstatistical behaviour.

The positive (negative) charged multiplicity was defined as the total number of positive (negative) charged tracks in coincidence with a DIS event. The positive (negative) charge multiplicities for each target-beam spin configuration were averaged over each run. Charge multiplicities for each run were then compared to an average taken over the year so that runs with nonstatistical values ($> 3\sigma$ from the mean) could be removed from the analysis. In 1995, 45 out of 1412 runs were removed by this criteria. In the subsequent years of data taking it was found that this requirement was no longer required as the expected number of runs with multiplicities greater than 3σ were found. Further systematic studies of the data are described in chapter 6.

5.6 Calculation of the Asymmetries

This section describes the calculation of the inclusive and semi-inclusive asymmetries required for the flavour decomposition of the nucleon spin.

The differential cross-section of a particular process for each target-beam spin state $\sigma^{+(-)}$ is related to the number of detected particles in that spin-state $N^{+(-)}$ as follows:

$$\sigma^{+} = \frac{N^{+}}{\varepsilon \int_{+} L^{+}(t) D^{+} P_B^{+}(t) P_T^{+}(t) dt} \tag{5.1}$$

$$\sigma^{-} = \frac{N^{-}}{\varepsilon \int_{-} L^{-}(t) D^{-} P_B^{-}(t) P_T^{-}(t) dt} \tag{5.2}$$

where ε is the detector efficiency and acceptance (assumed to be spin-independent), $L^{+(-)}(t)$ is the time dependent luminosity, $P_B^{+(-)}(t)$ and $P_T^{+(-)}(t)$ are the polarisations of the beam and target and $D^{+(-)}$ gives the event-by-event photon depolarisation factor averaged over all events in each spin state.

The spin asymmetry of differential cross sections as defined in equation 2.25 can now be rewritten in terms of the measured variables as described below.

If in burst i the total count rate of particle h for each spin state is $N^h_{i\pm}$, the total integrated luminosity is $L_{i\pm}$, the DAQ live time is T_{DAQi} and the product of the beam and target polarisation (assumed constant over the whole burst) is $(P_B{\cdot}P_T)_{i\pm}$, then the general formula for the measured asymmetries can be written as

$$A^h(x) = \frac{N^h_-(x)L_+ - N^h_+(x)L_-}{N^h_-(x)D^h_+(x,Q^2)L_+P_+ + N^h_+(x)D^h_-(x,Q^2)L_-P_-} \tag{5.3}$$

where

x is Bjorken-x,

$N^h_\pm = \sum_{all\ bursts} N^h_{i\pm}$,

$L_\pm = \sum_{all\ bursts} L_{i\pm} * T_{DAQi}$,

$P_\pm = \sum_{all\ bursts} L_{i\pm}{\cdot}(P_B{\cdot}P_T)_{i\pm}$,

and $D^h_\pm(x,Q^2)$ is the photon depolarisation factor.

5.7 Corrections

Distortions to the true photon absorption asymmetry may arise due to non DIS physics processes or detector effects. In this section, the three largest sources of expected distortion are considered. As mentioned previously, effects due to changes in the apparatus over a period of time much larger than the spin-flipping interval, such as the detector acceptance and reconstruction efficiency, are assumed to cancel.

5.7.1 Background

Non Charge Symmetric:

The identified DIS positrons(electrons) will have a degree of contamination from misidentified $h^+(h^-)$ and vice-versa. However the effect on the asymmetries is negligible as the contamination has been shown to be insignificant and the semi-inclusive asymmetries do not differ greatly from the inclusive ones anyway.

Pions originating from ρ_0 production are a source of background which may dilute the observed hadron asymmetry. The number of such pions can be extracted from the number of reconstructed rhos in the data, given that the reconstruction efficiency is known. Less than 0.4% of pions were found to originate from ρ_0 decays where both a π^+ and π^- were reconstructed. While there may be additional ρ_0 events with only a single pion in the acceptance, this number is expected to be correspondingly small.

Photoproduction:

Hadrons and photons (which may pair produce e^+e^-) that are not related to the DIS process under study arise through the process of photoproduction. In such photoproduction events the DIS positron (electron) tends to scatter with an angle that is sufficiently low to escape detection e.g. it passes down the beam pipe. Two sources of background may now arise. Firstly the e^+ or e^- from subsequent pair production may be misidentified as the DIS particle, in which case the event kinematics are incorrectly defined. Secondly the hadrons associated with photoproduction have a higher mean energy (around 7 GeV) than those from the DIS process (around 4 GeV) and so are more likely to be misidentified as DIS positrons(electrons).

So far, possible backgrounds to the inclusive DIS sample have been discussed. Using the same arguments it can be seen that a background also exists for the semi-inclusive hadron samples. As both the photoproduction and pairproduction backgrounds are charge symmetric, i.e. there are as many e^+ as e^- or h^+ as h^- produced from these processes, it is possible to make a correction for these backgrounds in the following manner:

- **Pairproduction**
  If an electron passes all the cuts for a DIS positron then subtract one DIS positron event with identical kinematics to the electron. Assuming equal probabilities for identifying the positrons and electrons from pair production, this will effectively remove the background from pair production from the inclusive DIS sample.

- **Misidentified hadrons**
  Assuming that the probability of misidentifying a hadron as an electron (or positron) is independent of charge, then for every electron with a hadron in coincidence subtract one hadron event of the opposite charge from the sample of hadrons found in coincidence with the DIS positrons. For example if the π^- from a pair produced $\pi^+\pi^-$ were misidentified as the DIS electron then an e^+ and π^- would be subtracted.

Typically about 1% of all DIS events in this analysis originate from charge symmetric backgrounds. It is worth noting here that although the purity method described later can potentially account for these backgrounds (as the photoproduction processes are simulated), the models for photoproduction at medium energies are not optimised to describe the HERMES data. Therefore, the background corrections are made to both data and Monte Carlo.

5.7.2 Kinematic Smearing

Due to the finite momentum and angular resolution of the HERMES spectrometer a correction must be applied to the data to account for the difference between measured and true kinematic quantities. Another major source of kinematic smearing occurs due to interactions of the scattered particles with internal components of the spectrometer.

Correction factors may be calculated by comparing the true kinematic quantities from Hermes Monte Carlo (HMC) with those from the fully GEANT (see section 7.2) reconstructed HMC. In practice correction factors for each asymmetry type are calculated on an appropriate (x, Q^2)-binned kinematic plane (see figure 5.1). Although most of the smearing effects cancel in the asymmetry, there is often such a strong x-dependence in the asymmetry that the migration of only

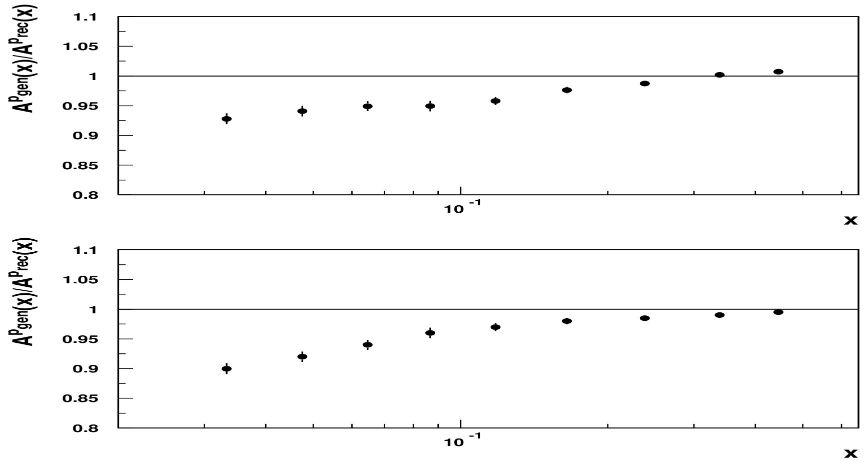

Figure 5.1: Corrections for the Kinematic Smearing (top) and Radiative Corrections (bottom) for the inclusive proton asymmetry A_p^1.

a few percent of events can give rise to large changes in the value of the measured asymmetry. The ^{3}He asymmetries show a much smaller x-dependence, so no smearing correction need be applied. At present no smearing corrections are available for the deuteron asymmetries, so an additional systematic uncertainty is assigned.

5.7.3 Radiative Corrections

The measured deep inelastic cross-section in ep scattering contains all higher order electro-weak contributions as summarised in figure 5.2. The extraction of structure functions requires correction procedures which reduce the measured cross-section to the Born term. However at HERMES energies the electro-weak correction caused by the γ/Z_0 term may be neglected as $Q^2 << M_{Z_0}$. Although the corrections to the unpolarised cross-section measurements may be large, most of the contributions are spin-independent and therefore corrections to the measured asymmetries are comparatively small ($< 5\%$). The cut of $y < 0.85$ on DIS events ensures that data in the region where unpolarised radiative corrections are large are removed from the analysis.

In practice correction factors are calculated in a similar way as for the kinematic smearing; with correction factors for each asymmetry type calculated on an appropriately (x, Q^2)-binned kinematic plane (see figure 5.1). As the corrections are small, instead of correcting the asymmetry they have been absorbed into the systematic uncertainty.

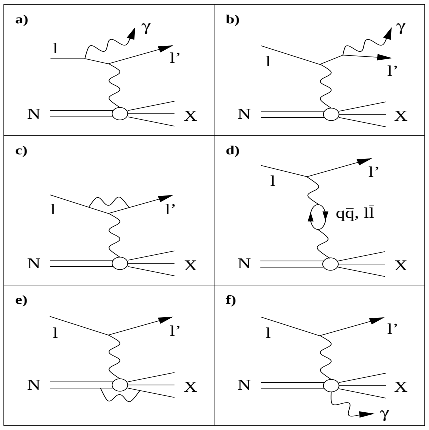

Figure 5.2: The most important radiative corrections at HERMES energies are: a) Bremsstrahlung in the initial state, b) Bremsstrahlung in the final state, c) vertex correction, d) vacuum polarisation, e) hadron vertex correction, f) hadronic Bremsstrahlung.

5.7.4 Correction for A_2

In this work A_2 is not assumed to be zero (see figure 2.3). Consequently, to determine $\frac{g_1}{F_2}$ from $A_{||}$ the value of A_2 must be known (see equation 2.25). Parameterisations of data [10] were used to calculate the value of A_2 for each x bin. Figure 5.3 shows the fit for A_2^p. The scale of A_2^h, relative to to the inclusive case, was assumed to be the same as for $A_{||}$. The factor $(\gamma - \eta)A_2$ for hydrogen and ^3He is typically less that 1%. A_2 for deuterium was assumed to be zero.

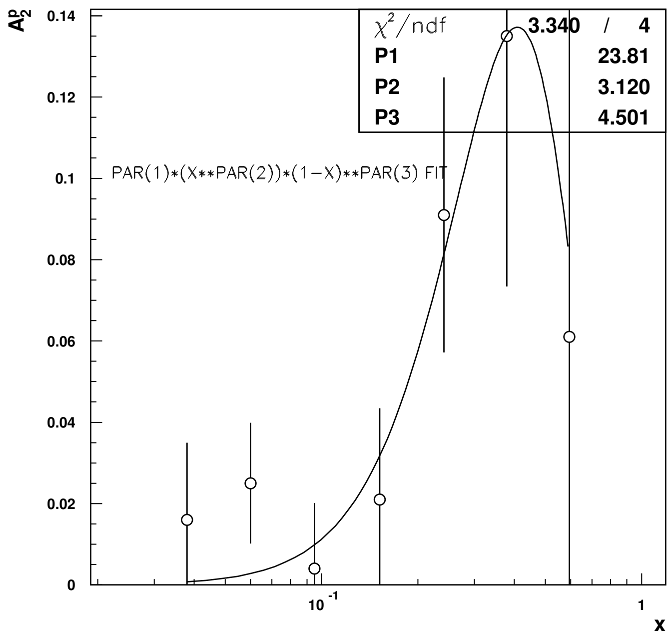

Figure 5.3: Three parameter polynomial fit to data on A_2^p from [10]. A similar fit was performed for A_2^n, enabling both A_1^p and $A_1^{^3He}$ to be determined.

5.8 The Measured Asymmetries

The extracted "raw" asymmetries, $\frac{A_\parallel}{D}$, are now presented for each year of HERMES data taking. The smearing and A_2 corrections are not applied until the quark polarisations are extracted as described in chapter 7.

5.8.1 1995 data (^{3}He target)

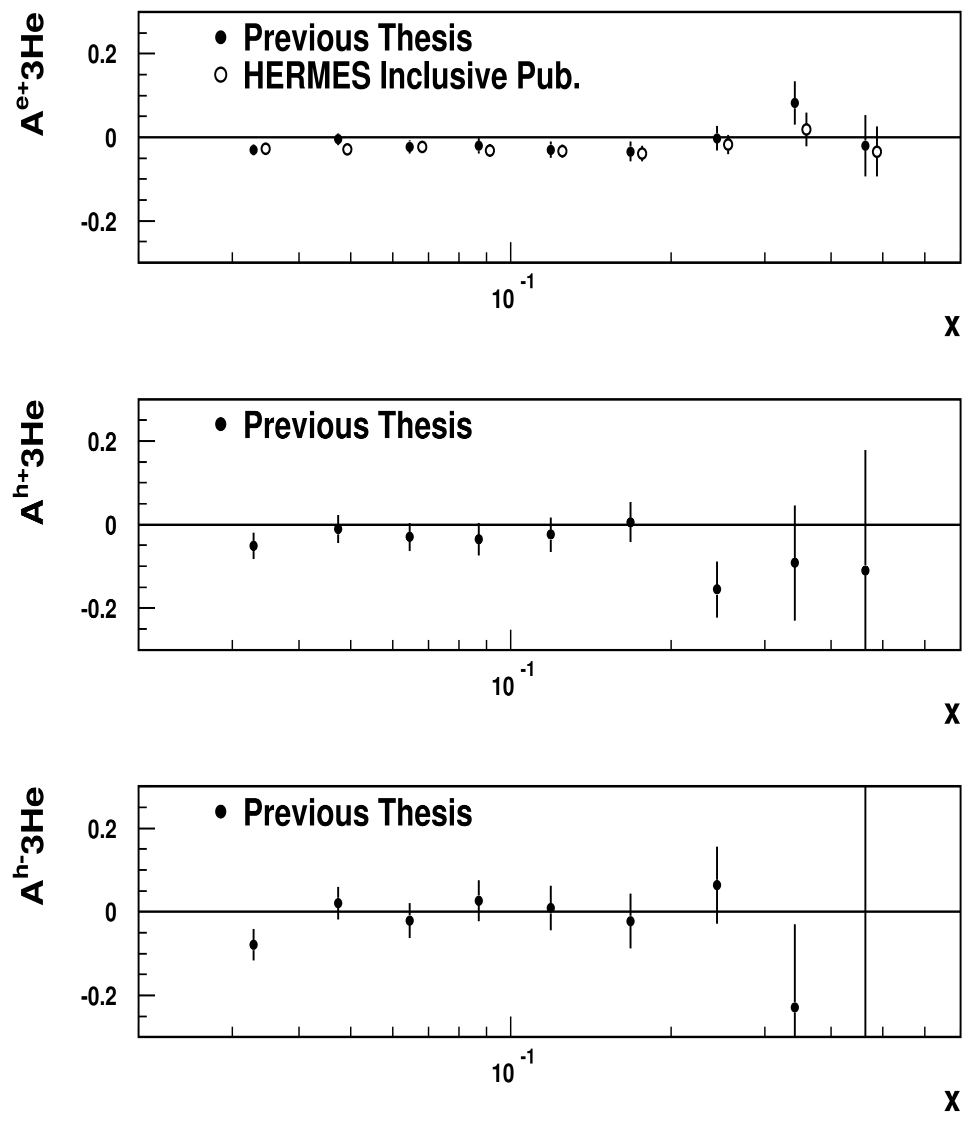

Figure 5.4: For the analysis presented in this thesis, the values of the ^{3}He asymmetries are taken from a previous HERMES thesis [32] (closed circles). The inclusive asymmetry from reference [32] (top figure) is compared to the result obtained for a slightly different analysis of inclusive data only [53]. The middle and bottom figures show the positive and negative hadron asymmetries respectively. Only statistical errors are shown.

5.8.2 1996 data (H target)

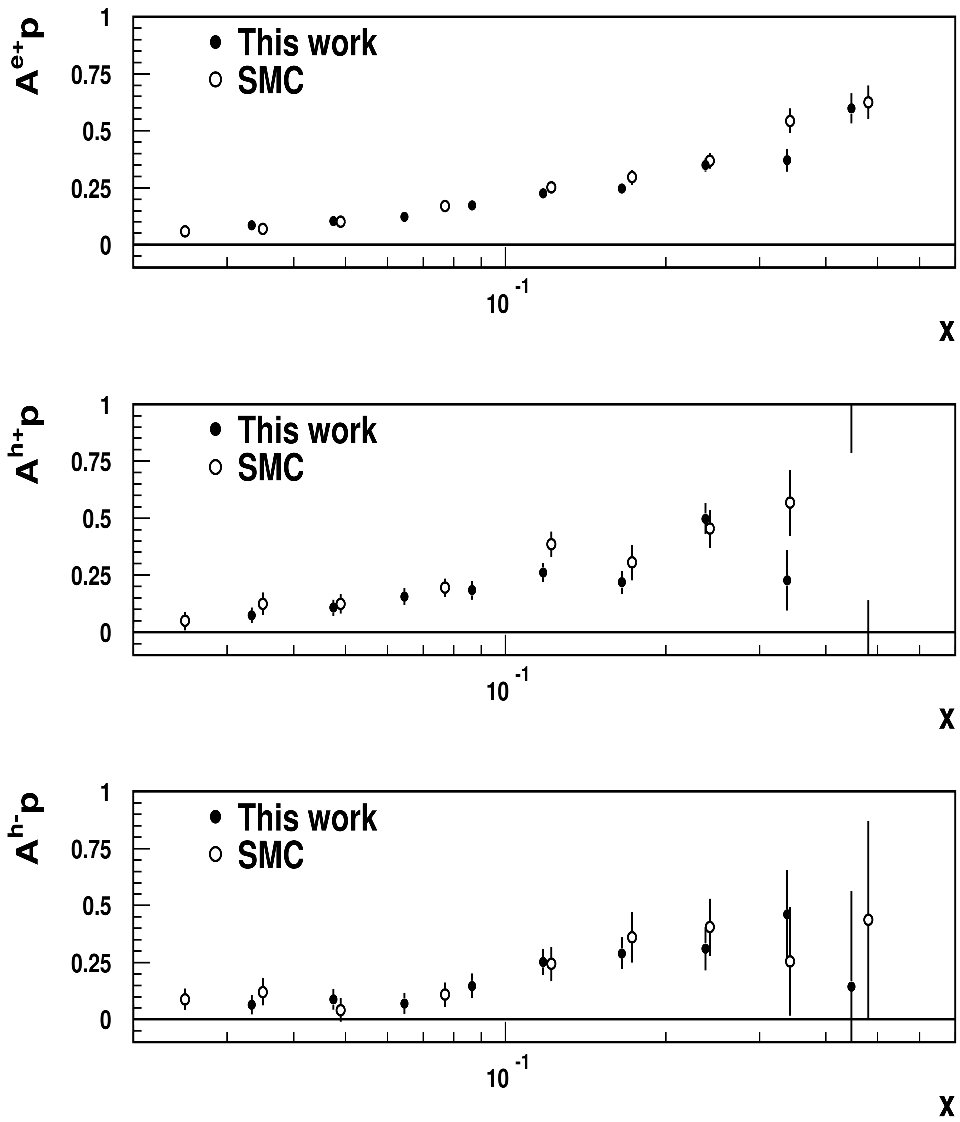

Figure 5.5: The inclusive (top), positive hadron (middle), and negative hadron (bottom) asymmetries results for 1996 hydrogen data (closed circles), compared to the results of SMC [63, 72]. Only statistical errors are shown.

5.8.3 1997 data (H target)

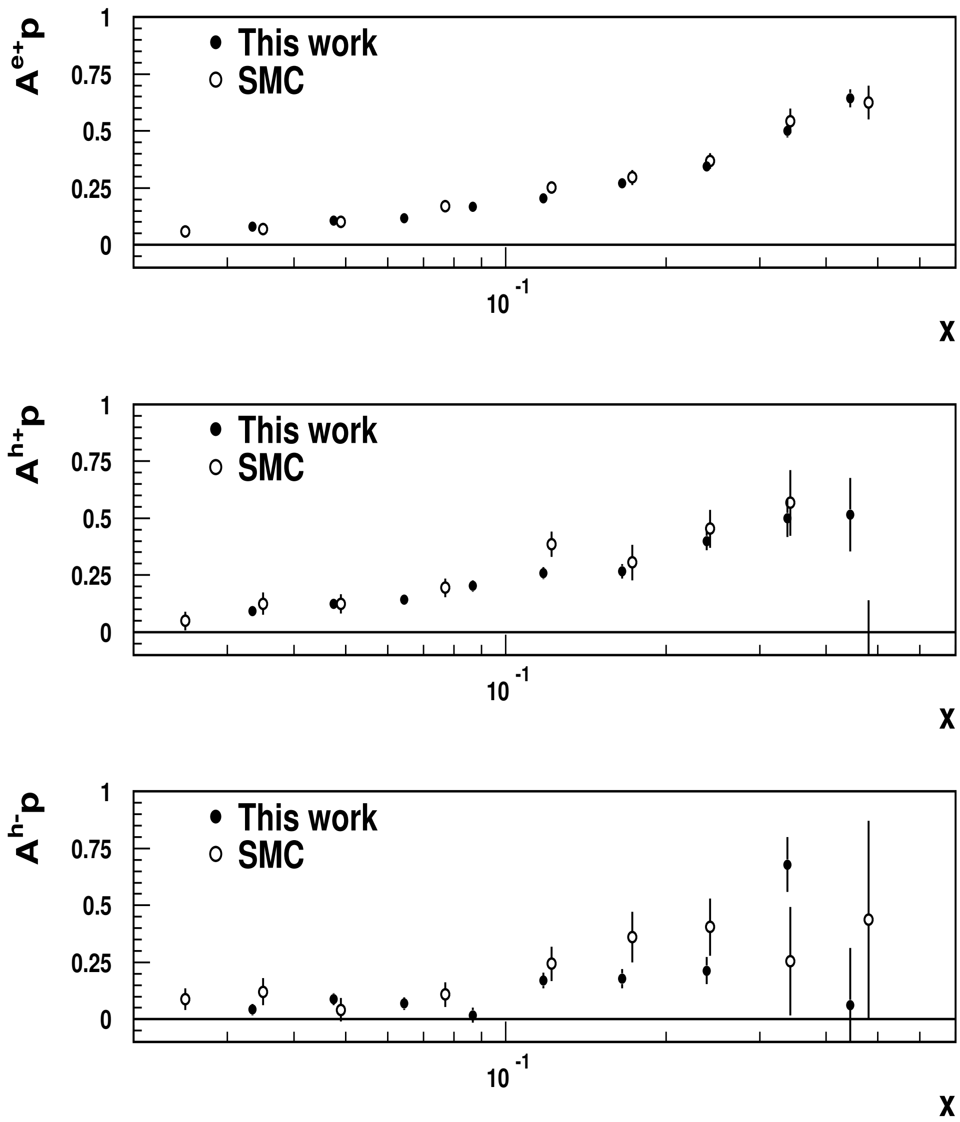

Figure 5.6: The inclusive (top), positive hadron (middle), and negative hadron (bottom) asymmetries results for 1997 hydrogen data (closed circles), compared to the results of SMC [63, 72]. Only statistical errors are shown.

5.8.4 1998 data (D target)

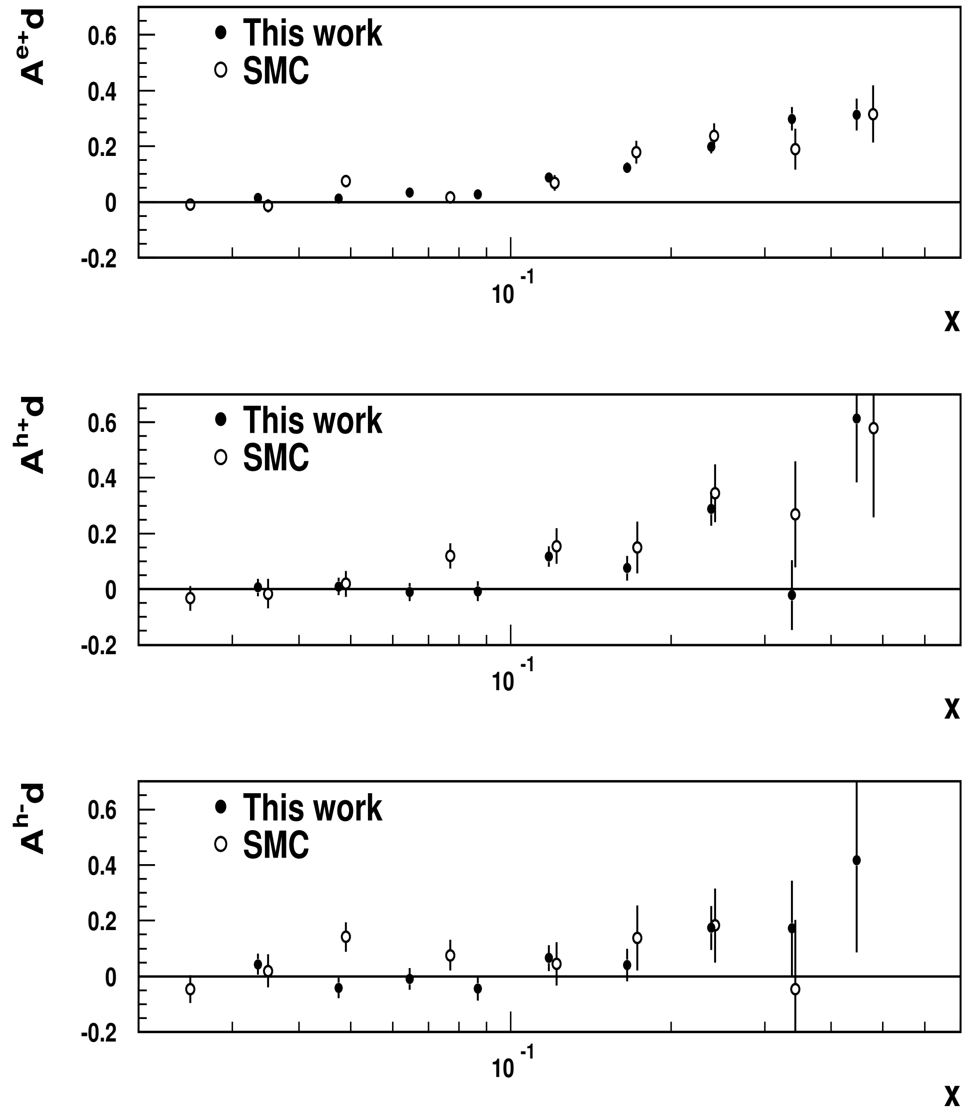

Figure 5.7: The inclusive (top), positive hadron (middle), and negative hadron (bottom) asymmetries results for 1998 deuterium data (closed circles), compared to the results of SMC [63, 72]. Only statistical errors are shown.

Chapter 6

Systematic Studies on the Hydrogen Asymmetries

6.1 Introduction

Measurements of cross section asymmetries are potentially susceptible to many sources of systematic error, which ideally must be minimised or removed altogether. This chapter summarises the extensive systematic studies performed on the measured hydrogen asymmetries. To facilitate these studies the data are split into various time intervals. The largest time interval considered will be the data set of one year's running i.e 1996 or 1997. As figure 6.1 shows, the data of 1997 are further divided into three *periods*. The boundaries of each beam *fill* provide a smaller time interval for study, while smaller yet is a ten minute *run*. The smallest interval considered will be a *burst*, which is typically 10 seconds long and contains about 15 DIS events.

6.2 Normalised Yields

The quality of the selected "good" data was investigated by calculating the normalised yield of inclusive positrons per run, defined as

$$Y_i = \sum_{\text{bursts}} \frac{N_{e^+}}{lumi \, * \, \varepsilon_{\text{DAQ}}} \tag{6.1}$$

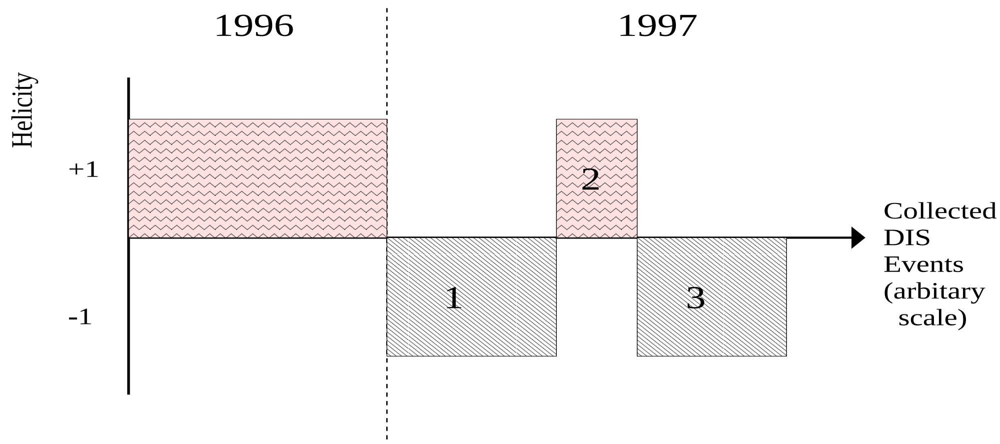

Figure 6.1: Graphical representation of the three periods used for systematic studies of the 1997 data. Also shown is the beam helicity state used to collect data in 1996 and 1997. The periods in 1997 were defined to coincide with times when different beam helicities were used.

where the sum is over all bursts in each fill, N_{e^+} is the number of DIS events in a burst, *lumi* is the value from the luminosity monitor for each burst and $\varepsilon_{\mathrm{DAQ}} = \frac{burstlength}{deadtime}$, is the efficiency of the data acquisition system. If all detector components are on and functioning normally, the normalised yield should show no systematic time dependence within each year.

The error weighted difference from the mean χ_i was calculated, where $\chi_i = \frac{Y_i - \overline{Y}}{\sigma_i}$, with Y_i the normalised yield for fill i, σ_i the statistical error and $\overline{Y}$ the mean taken over data of the appropriate year. Here the statistical error was assumed to behave as $\sqrt{N}$ which is an approximation as sometimes N is small (< 10) [54]. However, this approximation allows the overall stability of the data to be compared for each year. The results for 1996 fills are plotted in figure 6.2a. No systematic time dependence is observed and the overall $\chi^2 = \sum_i (\chi_i)^2/(N-1)$ is low, $\chi^2 = 0.66$. The results for 1997 fills are plotted in figure 6.2b. A significant variation in the normalised yield for 1997 running is seen, as $\chi^2 = 1.58$. Many factors can potentially alter the normalised yield. However, no conclusive explanation for the yield variation in 1997 has been found. The fluctuations in the yield were not found to be correlated with the size of the asymmetries.

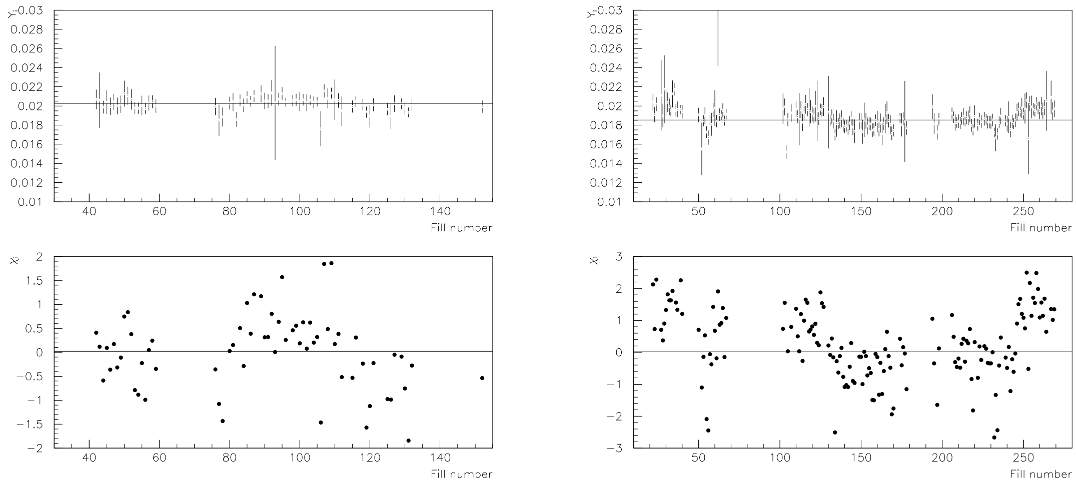

(a) (b)

Figure 6.2: Top: The normalised yield for fills in (a) 1996 and (b) 1997. The error weighted mean for the year is shown. Bottom: The error weighted difference from the mean χ_i, for each fill in (a) 1996 and (b) 1997, with respect to the mean for the year. A significant time dependence is seen in 1997.

6.3 Multiplicity Study

The stability of the spectrometer over time, for detection of semi-inclusive processes, was investigated by examining multiplicities[1]. The average multiplicity per fill, for all charged tracks before track cuts, is shown in figure 6.3.

Separate multiplicities were defined for positive and negative hadrons which pass the usual track cuts described in chapter 5. Average values for these multiplicities were found for 1996 and the three periods in 1997 (shown in figure 6.1). The division of 1997 data into these periods is useful for systematic studies as each period has a similar statistical significance. The definition of the periods was chosen to coincide with times when different beam helicities were used, allowing possible correlations to be investigated. The second period was taken with the same beam helicity as used in the 1996 run. Data of the first and third periods were taken with the opposite beam helicity.

[1]Here multiplicity refers to the mean number of a given particle per DIS event

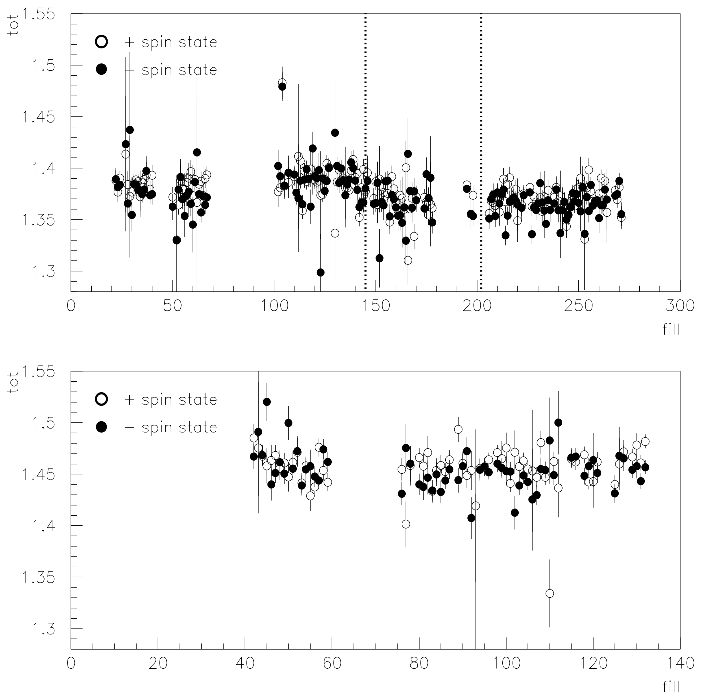

Figure 6.3: Top: The multiplicity for all charged tracks, before cuts, for fills in 1997. The dashed vertical lines divides the 1997 data into three periods. A decrease occurs around the start of the second period. Bottom: The total charged multiplicity for fills in 1996. The multiplicity is constant throughout the year, to within the statistical error.

The results of the multiplicity study are shown in table 6.1 and interpreted below.

Interval	$n_{h^+}^{\uparrow\downarrow}$	$n_{h^+}^{\uparrow\uparrow}$	$n_{h^-}^{\uparrow\downarrow}$	$n_{h^-}^{\uparrow\uparrow}$
96	0.1309±0.0007	0.1280±0.0007	0.0702±0.0005	0.0685±0.0005
97 Period 1	0.1303±0.0007	0.1276±0.0007	0.0676±0.0005	0.0694±0.0006
97 Period 2	0.1265±0.0012	0.1209±0.0012	0.0659±0.0009	0.0652±0.0010
97 Period 3	0.1244±0.0008	0.1203±0.0008	0.0652±0.0006	0.0673±0.0006

Table 6.1: Semi-inclusive hadron multiplicities after track cuts, averaged over various time intervals, were determined for the aligned (↑↑) and anti-aligned (↑↓) target-beam spin states. Periods two and three have significantly lower multiplicities compared to the 1996 and period one values. From examination of the table, it is seen that the relative size of the multiplicity for each spin orientation is reversed for negative hadrons in period one and three.

When calculating a multiplicity, n_h, a count rate is normalised to the number of inclusive DIS positrons ($n_h = N_h/N_{e^+}$), which have their own asymmetry. The difference in multiplicity between each spin state is, therefore, related to the size of that particle's asymmetry relative to the inclusive asymmetry. In 1996 both positive and negative semi-inclusive asymmetries are larger than the inclusive asymmetry in many x bins. The results in table 6.1 imply that the negative hadron asymmetry extracted from periods one and three will be smaller than the inclusive asymmetry. This is seen to be the case when the extracted asymmetries are integrated over x as the multiplicities have been. The significance of this will be discussed in section 6.5.6.

6.4 False Asymmetry Study

A study has been made to identify non-statistical yield fluctuations in the data by randomising the target spin bits assigned in the data. A random spin bit was applied to each burst in the data and then a normal asymmetry analysis was performed, with the measured asymmetry averaged over all x bins. This procedure was repeated 3000 times, each time with a different set of random spin bits. For each particle type, the resulting 3000 asymmetries were plotted as a histogram. Provided the spin bits are truly random, the resulting distribution should be a Gaussian centred at zero. In addition, the width of the distribution should be the same as the statistical error of the asymmetry.

The results are shown in figures 6.4 and 6.5. In table 6.2, where the results are summarised, the values obtained for a previous study of 1995 are also given. For each particle type, the widths of the Gaussians are slightly larger than the statistical errors on the asymmetries. This indicates yield fluctuations in the data due to unidentified systematic problems with the experiment. The last column of table 6.2 shows the relative size of the yield fluctuations compared to the statistical error. No single component of the detector was found to be the source of the fluctuations. The fluctuations are more likely due to combined instabilities of each of the detector components. These results are not necessarily unexpected. Similar experiments measuring spin asymmetries routinely add an uncertainty due to yield fluctuations [56] caused by changes in spectrometer acceptance. An uncertainty due to the false asymmetry is included in the estimation of the systematic error (see 7.6).

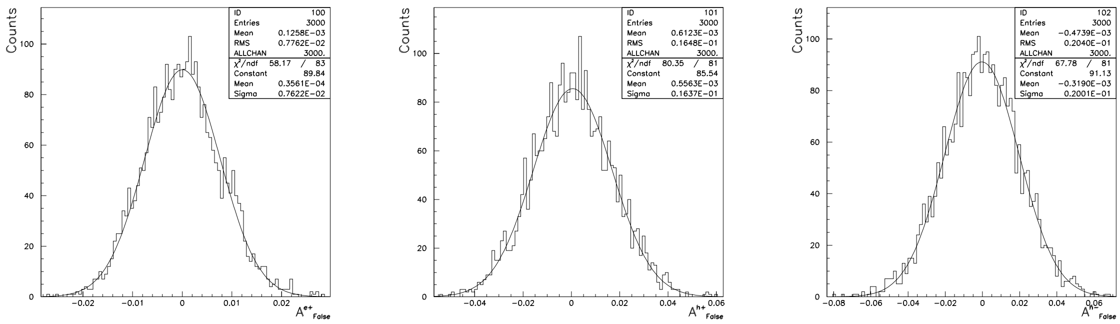

(a) (b) (c)

Figure 6.4: The resulting asymmetries for random target spin bits applied to each burst of the 1996 data 3000 times, for the (a) e^+, (b) h^+ and (c) h^- asymmetries. A Gaussian fit was made to each distribution.

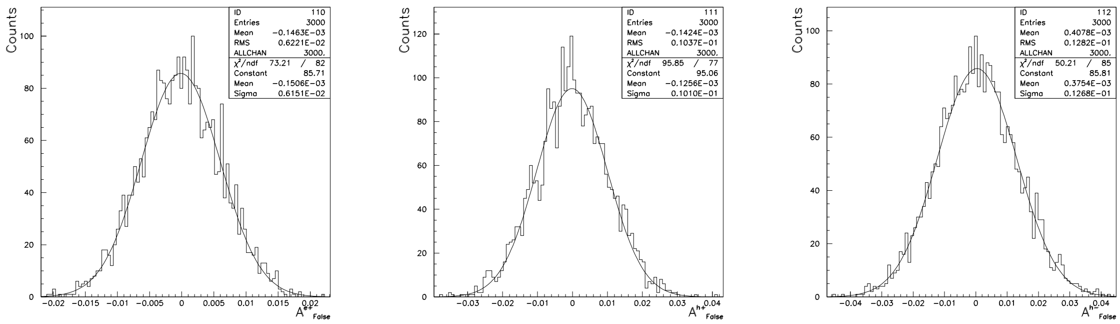

(a) (b) (c)

Figure 6.5: The resulting asymmetries for random target spin bits applied to each burst of the 1997 data 3000 times, for the (a) e^+, (b) h^+ and (c) h^- asymmetries. A Gaussian fit was made to each distribution.

Asymmetry type	True asymmetry value	Width of random distribution	Size of yield fluctuation($\%\sigma_{\mathrm{Stat}}$)
(95) e^+	–	–	46%
(95) h^+	-0.0343 ± 0.0145	0.0156 ± 0.0002	40%
(95) h^-	0.0090 ± 0.0183	0.0191 ± 0.0002	32%
(96) e^+	0.18749 ± 0.0071	0.0076 ± 0.0001	10%
(96) h^+	0.18853 ± 0.0153	0.0164 ± 0.0002	39%
(96) h^-	0.01480 ± 0.0197	0.0200 ± 0.0003	18%
(97) e^+	0.01905 ± 0.0043	0.0062 ± 0.0001	103%
(97) h^+	0.19276 ± 0.0092	0.0101 ± 0.0001	46%
(97) h^-	0.09814 ± 0.0119	0.0127 ± 0.0002	34%

Table 6.2: Summary of the randomised spin bit study for 1996 and 1997 inclusive and demi-inclusive data. The size of the effect relative to the statistical error $((\sigma^2_{False} - \sigma^2_{Stat})^{\frac{1}{2}}/\sigma_{Stat})$, is given in the last column. The results for 1995 (taken from reference [32]) are also given. For each of the false asymmetry distributions, the mean was found to be consistant with zero to within the error on the fit, showing that no false asymmetries exist.

6.5 Dependence of the Asymmetries on Various Variables

6.5.1 PID Study

To check the PID algorithm the asymmetries were extracted from particles identified by placing straight cuts (i.e. at a fixed value) on the PID detectors responses. The DIS positrons were required to have:

- Preshower energy > 7.5 Mev,
- A ratio of calorimeter energy/$p > 0.8$,
- TRD energy > 18 Kev.

Hadrons were identified if the particle track had:

- Preshower energy < 7.5 Mev,
- A ratio of calorimeter energy/$p < 0.8$,

- TRD energy < 15 Kev.

Asymmetries were determined from particles identified with the straight cut method outlined above and also using the usual cuts on the PID likelihood parameter (discussed in section 5.4). In figure 6.6 the asymmetry results obtained for each method are shown.

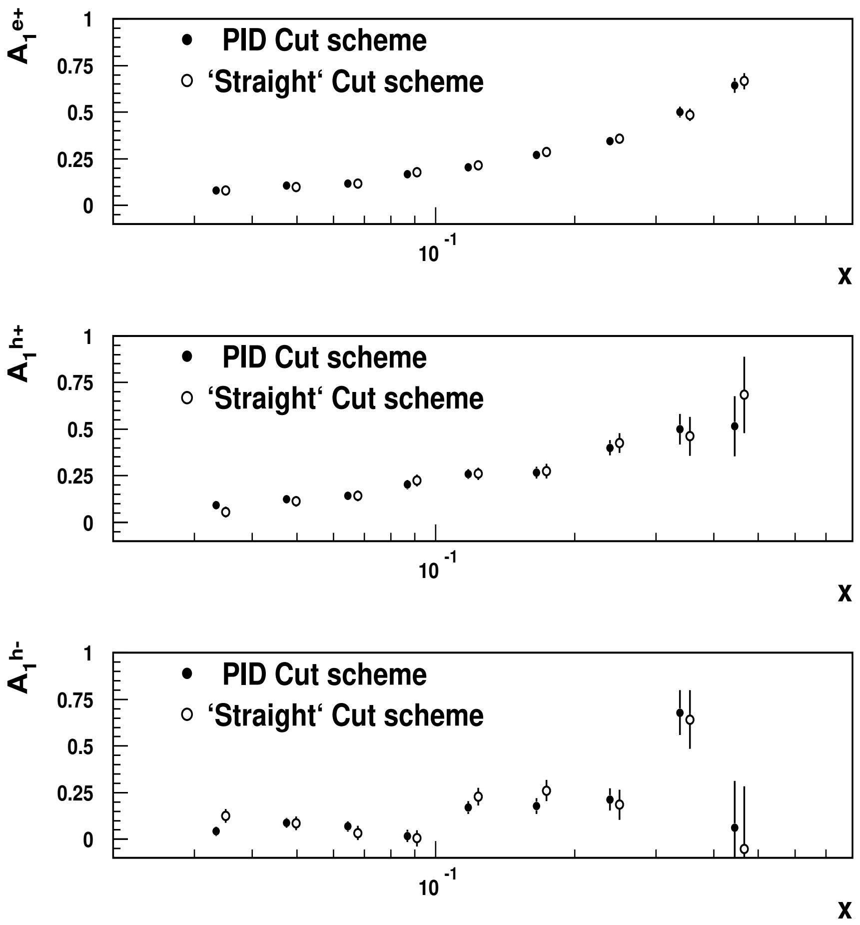

Figure 6.6: Inclusive and semi-inclusive asymmetries extracted from the hydrogen data of the 1997 run using either the usual cuts on the PID likelihood parameter (closed circles) or straight cuts on the PID detectors responses (open circles). See text for definition of the applied straight cuts.

No significant differences are seen between the two sets of asymmetries, showing that the PID likelihood method has a negligible effect on the size of the asymmetries.

6.5.2 Hadron Kinematic Cuts

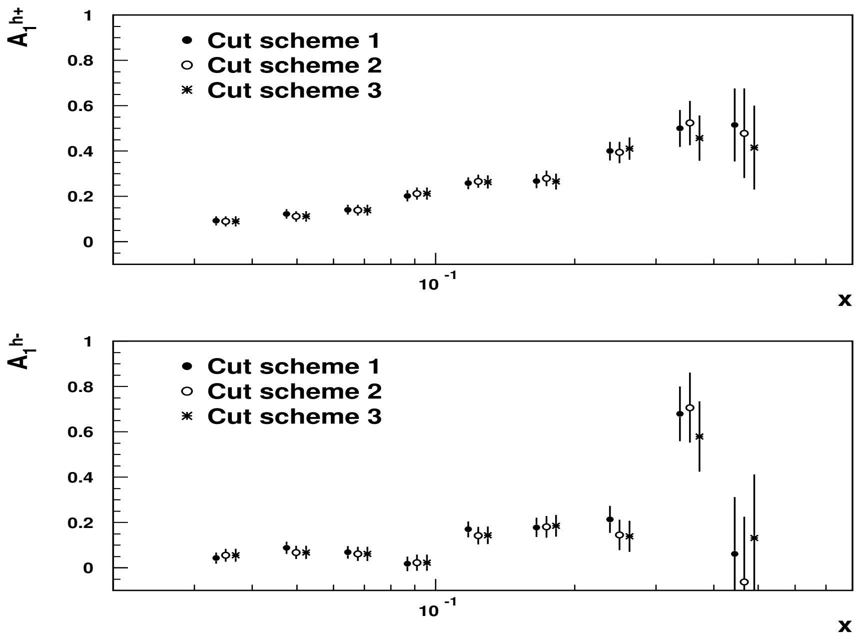

Figure 6.7: Comparison of various kinematic cut schemes used to extract the 1997 positive (top) and negative (bottom) hadron asymmetries. See text for definition of cut schemes. The difference in the resulting asymmetries is small.

The effect of varying the hadron kinematic cuts was investigated by running the analysis with the three different cut schemes listed below.

- Cut scheme 1: $W^2 > 10.0$ GeV^2, $x_F > 0.1$, $z > 0.2$.
- Cut scheme 2: $W^2 > 10.0$ GeV^2, $x_F > 0.1$.
- Cut scheme 3: $x_F > 0.2$, $z > 0.2$.

The difference in the resulting asymmetries (see figure 6.7) is small, showing that the asymmetry results do not depend strongly on the choice of cuts.

6.5.3 Stability Over Time

To check for any time dependency of the asymmetries, the asymmetry per fill, averaged over all x bins, was calculated and its time dependence studied. The error-weighted differences from the mean, χ_i, were calculated, where $\chi_i = \frac{A_i - \bar{A}}{\sigma_i}$, with A_i the asymmetry for fill i, σ_i its statistical error and $\bar{A}$ the average asymmetry for all fills (shown in table 6.2). Figure 6.8 shows the results for the 1997 running period plotted against fill number. Normal χ^2 values were found, 181/168 for the inclusive asymmetry, 166/168 for the positive hadron asymmetry and 160/168 for the negative hadron asymmetry. Reasonable χ^2 values of 84/68, 75/68 and 74/68 were also found for the 1996 inclusive, positive hadron and negative hadrons asymmetries respectively. It can therefore be concluded that no significant time dependency of the asymmetries is observed between fills in each year of running with the hydrogen target.

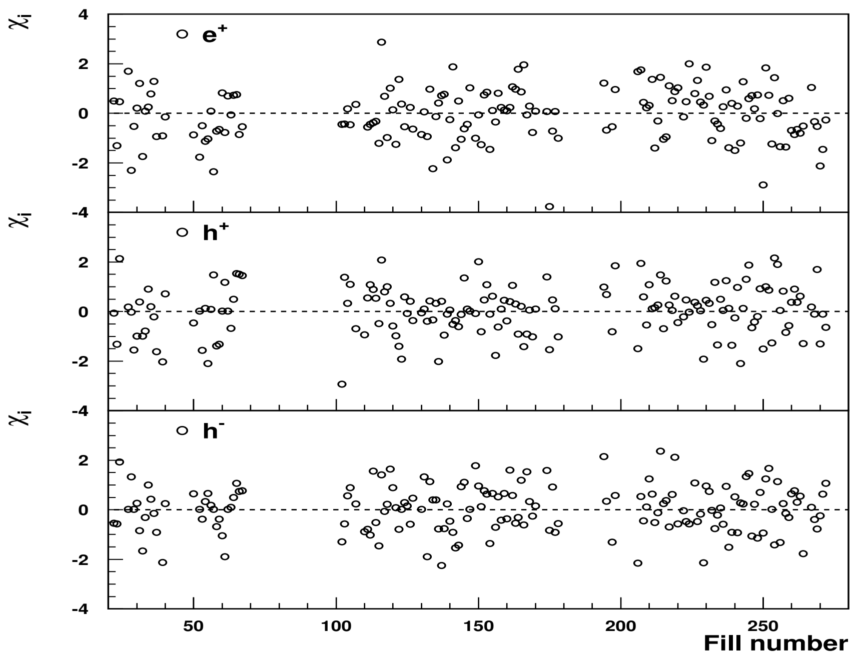

Figure 6.8: The weighted difference from the year's mean of the (top) e^+, (middle) h^+ and (bottom) h^- asymmetries extracted from fills taken in 1997.

6.5.4 The Asymmetry Results for each Reconstruction Method

An additional data production of the 1997 run (97c0) was performed using the "force bridge" method adopted for reconstruction of the 1995 and 1996 data (see section 3.6.3 for details of the reconstruction methods). Although poorer spatial resolution is obtained with the "force bridge" method, this allowed the effect of different reconstruction methods on the asymmetries to studied directly.

The asymmetries extracted from the 97c0 μDSTs, which contain the "force bridge" reconstructed data, are compared to those from the usual 97b2 μDSTs in figure 6.9. No statistically significant differences are seen leading to the conclusion that the choice of reconstruction method has a negligible effect on the size of the asymmetry.

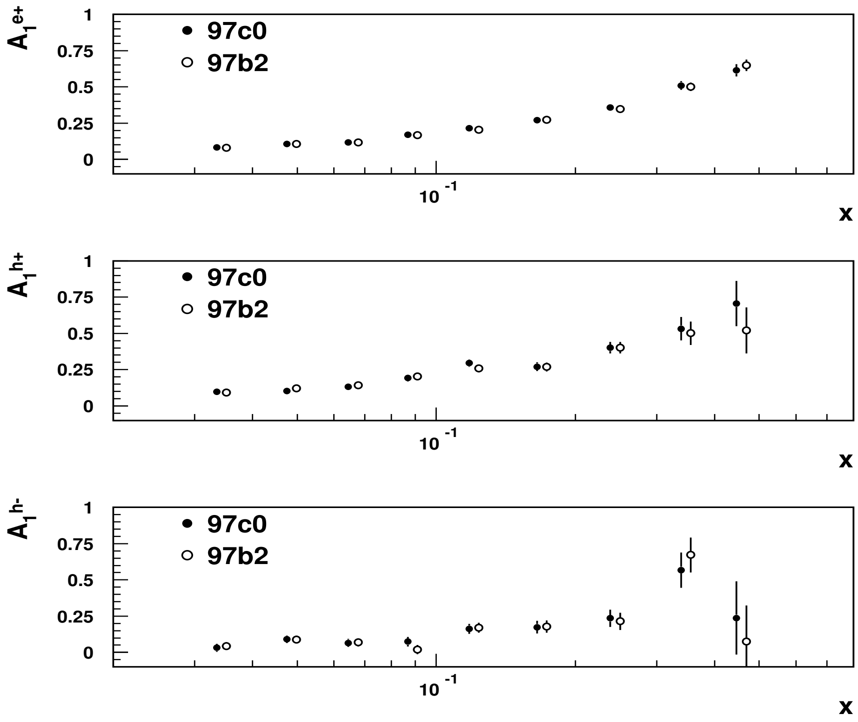

Figure 6.9: Inclusive (top) and semi-inclusive (middle and bottom) asymmetries extracted from the hydrogen data of the 1997 run using either the standard 1997 reconstruction or the "force bridge" method adopted.

6.5.5 The Hydrogen Asymmetry Results for 1996 and 1997

The asymmetry results extracted for each years running with the polarised hydrogen target were compared to check for compatibility. The results for the positive and negative hadrons are compared in figure 6.10.

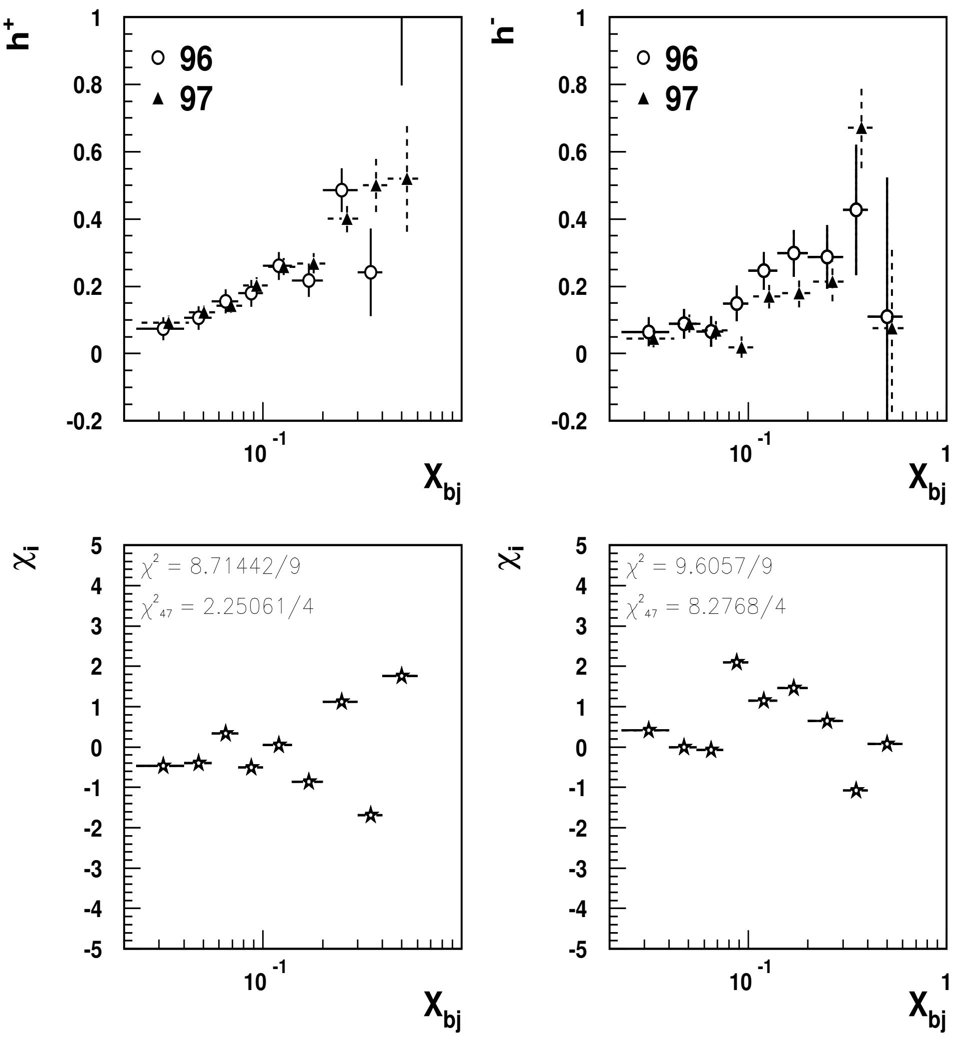

Figure 6.10: The positive (upper left) and negative (upper right) hadron asymmetries extracted from the 1996 run are compared to those of 1997. The lower plots show the error weighted difference χ_i for each bin, the χ^2 values for all bins and for bins four to seven are also shown.

The inclusive asymmetries of the 1996 and 1997 data sets were found to be statistically compatible ($\chi^2 = 8.4/9$) as were the positive hadron asymmetries

(χ^2=8.7/9). The negative hadron asymmetry is systematically high (low) in 1996 (1997) in four consecutive bins, although the χ^2 average over all bins is normal (χ^2=9.5/9). χ^2_{47} is the value of χ^2 for bins four to seventh only. For the negative hadrons the high value of χ^2_{47}=8.3/4 is indication of a statistical anomaly.

In order to quantify the probability for the occurrence of the anomaly observed in the negative hadron asymmetries a simple Monte Carlo simulation was performed. It was assumed that the asymmetries were totally correlated (the worst case) and that no correlations in the size of the error weighted difference χ_i between neighbouring bins existed. The probability for a run of four consecutive bins to lie consistently at least one error bar (1σ) above, or below, the expectation was 0.06. This corresponds to a 1.9σ effect overall, which leads to the conclusion that the asymmetries extracted from the 1996 run may not be statistically compatible with those of 1997.

6.5.6 The Asymmetry Results for each Beam Helicity

Sources of systematic difference between each years asymmetries could be correlated to times when different beam helicities were used for data taking. Theoretically, no dependence of the asymmetries to the beam helicity is expected due to the assumption of factorisation, used in defining the fragmentation functions. However, other changes in beam conditions may occur when the helicity is reversed, such as beam slope and position, and these factors may have an influence on the asymmetry results.

The asymmetries taken in the second period of 1997 with a +1 beam helicity, were found to be compatible with the 1996 results (also +1 helicity). The dependence of the asymmetries on the beam helicity was studied by comparing the asymmetries extracted from data taken with either +1 or −1 beam helicities. The +1 beam helicity data was taken in 1996 and 1997 period two. The −1 beam helicity data was taken in 1997 periods one and three.

The inclusive asymmetries extracted from +1 beam helicity and −1 beam helicity data are found to be compatible. Figure 6.11 shows the results for the positive and negative hadrons. No significant difference is seen between the positive hadron asymmetries. The significance of the disagreement in the negative hadron asymmetries is greater than for the comparison of 1996 and 1997 asym-

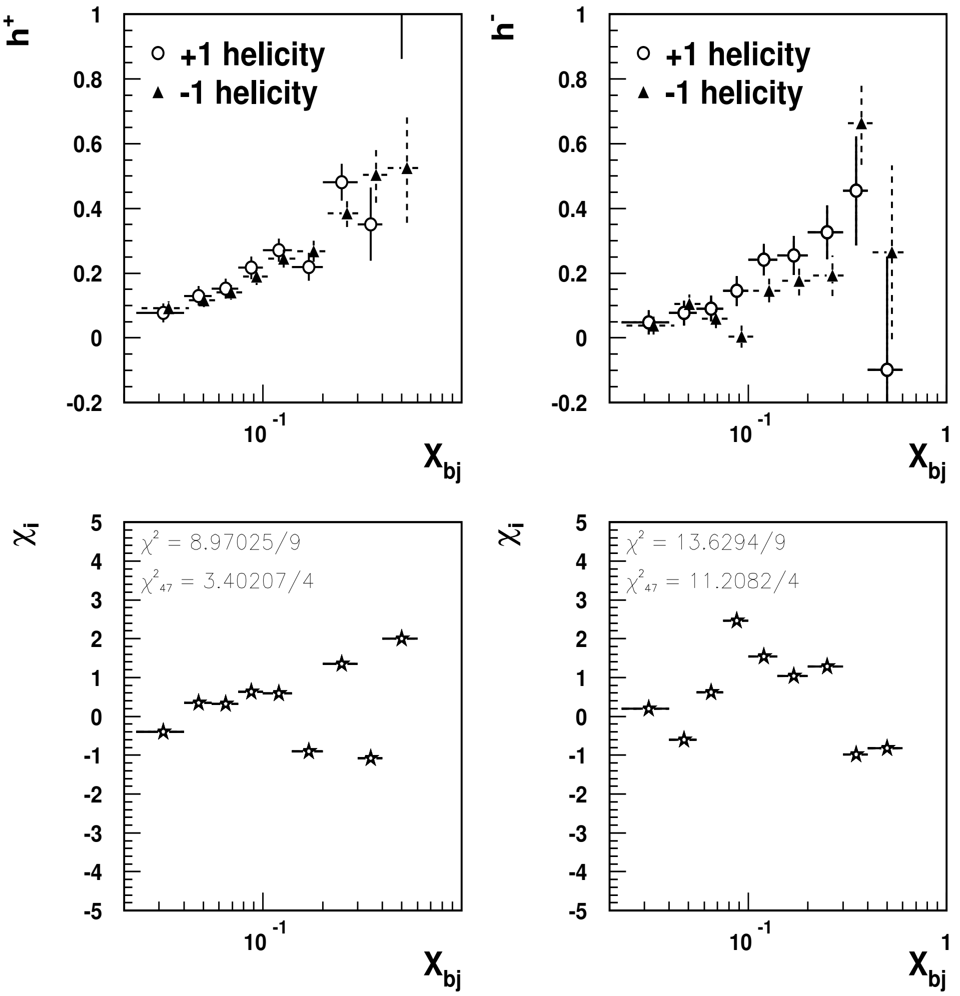

Figure 6.11: The positive (upper left) and negative (upper right) hadron asymmetries extracted from the +1 beam helicity data are compared to those of the −1 beam helicity data. The lower plots show the error weighted difference χ_i for each bin, the χ^2 values for all bins and for bins four to seven are also shown.

metries. Table 6.3 summarises the χ^2 results for the comparison of asymmetries extracted from 1996 and 1997, and for each beam helicity. The associated χ^2 probability is also given.

In conclusion, this study suggests the cause of the discrepancy seen between the 1996 and 1997 negative semi-inclusive hadron asymmetries originates in data

	1996 – 1997		Beam helicity states +1 – -1	
Asymmetry type	χ^2 value	χ^2 probability	χ^2 value	χ^2 probability
e^+	8.4/9	0.49	8.5/9	0.48
h^+	8.7/9	0.47	9.0/9	0.44
h^-	9.5/9	0.39	13.6/9	0.14
h^-_{47}	8.3/4	0.08	11.2/4	0.02

Table 6.3: Summary of χ^2 values. The χ^2 probabilities are the likelihood of getting a larger χ^2 value from two compatible data sets.

taken in periods 1 and 3 of the 1997 data, which coincides with times the beam helicity was reversed relative to 1996.

6.5.7 Miscellaneous Studies

A detailed set of systematic studies were undertaken in order to account for the observed discrepancy in the negative hadrons asymmetries, a full description can be found in a HERMES internal note [55]. The studies presented in this chapter are a summary of the main investigations that were conducted on the hydrogen data. However, many other studies were performed as summarised below:

- Any correlation of the asymmetries with beam parameters such as slope, position, and current was sought. None was found.
- A correlation of the asymmetries with the distance between primary and hadron vertex was sought to check whether the anomaly was due to decaying particles. None was found.
- The asymmetries for each year were extracted as a function of variables other than Bjorken x, such as angle in the horizontal and vertical planes, z, Q^2 and W^2. The anomaly was not found to be correlated to these variables.
- The hadron z and p distributions of 1996 and 1997 were compared to locate any significant differences. The anomaly was not found to be correlated to these variables.

In each case no significant differences, that could account for the negative hadron anomaly, were observed between the data collected in 1996 and 1997.

6.6 Conclusion

The systematic studies discussed in this chapter reveal a significant difference between the negative semi-inclusive hadron asymmetries extracted from data taken with the hydrogen target in 1996 and 1997. An extensive set of systematic studies have been performed and show no abnormal behaviour of the experimental apparatus. A correlation has been observed between the size of the negative hadron asymmetry and the beams' helicity state. A mechanism for producing such an effect has not been established.

In conclusion, the negative hadron anomaly could be due to a statistical fluctuation, an unknown problem with the experimental apparatus, or a dependence of the asymmetry on the beam helicity. None of these possibilities can be ruled out. A correlation with the beam helicity can only be verified by repeating the measurement. Because many aspects of the data set have been considered, it may be that the observation of an unlikely effect has become more probable. For the 1999 data taking the beam helicity is reversed every four weeks. The analysis of this data may verify, or otherwise, a helicity dependent effect.

To proceed with the extraction of the quark polarisations, it will be assumed that the difference is due to a statistical fluctuation. It is worth noting that if the difference were due to a dependence on the beam helicity, then the effect would largely cancel when $+1$ and -1 beam helicity asymmetries are combined in the purity analysis.

Chapter 7

Extraction of the Quark Polarisations

7.1 Introduction

In this chapter the Purity method, discussed in 2.6, for extracting the quark polarisations from measured inclusive and semi-inclusive cross section asymmetries will be applied to the asymmetry data presented in chapter 5. The method presented here is similar to that used to extract the published HERMES results [57] for data collected up until 1997. SMC also utilise a "purity method" for their extraction of the polarised Parton Density Functions (PDFs) [63].

With the measured asymmetries, models of the ^{3}He and deuterium atoms and the purities, the quark polarisations can be determined. The results obtained are presented as a function of x in section 7.5. In section 7.6 the systematic uncertainty on the final results are considered. Finally in section 7.7 the moments of the polarised PDFs are presented.

7.2 Generation of Purities

To determine the purities, as defined in equation 2.51,

$$P_q^h(x,z) = \frac{e_q^2 D_q^h(z) q(x)}{\sum_{q'} e_{q'}^2 D_{q'}^h(z) q'(x)}, \tag{2.51}$$

information about the unpolarised Parton Density Functions (PDFs), $q(x)$, and the fragmentation functions, $D_q^h(z)$, is needed as represented in figure 7.1. The PDFs used in this work are obtained from global fits to world data, which are then evolved to HERMES energy range. The LUND string model, discussed in section 2.5.2, is used in a Monte Carlo simulation of the hadronisation. Fragmentation Functions are then determined from the Monte Carlo output. The acceptance of the spectrometer has a negligible effect on the inclusive asymmetry and consequently can be neglected when calculating the inclusive purities. This is not the case for the semi-inclusive hadrons. Therefore, the hadron purities must be determined for the same acceptance as the asymmetry measurement. The details of how the purities are determined using this method are discussed below.

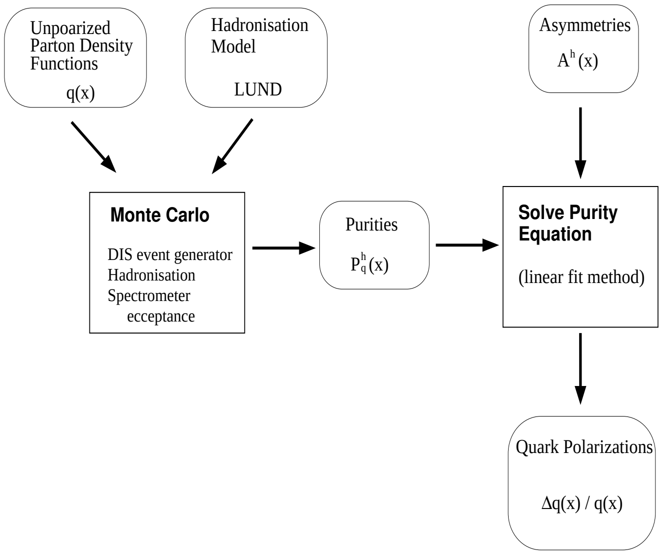

Figure 7.1: The Purity method for extracting the quark polarisations. The parton densities and LUND hadronisation model are used in the Monte Carlo simulation. The purity matrix is then calculated from the Monte Carlo output. The quark polarisations are finally obtained by performing a linear fit to the inverted purity equation 2.55 (see text for details).

In the Monte Carlo program, the initial stage of the DIS interaction is simulated with the LEPTO [59] code. Here the PDFs are used to determine the relative probability that the scattering takes place on a particular quark flavour. The actual flavour of the struck quark is then determined in a probabilistic way. For this analysis the CTEQ low Q^2 parametrisations [60] are used. The event information is then passed to the second stage, implemented with the JETSET code [31], where the LUND model is used to perform the hadronisation.

At this stage all the event information as would be observed by a "perfect" detector has been simulated. All that remains to be done is the simulation of the spectrometer acceptance. An accurate simulation of the HERMES spectrometer can be performed with the GEANT code [61]. However, this process is prohibitively time consuming as it is very CPU intensive. A much faster alternative is provided by placing a "box" acceptance on the generated events. This is implemented by the use of momentum look-up tables, from the HERMES Reconstruction Code (HRC), which give the exact momentum cut-offs of particles observed in the spectrometer. The effect of these momentum cuts is equivalent to the fiducial cuts placed on the data. Studies have shown [58, 54, 64] that the acceptance of the spectrometer has a negligible effect on the inclusive positron asymmetry. Therefore, the purities for the inclusive positrons can be determined directly from the PDFs as described below.

Each entry in the purity matrix gives the probability that a particle type h originated from scattering on a quark of flavour q. For inclusive particles the purity can be determined trivially from

$$P_q^{e^+}(x) = \frac{e_q^2 q(x)}{\sum_{q'} e_{q'}^2 q'(x)}. \tag{7.1}$$

With the inputs discussed above, the semi-inclusive entries to the purity matrix are given by

$$P_q^h(x,z) = \frac{\#h : [l(N,q) \to l'hX](x,z)}{\# : [lN \to l'hX](x,z)} \tag{7.2}$$

where $\#h : [l(N,q) \to l'hX]$ is the number of hadrons of type h in all accepted events where the lepton scattered off a quark of flavour q in the nucleon N and $\# : [lN \to l'hX]$ is the number of hadrons h in all accepted events.

Note: Different sets of PDFs are used for systematic studies. To avoid regenerating Monte Carlo events every time a new set is used, effective fragmentation functions with detector acceptance included are computed such that

$$\tilde{D}_q^h(x,z) = \frac{\#h : [l(N,q) \to l'hX](x,z)}{\# : [l(N,q) \to l'X](x)}, \tag{7.3}$$

where $\# : [l(N,q) \to l'X](x)$ is the number of accepted events where a quark of flavour q was struck. The purities for a given set of PDFs are then be calculated as

$$P_q^h(x,z) = \frac{\tilde{D}_q^h(x,z)e_q^2 q(x)}{\sum_{q'} \tilde{D}_{q'}^h(x,z)e_{q'}^2 q'(x)}, \tag{7.4}$$

which does not require rerunning the Monte Carlo (see [62, 64, 77] for more details). The purity values obtained with a proton target are summarised in figure 7.2.

7.3 Definition of Sea Polarisation

Examination of figure 7.2 reveals that a large fraction of events originate from scattering on u quarks and that the data are comparatively insensitive to other, less dominant, flavours. The statistical accuracy of the data set analysed here does not allow for a full decomposition of the polarisations for each sea quark flavour. The quark polarisation values are obtained with a χ^2 minimisation routine, which has certain minimum statistics requirements. Sufficient statistical accuracy is gained by combining sea flavours with low sensitivity. This requires assumptions about how the polarisations of the sea quarks are related.

7.3.1 $SU(3)$ Flavour-symmetric Sea

An $SU(3)$ flavour-symmetric sea is one where the number density of quarks in each helicity state are equal for each sea quark flavour. Such that:

$$\frac{1}{6}\Delta\overline{q}_{SU(3)} = \Delta u_s = \Delta\overline{u} = \Delta d_s = \Delta\overline{d} = \Delta s = \Delta\overline{s}, \tag{7.5}$$

where $\Delta\overline{q}$ corresponds to the polarised structure function for the total sea. Now the contribution the sea quarks make to measured asymmetries can be expressed as

$$P_{\overline{q}SU(3)}^h \frac{\Delta\overline{q}_{SU(3)}}{\overline{q}} = \frac{\Delta\overline{q}_{SU(3)}}{6}\left(\frac{P_{u_s}^h}{u_s} + \frac{P_{\overline{u}}^h}{\overline{u}} + \frac{P_{d_s}^h}{d_s} + \frac{P_{\overline{d}}^h}{\overline{d}} + \frac{P_s^h}{s} + \frac{P_{\overline{s}}^h}{\overline{s}}\right), \tag{7.6}$$

where the unpolarised sea has been defined as

$$\overline{q} = u_s + \overline{u} + d_s + \overline{d} + s + \overline{s}. \tag{7.7}$$

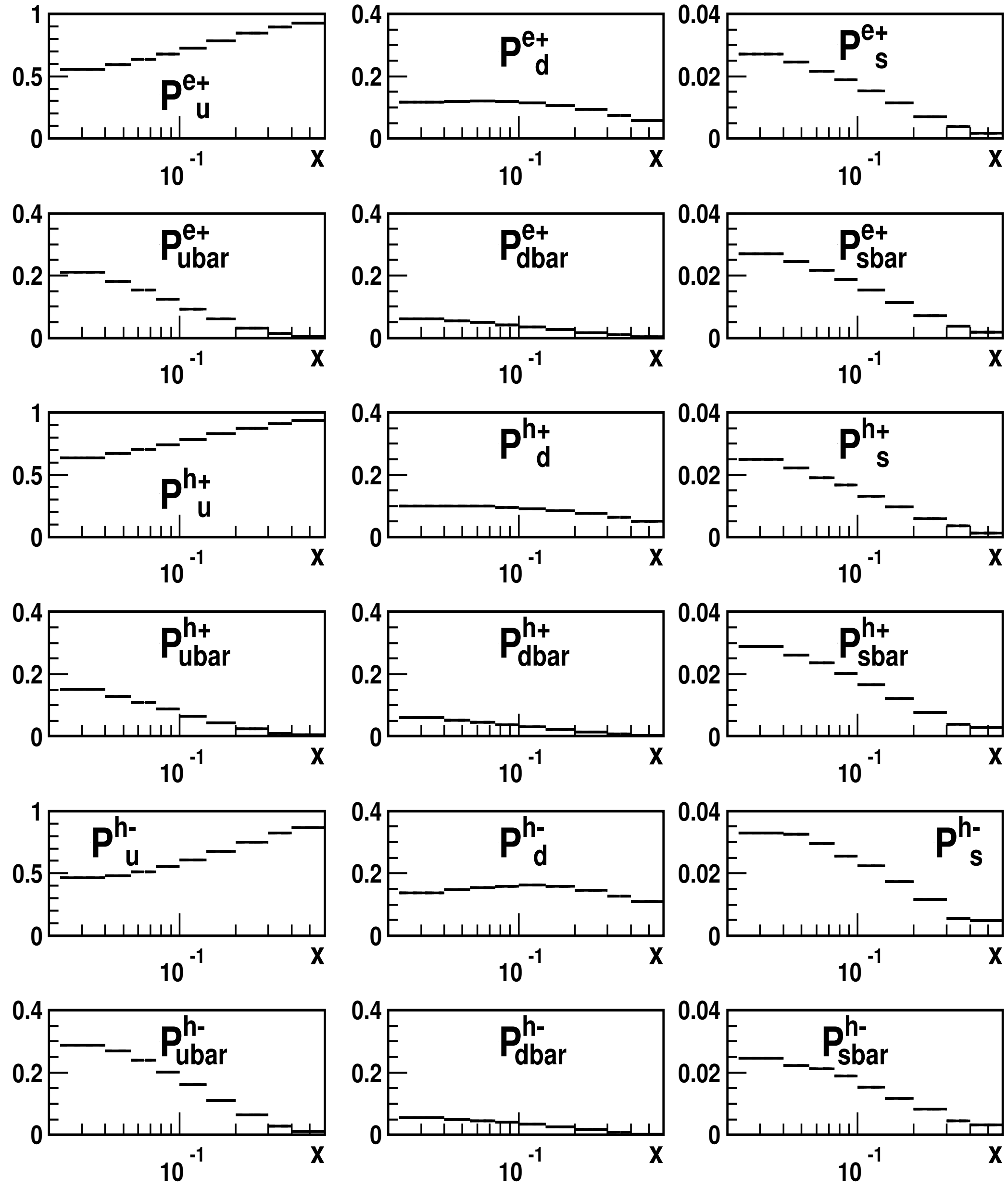

Figure 7.2: Values of the proton target purities for inclusive positrons and semi-inclusive charged hadrons, as determined from the Monte Carlo output. The LUND string fragmentation model and the CTEQ [60] low Q^2 unpolarised PDFs were used in the Monte Carlo simulation.

With this "valence" definition the fitted quark polarisations are $\frac{\Delta u_v}{u_v}$, $\frac{\Delta d_v}{d_v}$ and $\frac{\Delta \overline{q}_{\mathrm{SU(3)}}}{\overline{q}}$, where the contribution of valence and sea quarks are separated, $q_v = q - q_{\mathrm{sea}}$, allowing the polarisation of the valence quarks to be investigated.

Alternatively a "flavour symmetric" fit is possible by defining 7.6 for s and $\overline{s}$ quarks only and absorbing the remaining sea quarks of each flavour into the corresponding valence distribution. The fitted polarisations are then $\frac{\Delta u + \Delta \overline{u}}{u + \overline{u}}$, $\frac{\Delta d + \Delta \overline{d}}{d + \overline{d}}$, and $\frac{\Delta s + \Delta \overline{s}}{s + \overline{s}}$.

7.3.2 Polarisation-symmetric Sea

Alternatively, it can be assumed that the sea quark polarisations are independent of flavour:

$$\left(\frac{\Delta \overline{q}}{\overline{q}}\right)_{\mathrm{Pol}} = \frac{\Delta u_s}{u_s} = \frac{\Delta \overline{u}}{\overline{u}} = \frac{\Delta d_s}{d_s} = \frac{\Delta \overline{d}}{\overline{d}} = \frac{\Delta s}{s} = \frac{\Delta \overline{s}}{\overline{s}}. \tag{7.8}$$

This assumption is motivated by the fact that the unpolarised sea quark densities are known to break $SU(3)$ flavour-symmetry [65]. Therefore, the assumption that the polarised sea is $SU(3)$ flavour-symmetric may not be valid. The purity of the sea in the polarisation-symmetric model is the sum of all sea contributions,

$$P^h_{\overline{q}\mathrm{Pol}} \left(\frac{\Delta \overline{q}}{\overline{q}}\right)_{\mathrm{Pol}} = \left(\frac{\Delta \overline{q}}{\overline{q}}\right)_{\mathrm{Pol}} \left[P^h_{u_s} + P^h_{\overline{u}} + P^h_{d_s} + P^h_{\overline{d}} + P^h_{s} + P^h_{\overline{s}}\right]. \tag{7.9}$$

The fitted polarisations are $\frac{\Delta u_v}{u_v}$, $\frac{\Delta d_v}{d_v}$ and $\left(\frac{\Delta \overline{q}}{\overline{q}}\right)_{\mathrm{Pol}}$.

7.4 Interpretation of the ^{3}He and Deuterium Data

Models for of ^{3}He and deuterium nuclei will now be reviewed. They will allow the measured asymmetries to be unfolded to asymmetries on a "bare" neutron. The neutron asymmetries from the ^{3}He and deuterium data are compared in section 7.4.3. An extension to the purity method will then be presented which incorporates these nuclear models and will allow the measured asymmetries to be related, via purities on the proton and neutron, to the quark polarisations.

7.4.1 ^{3}He

The most probable configuration for the ^{3}He nucleus (S-state) has the proton spins pairing off with zero net spin, in which case the ^{3}He asymmetries are entirely due to the neutron (although diluted due to the effectively unpolarised protons). However, other configurations have significant probabilities which alter the effective polarisation of the nucleons. For a completely polarised ^{3}He nucleus, the effective neutron and proton polarisations are $P_n^{(^3He)} = 0.86 \pm 0.02$ and $P_p^{(^3He)} = -0.028 \pm 0.004$ respectively [66, 67].

The measured asymmetry on ^{3}He is composed of separate contributions from the neutron and protons, such that

$$A_{^3He}^{(^3He)} = A_n^{(^3He)} + A_p^{(^3He)}. \tag{7.10}$$

In this notation, the upper script denotes the target used, and the lower the particle type the asymmetry originates from. So that $A_n^{(^3He)}$ is the asymmetry of a neutron and $A_p^{(^3He)}$ the asymmetry due to both protons bound within ^{3}He. The asymmetry of the bound nucleons may now be described in terms of their unbound asymmetry,

$$A_n^{(^3He)} = A_n^{(n)} f_n P_n^{(^3He)}, \tag{7.11}$$

$$A_p^{(^3He)} = A_p^{(p)} f_p P_p^{(^3He)}. \tag{7.12}$$

Where the "*dilution*" factors $f_{n,p}$ account for the probability of scattering off either the neutron or the protons, thus

$$f_p = 1 - f_n \tag{7.13}$$

by definition. The dilution factors may be found by taking a ratio of the nucleon differential cross sections, relevant to the process in question. This gives,

$$f_n = \frac{\sigma_n}{\sigma_n + 2\sigma_p} \qquad \text{and} \qquad f_p = \frac{2\sigma_p}{\sigma_n + 2\sigma_p}. \tag{7.14}$$

For the inclusive asymmetries, the DIS structure functions are substituted for cross sections and by assuming

$$F_2^n = 2F_2^d - F_2^p, \tag{7.15}$$

where F_2^d refers to the deuteron structure function, values of the dilution factors can be calculated from directly measurable quantities, i.e.

$$f_n = \frac{2F_2^d - F_2^p}{2F_2^d + F_2^p}. \tag{7.16}$$

Substituting this expression for the neutron dilution factor into equations 7.11 and 7.12, and then substituting equations 7.11 and 7.12 back into 7.10, yields an expression for the inclusive DIS neutron asymmetry that contains no unknown quantities.

$$A_n^{1(n)} = \frac{A_{^3He}^{1(^3He)}}{P_n f_n^{DIS}} - \frac{P_p}{P_n} \frac{1 - f_n^{DIS}}{f_n^{DIS}} A_p^{1(p)} \tag{7.17}$$

As the nucleon structure functions pertain to inclusive scattering, more information is necessary to establish the relative probabilities of a semi-inclusive hadron originating from a proton or a neutron. Assuming the differential cross section for a process, h, on ^{3}He may be written as

$$\sigma_{^3He}^h = 2\sigma_p^h + \sigma_n^h. \tag{7.18}$$

The neutron dilution factor becomes

$$f_n^h = \frac{\sigma_{^3He}^h - 2\sigma_p^h}{\sigma_{^3He}^h} = 1 - 2.\frac{\sigma_p^h}{\sigma_{^3He}^h}. \tag{7.19}$$

Next, expressions are found for the semi-inclusive cross-sections in terms of the inclusive ones. This is achieved by multiplying equation 7.19 by two factors, both of which have a value equal to one. Rearranging the resulting equation gives an expression for the dilution factor in terms of measured quantities. Firstly, time integrated luminosities $\int \mathcal{L}$ are used, giving

$$f_n^h = 1 - 2\frac{\sigma_p^h \int \mathcal{L}_p dt}{\sigma_{^3He}^h \int \mathcal{L}_{^3He} dt} \frac{\int \mathcal{L}_{^3He} dt}{\int \mathcal{L}_p dt} = 1 - 2\frac{N_p^h}{N_{^3He}^h} \frac{\int \mathcal{L}_{^3He} dt}{\int \mathcal{L}_p dt}. \tag{7.20}$$

Then equation 7.20 is multiplied by the DIS cross-section for each target,

$$f_n^h = 1 - 2\frac{N_p^h}{N_{^3He}^h} \frac{\int \mathcal{L}_{^3He} dt \; \sigma_{^3He}^{DIS}}{\int \mathcal{L}_p dt \; \sigma_p^{DIS}} \frac{\sigma_p^{DIS}}{\sigma_{^3He}^{DIS}} = 1 - 2\frac{N_p^h N_{^3He}^{DIS}}{N_{^3He}^h N_p^{DIS}} \frac{\sigma_p^{DIS}}{\sigma_{^3He}^{DIS}}, \tag{7.21}$$

Thus, an expression is derived that only contains quantities measured on ^{3}He or proton targets. Substituting structure functions for DIS cross-sections and rearranging gives the final expression,

$$f_n^h = 1 - 2\frac{N_p^h}{N_p^{DIS}} \frac{N_{^3He}^{DIS}}{N_{^3He}^h} \frac{F_2^p}{\left(2F_2^d + F_2^p\right)}, \tag{7.22}$$

where the helium cross-section is formed from deuterium and proton structure functions (assuming $F_2^n = 2F_2^d - F_2^p$). Equation 7.17 can now be rewritten for the semi-inclusive case:

$$A_n^{h(n)}(x, Q^2) = \frac{1}{P_n f_n^h} \left[A_{^3He}^{h(^3He)} - (1 - f_n^h) P_p A_p^{h(p)} \right]. \tag{7.23}$$

The dilution factors used in this work were determined from unpolarised HERMES measurements [64] and are shown in figure 7.3.

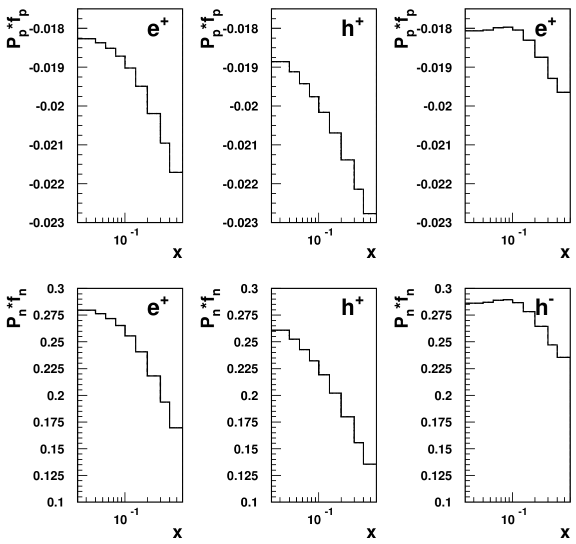

Figure 7.3: The factors $P_p f_p^h$ (top) and $P_n f_n^h$ (bottom) used to unfold the measured ^{3}He asymmetries to the neutron. See equation 7.23.

7.4.2 Deuteron

For the deuteron, the most probable configuration, S-state, has the proton and neutron spins aligned parallel to the nuclear magnetic moment with no relative angular momentum. However, calculations show [68, 69] the probability for the proton and neutron to exist in a state with angular momentum, D-state, ω_D is 0.05 ± 0.01. In the D-state one of the nucleons is anti-aligned, relative to the deuteron magnetic moment. On a global scale, this effect causes the proton and neutron to be slightly depolarised. At present the relative probability for finding the proton or neutron anti-aligned in the D-state is not well known [70, 71]. For this work the proton and neutron are assumed to have equal probability to be anti-aligned. The asymmetries can then be related [72] as

$$A_n^h(x) = 2A_d^h(x)/(1 - 1.5\omega_D) - A_p^h(x), \tag{7.24}$$

which gives

$$\begin{aligned} A_n^h(x) &= 2.16\ A_d^h(x) - \ A_p^h(x), \\ A_d^h(x) &= 0.463\ A_n^h(x) + 0.463\ A_p^h(x). \end{aligned} \tag{7.25}$$

To include the deuterium model into the purity analysis, a "pseudo" dilution is defined such that

$$f_d = P_n f_n^h = P_p(1 - f_n^h) = 0.463. \tag{7.26}$$

With this definition the ^{3}He and deuterium asymmetries can be treated in a similar way in the purity analysis (see section 7.4.4)

7.4.3 Comparison of A_1^n

The treatment of the ^{3}He and deuteron asymmetries in the purity analysis, as described in the next section, does not require the measured asymmetries to be "unfolded" to bare neutron asymmetries. Instead the purities are computed for each of targets. Which ever approach is taken, the purity method still uses the nuclear models described in this section. A comparison of the unfolded neutron asymmetries, therefore provides a valuable cross check of the unfolding methods.

The inclusive and semi-inclusive neutron asymmetries are shown in figure 7.4. The results for ^{3}He are consistent with deuterium. A small systematic difference is evident in the inclusive asymmetry for $0.1 < x < 0.3$. However, considering that many of the parameters used to extract the deuterium asymmetries are not yet finely calibrated, the comparison is good. It is worth noting that the deuterium data have approximately a factor of two better statistical accuracy compared to the ^{3}He data and will therefore have a larger weight in the quark polarisation extraction.

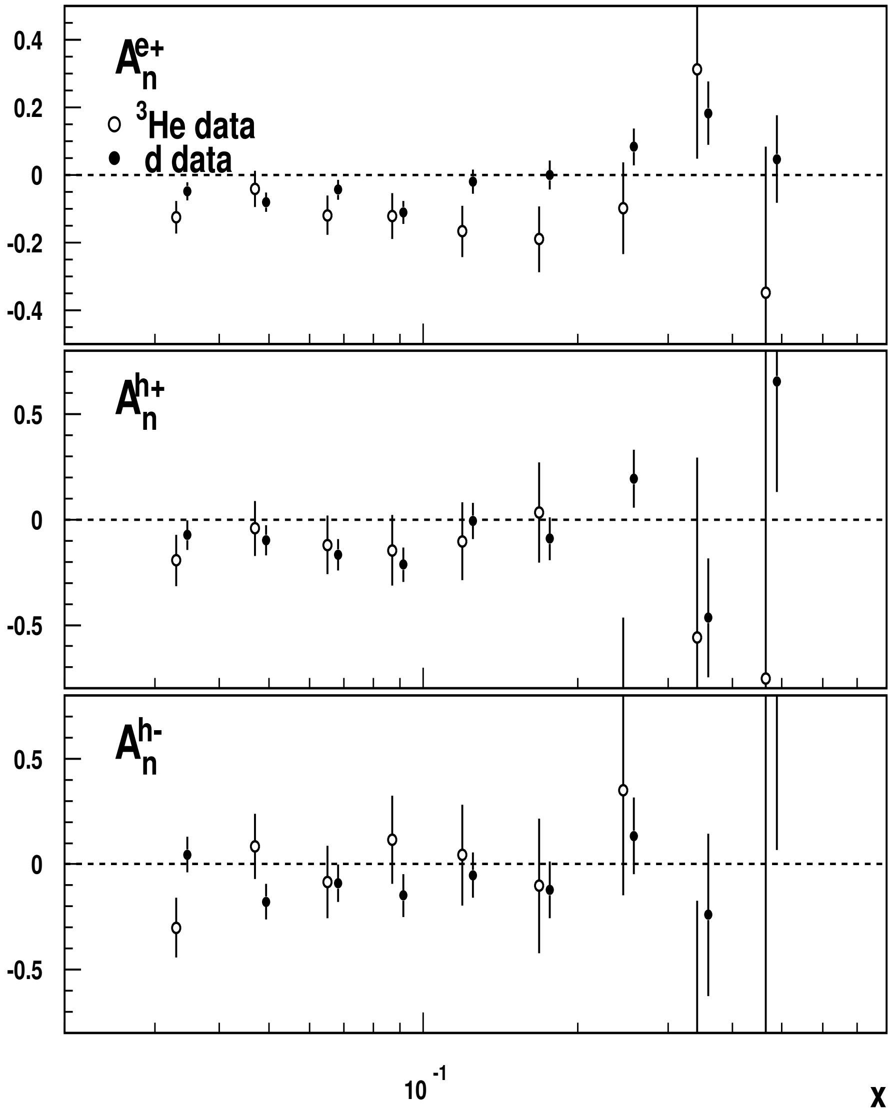

Figure 7.4: Comparison of neutron asymmetries $A_{\|}/D$ derived from asymmetries measured on ^{3}He and D targets. The combined hydrogen data of 1996 and 1997 were used to correct the measured asymmetries as described in the text. Only statistical errors are shown.

7.4.4 Extending the Purity Formalism

The formalism used to express the relation between asymmetries and quark polarisations (equation 2.53) implies that purities are of the type appropriate to the target used in measuring the asymmetry. If asymmetries on the proton and neutron are used, then the appropriate purity matrices would also be determined on the proton and neutron and 2.53 would become

$$\begin{pmatrix} \mathbf{A_p} \\ \mathbf{A_n} \end{pmatrix} = \frac{(1+R)}{(1+\gamma^2)} \begin{pmatrix} \mathbf{P_p} \\ \mathbf{P_n} \end{pmatrix} \mathbf{Q}. \tag{7.27}$$

To include the asymmetries measured on ^{3}He and D in this formalism, the nuclear mixing matrix $\mathbf{N}$ is defined as

$$\mathbf{N} = \begin{pmatrix} 1 & & & & & \\ & \ddots & & & 0 & \\ & & 1 & & & \\ a_{h1} & & & b_{h1} & & \\ & \ddots & & & \ddots & \\ & & a_{hm} & & & b_{hm} \\ f_d & & & f_d & & \\ & \ddots & & & \ddots & \\ & & f_d & & & f_d \end{pmatrix}, \tag{7.28}$$

where $a_{h1} := (1-f_n^h)P_p$ and $b_{h1} := f_n^h P_n$ are the ^{3}He dilution factors and nucleon polarisations and the pseudo dilution factor $f_d := 0.463$ is used to translate the deuterium asymmetries to the neutron.

Defining the mixing matrix 7.28 allows the relation between ^3He (and deuterium) and the neutron asymmetries 7.10 (and 7.23), to be expressed in a vector notation.

$$\begin{pmatrix} \mathbf{A_p} \\ \mathbf{A_{^3He}} \\ \mathbf{A_d} \end{pmatrix} = \frac{(1+R)}{(1+\gamma^2)} \mathbf{P}_{\text{Tot}} \mathbf{Q}, \tag{7.29}$$

where the total purity has been defined as

$$P_{\text{Tot}} = \mathbf{N} \begin{pmatrix} \mathbf{P_p} \\ \mathbf{P_n} \end{pmatrix}. \tag{7.30}$$

It is now possible to solve the master purity relation (2.53) for the nine measured asymmetries.

Technically the fit is performed via the "Single Value Decomposition" (SVD) method [73, 77]. Which was implemented into the analysis via standard C code library functions.

7.5 Results

7.5.1 Quark Polarisation

The results obtained for the flavour symmetric fit, performed for the SU(3) sea assumption, are shown together with HERMES published results for data taken up until 1997 (i.e. excluding deuterium asymmetries) in figure 7.5 and can be found in table B.11 of appendix B. The correlations between the quark polarisations are given in table B.12. The results of this analysis are compatible with the values published in [57].

The results show that the up quarks are polarised in the same direction as the parent nucleon spin and that their polarisation increases with x. The down quarks are polarised in the opposite direction to the parent nucleon, with generally smaller polarisation compared to the up quarks. No strong dependence on x is seen for the down quark polarisation. The strange quark polarisation is consistent with zero to within the statistical and systematic uncertainties.

7.5.2 Polarised Parton Density Functions

The main result of this work, the polarised parton densities for the valence fit performed for the SU(3) symmetric sea assumption, are compared to the SMC results [63] in figure 7.6 and can be found in table B.14 of Appendix B. The correlations between the quark polarisations are given in table B.12.

The results of this analysis are compatible with the SMC values to within the statistical and systematic uncertainties. However, the SMC values tend to be larger over most of the common x range.

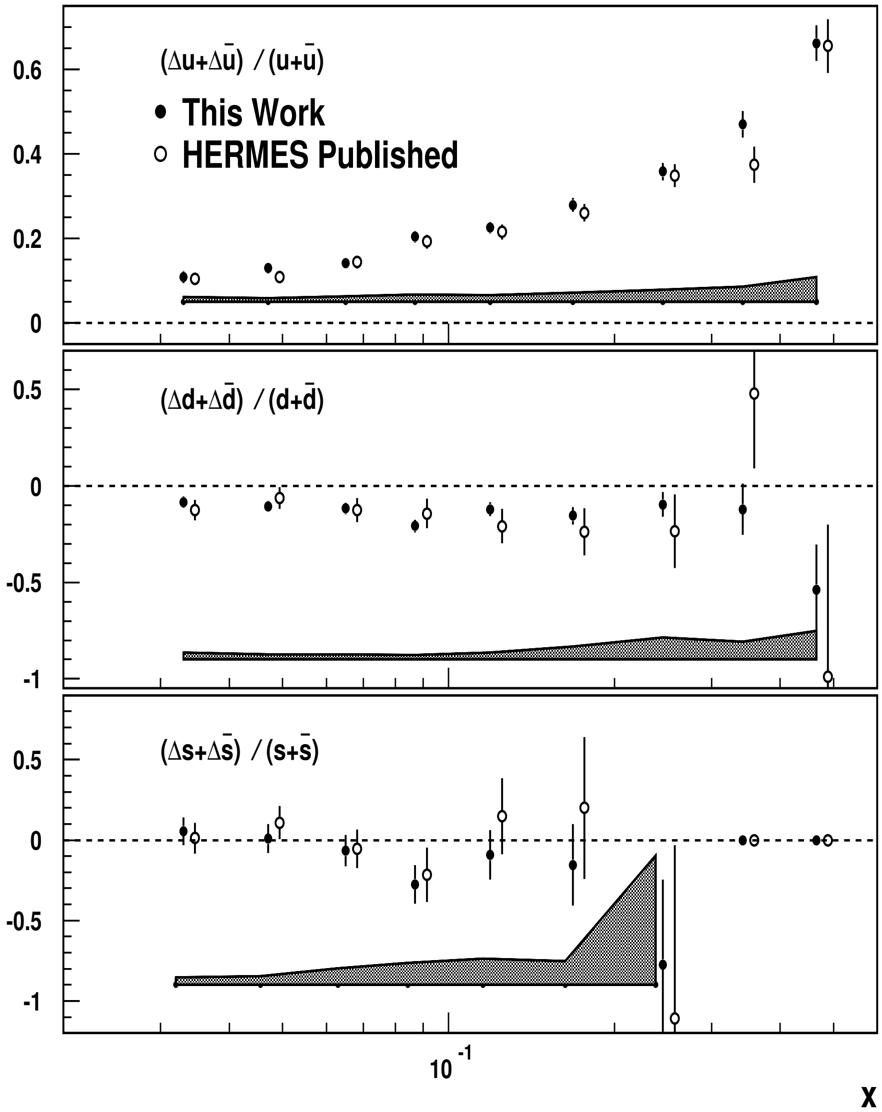

Figure 7.5: The flavour decomposition $(\Delta u(x)+\Delta\overline{u}(x))/(u(x)+\overline{u}(x))$, $(\Delta d(x)+\Delta\overline{d}(x))/(d(x)+\overline{d}(x))$ and $(\Delta\overline{q}(x))/(\overline{q}(x))$ of the quark polarisations as a function of x. An SU(3) flavour symmetric sea was assumed. The error bars show the statistical errors and the bands the systematic uncertainties.

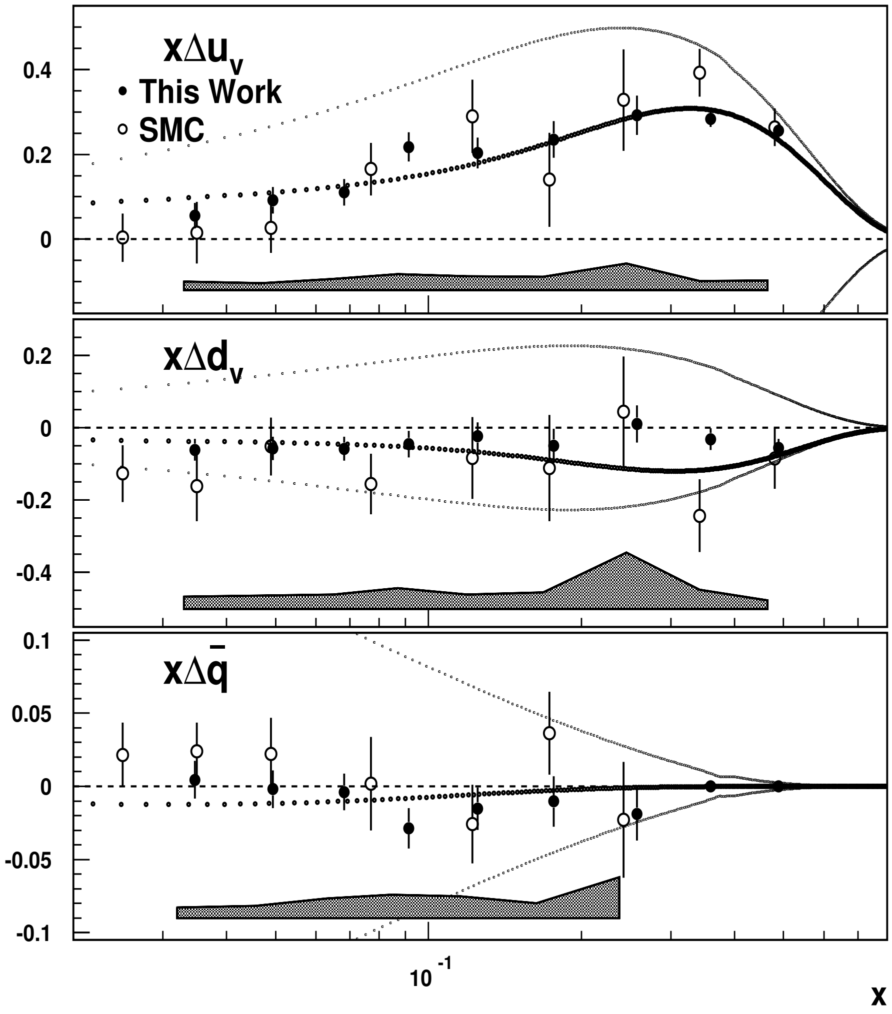

Figure 7.6: The polarised parton density functions separately for valence quarks $x\Delta u_v(x)$,$x\Delta d_v(x)$ and the sea quarks $x\Delta\overline{q}(x)$ as a function of x. The sea quarks were determined with the SU(3) flavour symmetric model. The values are multiplied by x to facilitate easy viewing. The error bars shown are statistical errors and the bands show the systematic uncertainties. The distributions are compared to results from the SMC, extrapolated to $Q^2 = 2.5$ Gev^2. The error bars of the SMC results correspond to the total uncertainty. The light lines represent the positivity limit, $|\Delta q_f(x)/q_f(x)| \leq 1/(1+R(x))$, and the heavy lines are the parameterisation from Gehrman and Stirling ('Gluon A', LO) [74].

7.6 Systematic Error

In this section the various systematic uncertainties on the extracted quark polarisations, which contribute to the error band of figures 7.5 and 7.6 will be discussed. The total systematic error on the results originates from two different classes of input uncertainties: systematic errors on the measurement of the asymmetries and the variation of the purity matrix when different unpolarised parton density functions and fragmentation models are used for its generation.

Although the 1998 measured deuteron asymmetries compare well to the SMC data, it must be stressed that they were extracted from the first iteration of HERMES Reconstruction Code (HRC) production of the 1998 data. Consequently, the exact calibration of many parameters effecting the systematic error, such as the target polarisation, has not yet been determined. To account for the uncertainties originating in the deuterium data, values similar to those of 1996 have been used where appropriate, else conservative first estimates were made.

7.6.1 Errors on the Asymmetries

The measured asymmetries have statistical correlations as described in Appendix A.2. It is therefore necessary to consider the correlation of the experimental uncertainty among the asymmetries. In analogy to the statistical covariance, defined in A.7, the asymmetry systematic covariance is now defined as

$$\mathbf{C}_A^{sys} = cov(A^i A^j). \tag{7.31}$$

The dominant contributions to the asymmetry systematic covariance will now be considered.

Target Polarisation

The ^3He target has a relative polarisation uncertainty of $\frac{\delta P_{^3He}}{P} = 5\%$. The covariance for this uncertainty is

$$C_{A_{^3He}}^{P_{Targ}} = A^i_{^3He} A^j_{^3He} \left(\frac{\delta P_{^3He}}{P} \right)^2 . \tag{7.32}$$

The polarisation uncertainty of the hydrogen and deuterium targets are not correlated to the ^{3}He target since both the sources and the polarimeters were implemented using different techniques.

The uncertainty for the 1997 hydrogen target has been determined to be 4.5% [64]. In order to improve the uncertainty for asymmetries measured in the hydrogen targets commissioning year (1996), the 1996 inclusive asymmetries were renormalised by a constant, k, to those of 1997. The statistical uncertainty in determining k corresponds to a polarisation uncertainty of 4%. The 1996 asymmetries are then correlated to both the 1997 uncertainty and the uncertainty due to k, giving an overall uncertainty of 6%. The covariance for the hydrogen target is

$$\mathbf{C}_{A_p}^{Targ} = A_p^i A_p^j \left((\frac{\delta P_{97}}{P})^2 + \rho_{96} (\frac{\delta k}{k})^2 \right), \tag{7.33}$$

where ρ_{96} is one within 1996 and zero otherwise.

No uncertainty has yet been determined for the polarisation of the deuterium target. Also, no corrections to the raw polarisation measurement are available in the "a" production. As a worst case the uncertainty will be taken as $\frac{\delta P_d}{P} =$ 10% and is assumed to be uncorrelated with the hydrogen targets polarisation uncertainty. The covariance for the deuterium target is then given by

$$C_{A_d}^{Targ} = A_d^i A_d^j \left(\frac{\delta P_d}{P} \right)^2 . \tag{7.34}$$

Beam Polarisation

The beam polarisation was measured with the same apparatus for both sets of asymmetries. Therefore parts of the systematic error are correlated. The main contribution to the uncertainty is given by a calibration constant which is derived as a function of the rise time constant. This constant has a fractional error of $\delta P_{\rm rise} = 3.26\%$ and is 100% correlated for all years. Another contributions from "point-to-point" [64] instabilities have values $\frac{\delta P_{\rm point}}{P} = 2.2\%, 0.9\%, 0.9\%, 0.9\%$ in 95, 96, 97 and 98. Where it was assumed the 98 value was equal to the 96 value. The point-to-point contributions are 100% correlated between asymmetries in one year, but not between years. The contribution to the covariance matrix is then given by

$$\mathbf{C}_A^{Beam} = A^i A^j \left[(\frac{\delta P_{\text{rise}}}{P})^2 + \rho_{\text{point}} (\frac{\delta P_{\text{point}}}{P})^2 \right], \tag{7.35}$$

where ρ_{point} has a value of one for asymmetries of the same year and zero otherwise.

Smearing and Radiative Corrections

As discussed in section 5.7, the measured hydrogen asymmetries have to be corrected for kinematic smearing. The uncertainty in the smearing correction is assumed to be completely correlated between asymmetries of one year. No smearing corrections have been applied to the deuteron asymmetries, instead the magnitude of the hydrogen smearing correction was taken as a worst case for the uncertainty.

The radiative corrections are taken as an uncertainty rather than correcting the asymmetries and apply only to the inclusive asymmetries. The covariance due to smearing and radiative corrections can now be written as

$$\mathbf{C}_A^{Smear,Rad} = A^i A^j (\frac{\delta k_{\text{smear}}}{k})^2 + \rho_{\text{inclusive}} (\Delta_{RC})^2. \tag{7.36}$$

where $\rho_{\text{inclusive}}$ has a value of one when both asymmetries are inclusive and zero otherwise.

Yield fluctuations

The yield fluctuations determined from the false asymmetry study of section 6.4 were found by averaging over x. To apply an uncertainty to each x bin individually, it is assume the yield fluctuation acts on each bin coherently. No uncertainty from yield fluctuations has been assigned for 1998. Assuming the yield fluctuations y (= $\%\sigma_{\text{stat}}$ as defined in table 6.2) have the same correlations as the asymmetries, the covariance is given by

$$\mathbf{C}_A^{Yield} = cov(A_i, A_j)\delta A_i \delta A_j \left(\sqrt{(1+y_i^2)(1+y_j^2)} - 1 \right) \tag{7.37}$$

Systematic error of $R(x, Q^2)$

The parameterisation of R has an associated uncertainty of about 4% which, due to equation 2.49, is treated as a correlated uncertainty on the measured asymmetries. As the photon depolarisation factor also depends on $R(x, Q^2)$ [64], both contributions are accounted for in the covariance matrix

$$\mathbf{C}_A^R = A_i A_j \delta R^2, \tag{7.38}$$

where

$$\delta R = \frac{y}{(2-y)(1+R(x,Q^2))^2} \Delta R(x, Q^2) \tag{7.39}$$

is evaluated for the mean kinematic values of each x bin.

Uncertainty on the A_2 correction

The uncertainty on the A_2 correction was taken to be the same as the magnitude of the correction itself. Because of the small kinematic factor $(\gamma - \eta)$ appearing in the A_2 correction term, this uncertainty whose covariance is given by

$$\mathbf{C}_A^{A_2} = A_i A_j \delta A_2, \tag{7.40}$$

is typically less that 1%.

7.6.2 Errors on the Purities

Two sources of uncertainty for the determination of the purities have been considered [64]. Contributions may arise from uncertainties in the unpolarised PDFs and the fragmentation model. To estimate the uncertainty on the purities due to the PDFs, the difference between alternative unpolarised PDF sets were used. The uncertainty due to the fragmentation model was taken as the difference between the LUND and independent fragmentation models (see section 2.5.2). For the highest two x bins where the sea purity is set to zero, the uncertainty covariance matrix for the purities $\mathbf{C}_Q^{\mathrm{Pur}}$ also includes the positivity limit for the sea quarks. Note that $\mathbf{C}_Q^{\mathrm{Pur}}$ contains uncertainties on the quark polarisations (as opposed to the asymmetries).

7.6.3 The Total Systematic Uncertainty

The total asymmetry systematic uncertainty is the square root of the diagonal element of the matrix,

$$\mathbf{C}_A^{sys} = \mathbf{C}_A^{P_{Targ}} + \mathbf{C}_A^{Beam} + \mathbf{C}_A^{Smear,Rad} + \mathbf{C}_A^{Yield} + \mathbf{C}_A^{R} + \mathbf{C}_A^{A_2}. \tag{7.41}$$

The contributions of the asymmetry systematic errors to the quark polarisations are estimated by performing the fit 2.55 once with a matrix of statistical covariances $\mathbf{C}_\mathbf{A}^\mathbf{stat}$ only and once with the total covariances $\mathbf{C}_\mathbf{A}^\mathbf{tot} = \mathbf{C}_\mathbf{A}^\mathbf{stat} + \mathbf{C}_\mathbf{A}^\mathbf{sys}$. The difference of the diagonal elements in the these covariance matrices is interpreted as the squared systematic error.

$$\mathbf{C}_\mathbf{Q}^\mathbf{sys} = \mathbf{C}_\mathbf{A}^\mathbf{tot} - \mathbf{C}_\mathbf{A}^\mathbf{stat}. \tag{7.42}$$

For the final systematic error the contribution from the purity uncertainty is added.

$$\mathbf{C}_\mathbf{Q}^\mathbf{SYS} = \mathbf{C}_\mathbf{Q}^\mathbf{sys} + \mathbf{C}_\mathbf{Q}^\mathbf{Pur}. \tag{7.43}$$

The relative contributions of the various sources of systematic error to the quark polarisations are shown in figure 7.7.

7.7 Integrals of the Polarised Parton Densities

The integral of the polarised PDF, for any given flavour, over all x, is equal to the fraction of the proton spin originating from that flavour. The valence and sea quark polarised PDFs have been measured in the experimentally accessible region of $0.023 < x < 0.6$. Therefore, to obtain the fraction of proton spin from each quark type, the integrals must also be determined for the two unmeasured regions, i.e at low x:$0 < x < 0.023$ and at high x:$0.6 < x < 1$. The method for each region will now be discussed and the results presented in table 7.1.

Low x region

No reliable prediction exists for the behaviour of the polarised PDFs at low x [72]. Nonetheless, in order to determine the integral over all x , some meaningful

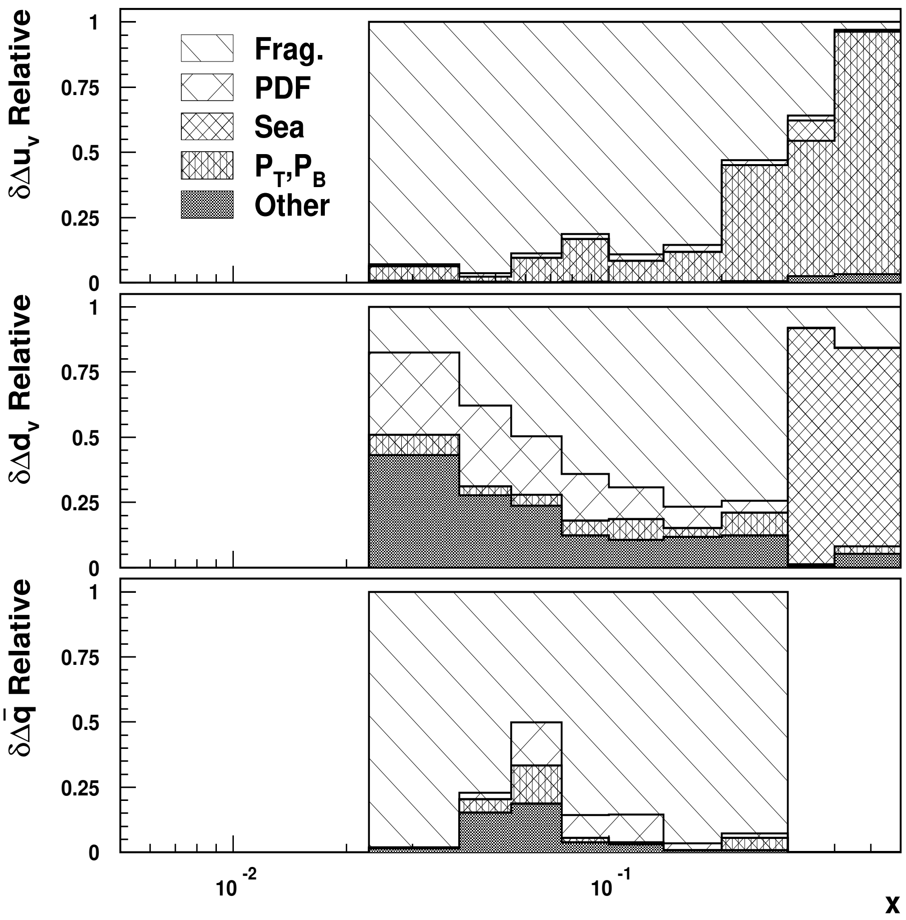

Figure 7.7: The relative contributions of the sources of systematic uncertainty for the fit of valence quark polarisations. Each of the following quantities is plotted as as fraction of the total uncertainty in each bin; (Frag) fragmentation, (PDF) unpolarised parton density functions, (Sea) The unpolarised sea assumption for the two highest bins in x and (P_T, P_B) the combined contribution from uncertainty in the beam and target polarisation and (Other) includes the contribution from the smearing, radiative and A_2 corrections as well as the uncertainty due to $R(x, Q^2)$. For the absolute contributions see tables B.15, B.16 and B.17.

approximation must be made. The approach taken here follows that presented in previous analysis of HERMES data [64], where a constant value in the low x region is assumed. This value is found by fitting the lowest three bins in x with a constant k. The systematic uncertainty is then taken as the statistical error on the fit.

Measured x region

The same approach as [64] was used to determined the integrals in the measured region. The quark polarisations are assumed to have constant values within each bin. The first moment of the measured distributions are then determined by,

$$\begin{aligned}(\Delta q^{\text{measured}}|_{Q^2=2.5\text{GeV}} &= \int_{0.023}^{0.6} dx(\Delta q(x)|_{Q^2=2.5\text{GeV}} \\ &= \sum_{i=1}^{9} \left(\frac{\Delta q}{q}|_i \int_{x_i}^{x_{i+1}} dx(q(x)|_{Q^2=2.5\text{GeV}} \right). \qquad (7.44)\end{aligned}$$

The statistical uncertainty is determined by adding the the error for each x bin in quadrature. The systematic uncertainty is taken as the linear addition of the systematic error on each x bin.

High x region

The value of the integral for $x > 0.6$ was estimated by integrating the polarised PDFs of CTEQ [60] over this region. The contribution is small as both the polarised and unpolarised distributions have a sharp drop-off above $x = 0.6$. The systematic uncertainty is taken as the positivity limit.

The Integral Results

The contributions from each of the x regions discussed above and the sum over all regions are given in table 7.1. All results of this work are for the SU(3) flavour symmetric model of the sea. The difference between the two polarised models of the sea (equations 7.5 and 7.8) was found to be small compared to the statistical and systematic uncertainties. This shows that the statistical precision is not yet sufficient to distinguish the relationship between the polarisations of different flavoured sea quarks.

Except for the ^{3}He asymmetries, the analysis presented in this thesis is independent of that used to determine the published results for the polarised PDFs [57], extracted from HERMES data taken up until 1997. The results of this thesis, where deuterium asymmetries measured at HERMES have been included for the first time, are consistent with those of published previously by HERMES [57].

x-Range	0. – 0.023	0.023-0.6	0.6 – 1	0 – 1
Δu_v	0.033	0.594±0.037±0.099	0.013	0.640±0.037±0.183
Δd_v	-0.032	-0.130±0.041±0.174	-0.001	-0.157±0.041±0.192
$\Delta u + \Delta \overline{u}$	0.038	0.549±0.012±0.038	0.013	0.600±0.012±0.052
$\Delta d + \Delta \overline{d}$	-0.025	-0.197±0.020±0.061	-0.001	-0.223±0.020±0.071
$\Delta \overline{u}$	0.001	-0.036±0.021±0.036	0	-0.035±0.021±0.036
$\Delta \overline{d}$	-0.001	-0.016±0.020±0.058	0	-0.017±0.020±0.058
$\Delta \overline{s}$	-0.001	-0.015±0.009±0.024	0	-0.016±0.009±0.024
a_0	0.011	0.322±0.037±0.113	0.010	0.343±0.037±0.114
a_3	0.063	0.746±0.052±0.081	0.019	0.828±0.052±0.090
a_8	0.009	0.292±0.076±0.130	0.009	0.331±0.076±0.142

Table 7.1: First moments of the polarised parton densities for $Q^2 = 2.5$ GeV. The valence quark integrals were determined from the SU(3) sea quark fit.

The results for the measured region integrals are compared directly to those for the SMC experiment over the common x range and are given in table 7.2. This removes the large theoretical uncertainty for extrapolating to unmeasured regions, while allowing the results to be compared to an experiment with different sources of systematic error. The SMC values were evolved to $Q^2 = 2.5$ before the integration was performed over the HERMES measured x-range. The results agree well with the SMC values. With the addition of the deuterium data the statistical precision of the down valence quarks is comparable with that of the up valence quarks.

	This Thesis	SMC
Δu_v	0.59±0.04±0.10	0.59±0.08±0.07
Δd_v	-0.13±0.04±0.17	-0.33±0.11±0.09
$\Delta \overline{u}$	-0.04±0.02±0.04	0.02±0.03±0.02
$\Delta \overline{d}$	-0.02±0.02±0.06	0.02±0.03±0.02

Table 7.2: Comparison of the integrals from this thesis for valence and sea spin distributions with SMC results [63]. The SMC values are extrapolated to $Q^2 = 2.5$ GeV^2 and integrated over the HERMES x-range of $0.023 < x < 0.6$.

The integrals over the entire x range are compared to results obtained from an SU(3) analysis of hyperon decay and inclusive proton data (as discussed in section 2.4.3) in table 7.3. For consistency with similar analyses [57, 64] the updated values are taken [76]. The results of this thesis are in reasonable agreement with the with the SU(3) analysis although the quark polarisations are lower for each of the three flavours. The result for the strange sea polarisation is consistent with both zero and the significantly negative SU(3) result given in table 7.3.

	This Thesis	SU(3) Analysis
$\Delta u + \Delta\overline{u}$	0.60±0.01±0.05	0.66±0.03
$\Delta d + \Delta\overline{d}$	-0.22±0.02±0.07	-0.35±0.03
$\Delta s + \Delta\overline{s}$	-0.03±0.03±0.05	-0.08±0.01
a_0	0.34±0.04±0.11	0.23±0.04
a_3	0.83±0.05±0.09	1.01±0.05
a_8	0.33±0.08±0.14	0.46±0.03

Table 7.3: The integrated quark distributions over all x compared to an SU(3) symmetry analysis of inclusive data and hyperon decay [76]. All values have been determined for $Q^2 = 2.5$ GeV^2.

	This Thesis	Lattice QCD	Q^2 (GeV^2)
Δu_v	0.64±0.04±0.18	0.84±0.05	5
Δd_v	-0.16±0.04±0.19	-0.25±0.02	5

Table 7.4: Comparison of the result for the integral of the valence quark distributions compared to lattice QCD [75]. The measured values are at $Q^2 = 2.5$ GeV^2 and the lattice results are for $Q^2 = 5$ GeV^2

The integrals for the valence quarks over the entire x-range are compared to values calculated with lattice QCD techniques [75] in table 7.4. The measured results are consistent with the lattice values. However, both results lie below the prediction. Also, the results are compatible due to the large systematic uncertainty on the valence results, due to the low-x extrapolation.

Chapter 8

Conclusion

Inclusive and semi-inclusive proton asymmetries have been extracted from data collected at HERMES in 1996 and 1997. Preliminary asymmetries on the deuteron have also been extracted from HERMES data collected in 1998 and the Spring of 1999. Systematic studies on the extracted proton asymmetries showed a significant difference between the the negative hadron asymmetries of 1996 and 1997. Despite extensive studies no definite conclusion about the origin of this difference was reached. However, the extracted asymmetries for all years are compatible with previous asymmetry measurements made at SMC, where different sources of experimental uncertainty are present. The neutron asymmetries derived from the ^{3}He and deuteron asymmetries measured at HERMES were also in good agreement. The ^{3}He asymmetries, measured previously at HERMES, were combined with these proton and deuterium asymmetry results and the quark polarisations of the nucleon were extracted via the purity method.

The purity method for extracting the quark polarisations of the nucleon from measured asymmetries was first used by SMC and has been developed here to allow the inclusion of the HERMES deuterium data. The method relates asymmetries to linear combinations of quark polarisations via a purity matrix, which was determined with Monte Carlo methods using information from unpolarised data. The quark polarisations have been extracted as a function of the Bjorken scaling variable, x, allowing the polarised parton density functions to be determined.

The quark spin distributions were found to be in good agreement with measurements from SMC and are consistent with the CTEQ [60] polarised PDF parameterisations. These results are the most precise determination of the quark spin distribution to date. The addition of the deuterium data has reduced the statistical error on the d_v quark distribution by approximately 50% relative to the previously published HERMES results.

The integrals of the spin distributions, over the measured region of $0.023 < x < 0.6$, are compatible with values from SMC. The integrals over the entire x range are consistent with the predictions from an SU(3) analysis of inclusive data.

In summary, the conclusions presented here are in agreement with those given in the publication of HERMES polarised data collected up until 1997. Although the statistical precision of this new analysis is greater, the larger systematic uncertainly on the final results gives a modest improvement in the overall precision.

Further systematic studies of the deuteron data will improve the uncertainty in the calibration of parameters effecting asymmetries, thus reducing the systematic uncertainties. HERMES continues to collect polarised Deuterium data in 1999, which will further reduced the statistical error on the polarised quark distributions in future analyses.

In 1998 the Čerenkov detector was upgraded to a Ring Imaging Čerenkov detector (RICH) to provide identification of pions, kaons and protons over most of the momentum rage. Because of this hadron identification ability and the increasing aggregate of data, a complete polarisation extraction for all flavours, without the need to assume an SU(3) flavour symmetric sea, may soon be possible.

Appendix A

Error Analysis for the Particle Count Rates and Asymmetries

A full derivation of the error and covariance of the particle count rates and asymmetries can be found in [77], the main results are summarised here for easy reference.

A.1 Error and Covariances of the Particle Count Rates

The variance of the inclusive positrons $\sigma^2_{N_{e^+}}$ is equal to the number of positrons detected N_{e^+} as they are Poisson distributed. However, in the case of the hadrons:

$$\sigma^2_{N_h} = N_{e^+} \langle\, (n_i^h)^2 \,\rangle = N_h \frac{\langle\, (n_i^h)^2 \,\rangle}{\langle\, n_i^h \,\rangle} \tag{A.1}$$

where n_i^h is the mean number of i hadrons per event and N_h is the number of detected hadrons. This results is different from the value N_h that one would expect for a Poisson distribution.

The statistical covariances for the numbers of measured particles can be expressed as:

$$\begin{aligned} cov(N_{h1}, N_{h2}) &= \langle\, N_{h1} N_{h2} \,\rangle - \langle\, N_{h1} \,\rangle \langle\, N_{h2} \,\rangle \\ &= N_{e^2} \langle\, n_i^{h_1} n_i^{h_2} \,\rangle, \\ cov(N_{e^+}, N_{h2}) &= N_{e^2} n^h. \end{aligned} \tag{A.2}$$

where $n_i^{e^+} = 1$ was used. The correlation coefficients for the particle numbers are expressed as:

$$\begin{aligned} cor(N_{h1}, N_{h2}) &= \frac{cov(N_{h1}, N_{h2})}{\sigma_{h_1}\sigma_{h_2}} \\ &= \frac{\langle\ n_i^{h_1} n_i^{h_2}\ \rangle}{\sqrt{\langle\ (n_i^{h_1})^2\ \rangle\langle\ (n_i^{h_2})^2\ \rangle}} \\ cor(N_{e^+}, N_{h2}) &= \frac{n_i^h}{\sqrt{\langle\ (n_i^h)^2\ \rangle}}. \end{aligned} \tag{A.3}$$

A.2 Error and Covariances of the Asymmetries

Writing the asymmetry for a particle (e.g. $h-$) as:

$$\begin{aligned} A^{N^{h^-}} &= \frac{N_-^{h^-} L_+ - N_+^{h^-} L_-}{N_-^{h^-} D_+^{h^+} P_+ L_+ + N_+^{h^+} D_-^{h^-} P_- L_-}, \\ &\equiv \frac{X}{Y}. \end{aligned} \tag{A.4}$$

allows the statistical error on the asymmetry to be expressed in terms of the numerator and denominator. Such that,

$$(\sigma_{A^{h^-}})^2 = \left[\sigma_{N_-^{h^-}} \frac{YL_+ - XD_+^{h^-} P_+ L_+}{Y^2}\right]^2 + \left[\sigma_{N_+^{h^-}} \frac{-YL_- - XD_-^{h^-} P_- L_-}{Y^2}\right]^2 \tag{A.5}$$

where $\sigma_{N^{h^-}}$ is the error on each count rate as defined in A.1.

The covariance matrix of the asymmetries is given by the transformation

$$\mathbf{C}_A = \frac{\partial \mathbf{A}}{\partial \mathbf{N}} \mathbf{C}_{\mathbf{N}} \left(\frac{\partial \mathbf{A}}{\partial \mathbf{N}}\right)^T \tag{A.6}$$

Making the approximations $N_{i\pm} \approx 1/2N_i$ and $|\frac{\partial A}{\partial N_+}| \approx |\frac{\partial A}{\partial N_-}|$ allows A.6 to be written as:

$$cov(A_i, A_j) = \frac{\sigma_{A_i}\sigma_{A_j}}{\sigma_{N_i}\sigma_{N_j}}, \tag{A.7}$$

and the correlation coefficients become

$$cor(\mathbf{A}) \approx cor(\mathbf{N}). \tag{A.8}$$

Appendix B

Tables of Results

Kinematic Bins							
Bin	x range	$\langle x \rangle$	$\langle Q^2 \rangle$	$\langle D \rangle$	$\langle \gamma \rangle$	$\langle \eta \rangle$	$\langle R \rangle$
1	0.023–0.040	0.033	1.211	0.708	0.056	0.025	0.443
2	0.040–0.055	0.048	1.459	0.582	0.075	0.043	0.384
3	0.055–0.075	0.065	1.697	0.495	0.095	0.063	0.348
4	0.075–0.100	0.087	1.945	0.427	0.121	0.087	0.315
5	0.100–0.140	0.118	2.220	0.363	0.156	0.121	0.281
6	0.140–0.200	0.165	2.524	0.300	0.208	0.172	0.247
7	0.200–0.300	0.238	2.844	0.239	0.288	0.249	0.216
8	0.300–0.400	0.337	3.526	0.210	0.361	0.318	0.179
9	0.400–0.600	0.447	4.964	0.219	0.407	0.355	0.132

Table B.1: The kinematic binning used in the analysis. The values are taken from the hydrogen data.

Particle Yields				
Particle	Year			
	1995	1996	1997	1998
e^+	2157652	684765	1529249	856893
e^-	21488	10278	24780	13014
h^+	284249	94223	208132	98546
h^-	177907	53375	117124	62387
π^+	53088	39153	90228	0
π^-	37803	26892	61272	0

Table B.2: Particle Yields after all cuts.

^{3}He Asymmetries (1995)						
Bin	A^{e^+}	δA^{e^+}	A^{h^+}	δA^{h^+}	A^{h^-}	δA^{h^-}
1	-0.034	0.013	-0.051	0.032	-0.079	0.037
2	-0.007	0.014	-0.011	0.033	0.021	0.039
3	-0.026	0.015	-0.030	0.034	-0.021	0.042
4	-0.023	0.018	-0.035	0.039	0.027	0.049
5	-0.032	0.019	-0.024	0.040	0.009	0.052
6	-0.036	0.023	0.006	0.048	-0.022	0.065
7	-0.004	0.028	-0.150	0.065	0.062	0.089
8	0.073	0.046	-0.088	0.132	-0.220	0.191
9	-0.014	0.065	-0.104	0.273	0.291	0.613

Table B.3: The 1995 $\frac{A_\parallel}{D}$ asymmetries measured on ^{3}He. The errors are statistical only.

Hydrogen Asymmetries (1996)						
Bin	A^{e^+}	δA^{e^+}	A^{h^+}	δA^{h^+}	A^{h^-}	δA^{h^-}
1	0.086	0.014	0.074	0.035	0.065	0.042
2	0.102	0.015	0.107	0.036	0.088	0.044
3	0.122	0.016	0.155	0.037	0.070	0.046
4	0.173	0.018	0.184	0.041	0.147	0.054
5	0.225	0.019	0.262	0.043	0.252	0.057
6	0.248	0.023	0.218	0.051	0.290	0.070
7	0.349	0.029	0.498	0.067	0.311	0.096
8	0.371	0.049	0.227	0.133	0.462	0.195
9	0.597	0.066	1.049	0.264	0.144	0.419

Table B.4: The 1996 $\frac{A_\parallel}{D}$ asymmetries measured on hydrogen. The errors are statistical only.

Hydrogen Asymmetries (1997)						
Bin	A^{e^+}	δA^{e^+}	A^{h^+}	δA^{h^+}	A^{h^-}	δA^{h^-}
1	0.079	0.008	0.092	0.021	0.043	0.025
2	0.106	0.009	0.123	0.021	0.089	0.027
3	0.118	0.010	0.141	0.022	0.069	0.028
4	0.168	0.011	0.203	0.025	0.018	0.032
5	0.203	0.012	0.258	0.026	0.170	0.035
6	0.271	0.014	0.267	0.031	0.178	0.043
7	0.345	0.018	0.400	0.041	0.214	0.060
8	0.501	0.030	0.500	0.082	0.679	0.121
9	0.644	0.040	0.515	0.161	0.062	0.250

Table B.5: The 1997 $\frac{A_\parallel}{D}$ asymmetries measured on hydrogen. The errors are statistical only.

Deuterium Asymmetries (1998)						
Bin	A^{e^+}	δA^{e^+}	A^{h^+}	δA^{h^+}	A^{h^-}	δA^{h^-}
1	0.015	0.012	0.007	0.032	0.044	0.017
2	0.011	0.013	0.010	0.032	-0.041	0.012
3	0.035	0.013	-0.010	0.033	-0.010	0.009
4	0.027	0.015	-0.008	0.037	-0.043	0.013
5	0.088	0.016	0.117	0.038	0.066	0.014
6	0.122	0.019	0.075	0.045	0.041	0.018
7	0.199	0.024	0.288	0.061	0.174	0.017
8	0.299	0.042	-0.022	0.127	0.173	0.049
9	0.314	0.058	0.613	0.233	0.417	0.101

Table B.6: The 1998 $\frac{A_\parallel}{D}$ asymmetries measured on deuterium. The errors are statistical only.

	^{3}He				Hydrogen			
Bin	n_{h^+}	$\frac{<N^2_{h^+}>}{n_{h^+}}$	n_{h^-}	$\frac{<N^2_{h^-}>}{n_{h^-}}$	n_{h^+}	$\frac{<N^2_{h^+}>}{n_{h^+}}$	n_{h^-}	$\frac{<N^2_{h^-}>}{n_{h^-}}$
1	0.152	1.069	0.111	1.053	0.167	1.073	0.110	1.050
2	0.180	1.065	0.124	1.049	0.195	1.074	0.122	1.047
3	0.182	1.061	0.119	1.045	0.198	1.068	0.119	1.043
4	0.168	1.057	0.104	1.035	0.188	1.064	0.105	1.035
5	0.140	1.055	0.082	1.030	0.159	1.057	0.083	1.030
6	0.096	1.052	0.053	1.029	0.110	1.059	0.054	1.026
7	0.053	1.046	0.027	1.027	0.062	1.053	0.028	1.023
8	0.029	1.043	0.014	1.016	0.033	1.038	0.014	1.018
9	0.015	1.034	0.006	1.017	0.015	1.047	0.006	1.013

Table B.7: Hadron Multiplicities for ^{3}He and hydrogen, taken from the data and averaged over both spin states.

	Deuterium			
Bin	n_{h^+}	$\frac{<N^2_{h^+}>}{n_{h^+}}$	n_{h^-}	$\frac{<N^2_{h^-}>}{n_{h^-}}$
1	0.139	1.066	0.097	1.050
2	0.164	1.066	0.114	1.048
3	0.163	1.058	0.110	1.042
4	0.153	1.053	0.096	1.035
5	0.132	1.049	0.079	1.034
6	0.094	1.049	0.052	1.026
7	0.053	1.043	0.030	1.028
8	0.027	1.025	0.015	1.009
9	0.015	1.033	0.007	1.000

Table B.8: Hadron Multiplicities for deuterium, taken from the data and averaged over both spin states.

	^{3}He			Deuteron		
	Cor	Cor	Cor	Cor	Cor	Cor
Bin	(A^{e^+}, A^{h^+})	(A^{e^+}, A^{h^-})	(A^{h^+}, A^{h^-})	(A^{e^+}, A^{h^+})	(A^{e^+}, A^{h^-})	(A^{h^+}, A^{h^-})
1	0.283	0.208	0.0428	0.214	0.152	0.029
2	0.324	0.224	0.0490	0.255	0.178	0.035
3	0.335	0.221	0.0473	0.275	0.185	0.038
4	0.332	0.205	0.0418	0.283	0.173	0.032
5	0.309	0.179	0.0339	0.274	0.162	0.027
6	0.259	0.142	0.0243	0.236	0.131	0.020
7	0.198	0.101	0.0159	0.181	0.100	0.014
8	0.148	0.071	0.0077	0.136	0.072	0.007
9	0.106	0.048	0.0038	0.097	0.048	0.007

Table B.9: Correlations of the measured ^{3}He and deuteron asymmetries.

	96 hydrogen			97 hydrogen		
Bin	Cor	Cor	Cor	Cor	Cor	Cor
Bin	(A^{e^+}, A^{h^+})	(A^{e^+}, A^{h^-})	(A^{h^+}, A^{h^-})	(A^{e^+}, A^{h^+})	(A^{e^+}, A^{h^-})	(A^{h^+}, A^{h^-})
1	0.385	0.257	0.064	0.383	0.253	0.063
2	0.423	0.268	0.068	0.416	0.260	0.066
3	0.427	0.262	0.066	0.425	0.252	0.064
4	0.420	0.235	0.058	0.415	0.232	0.057
5	0.388	0.205	0.045	0.384	0.199	0.046
6	0.325	0.156	0.033	0.320	0.159	0.034
7	0.247	0.113	0.022	0.239	0.120	0.021
8	0.180	0.077	0.011	0.176	0.075	0.013
9	0.122	0.049	0.006	0.119	0.051	0.006

Table B.10: Correlations of the measured hydrogen asymmetries.

$\langle x \rangle$	$\langle Q^2 \rangle$	$\frac{\Delta u+\Delta\overline{u}}{u+\overline{u}}$	$\frac{\Delta d+\Delta\overline{u}}{d+\overline{u}}$	$\frac{\Delta\overline{q}_{\mathrm{SU(3)}}}{\overline{q}_{\mathrm{SU(3)}}}$	χ^2/d.o.f
0.033	1.211	0.108±0.015±0.011	-0.084±0.028±0.036	0.055±0.087±0.046	0.89
0.048	1.459	0.130±0.013±0.008	-0.108±0.029±0.028	0.009±0.091±0.055	0.66
0.065	1.697	0.141±0.012±0.012	-0.118±0.029±0.026	-0.066±0.098±0.102	0.53
0.087	1.945	0.204±0.013±0.016	-0.207±0.033±0.024	-0.274±0.120±0.138	1.59
0.118	2.220	0.225±0.014±0.016	-0.121±0.035±0.036	-0.093±0.153±0.163	1.11
0.165	2.524	0.278±0.016±0.021	-0.155±0.045±0.066	-0.154±0.253±0.147	0.91
0.238	2.844	0.358±0.021±0.028	-0.096±0.064±0.113	-0.774±0.528±0.802	2.36
0.337	3.526	0.470±0.031±0.036	-0.122±0.133±0.092	–	2.59
0.447	4.964	0.662±0.042±0.059	-0.538±0.235±149	–	1.08

Table B.11: Extracted quark polarisations as a function of x for the flavour symmetric fit and equal sea polarisation model.

Bin	Cor $(\frac{\Delta u_v}{u_v}, \frac{\Delta d_v}{d_v})$	Cor $(\frac{\Delta u_v}{u_v}, \frac{\Delta \overline{q}_{\mathrm{SU(3)}}}{\overline{q}_{\mathrm{SU(3)}}})$	Cor $(\frac{\Delta d_v}{d_v}, \frac{\Delta \overline{q}_{\mathrm{SU(3)}}}{\overline{q}_{\mathrm{SU(3)}}})$
1	-0.585	-0.355	-0.296
2	-0.607	-0.298	-0.294
3	-0.616	-0.268	-0.295
4	-0.607	-0.275	-0.308
5	-0.575	-0.317	-0.316
6	-0.521	-0.386	-0.323
7	-0.441	-0.470	-0.340
8	-0.704	–	–
9	-0.684	–	–

Table B.12: Correlations for the extracted quark polarisations.

$\langle x \rangle$	$\langle Q^2 \rangle$	$\frac{\Delta u_v}{u_v}$	$\frac{\Delta d_v}{d_v}$	$\frac{\Delta \overline{q}_{\mathrm{SU(3)}}}{\overline{q}_{\mathrm{SU(3)}}}$	χ^2/d.o.f
0.033	1.211	0.189±0.104±0.069	-0.329±0.163±0.175	0.027±0.078±0.043	0.90
0.048	1.459	0.254±0.088±0.043	-0.260±0.145±0.161	-0.013±0.087±0.056	0.65
0.065	1.697	0.256±0.072±0.062	-0.229±0.129±0.152	-0.030±0.096±0.102	0.33
0.087	1.945	0.431±0.068±0.075	-0.162±0.132±0.205	-0.254±0.122±0.140	1.39
0.118	2.220	0.348±0.063±0.057	-0.080±0.132±0.132	-0.168±0.162±0.166	1.21
0.165	2.524	0.358±0.066±0.047	-0.164±0.158±0.149	-0.164±0.276±0.158	0.83
0.238	2.844	0.433±0.069±0.093	0.043±0.200±0.603	-0.557±0.546±0.832	2.51
0.337	3.526	0.487±0.032±0.037	-0.173±0.165±0.285	–	2.54
0.447	4.964	0.668±0.043±0.060	-0.600±0.266±0.153	–	1.11

Table B.13: Extracted valence and sea quark polarisations as a function of x for the SU(3) sea polarisation model.

$\langle x \rangle$	$\langle Q^2 \rangle$	Δu_v	Δd_v	$\Delta \overline{q}_{\mathrm{SU(3)}}$
0.033	2.5	1.679±0.929±0.020	-1.849±0.918±0.032	0.169±0.493±0.007
0.048	2.5	1.947±0.672±0.016	-1.211±0.678±0.035	-0.053±0.357±0.008
0.065	2.5	1.700±0.480±0.027	-0.887±0.500±0.038	-0.080±0.259±0.013
0.087	2.5	2.498±0.396±0.038	-0.515±0.422±0.057	-0.453±0.218±0.016
0.118	2.5	1.709±0.307±0.033	-0.200±0.330±0.039	-0.183±0.176±0.015
0.165	2.5	1.400±0.260±0.031	-0.291±0.279±0.044	-0.093±0.157±0.010
0.238	2.5	1.193±0.191±0.063	0.046±0.211±0.156	-0.125±0.122±0.028
0.337	2.5	0.829±0.054±0.022	-0.092±0.088±0.052	–
0.447	2.5	0.550±0.035±0.023	-0.119±0.053±0.023	–

Table B.14: Extracted valence and sea quark distributions as a function of x for the SU(3) sea polarisation model.

$\frac{\Delta u_v}{u_v}$					
Bin nr.	Frag.	PDF	$P_T P_B$	Δq_{sea}	Other
1	0.0518	0.0046	0.0192	0.0000	0.0046
2	0.0563	0.0066	0.0119	0.0000	0.0036
3	0.0579	0.0079	0.0283	0.0000	0.0022
4	0.0567	0.0086	0.0381	0.0000	0.0041
5	0.0526	0.0087	0.0239	0.0000	0.0021
6	0.0457	0.0081	0.0251	0.0000	0.0026
7	0.0359	0.0070	0.0493	0.0000	0.0039
8	0.0232	0.0052	0.0419	0.0109	0.0060
9	0.0077	0.0028	0.0643	0.0027	0.0079

Table B.15: Contributions to the systematic uncertainty on the exracted $\frac{\Delta u_v}{u_v}$ distribution. "Other" includes contributions from the smearing, radiative and A_2 corrections as well as the uncertainty on $R(x, Q^2)$. See figure 7.7 for futher explanation.

$\frac{\Delta d_v}{d_v}$					
Bin nr.	Frag.	PDF	$P_T P_B$	Δq_{sea}	Other
1	0.0534	0.0736	0.0547	0.0000	0.0860
2	0.0795	0.0721	0.0362	0.0000	0.0683
3	0.1021	0.0689	0.0440	0.0000	0.0706
4	0.1212	0.0640	0.0543	0.0000	0.0531
5	0.1368	0.0574	0.0701	0.0000	0.0536
6	0.1489	0.0491	0.0467	0.0000	0.0583
7	0.1575	0.0390	0.0806	0.0000	0.0642
8	0.1626	0.0273	0.0599	0.5501	0.0485
9	0.1642	0.0138	0.1021	0.3628	0.0961

Table B.16: Contributions to the systematic uncertainty on the exracted $\frac{\Delta d_v}{d_v}$ distribution. "Other" includes contributions from the smearing, radiative and A_2 corrections as well as the uncertainty on $R(x, Q^2)$. See figure 7.7 for futher explanation.

$\frac{\Delta\bar{q}_{sea}}{\bar{q}_{sea}}$					
Bin nr.	Frag.	PDF	$P_T P_B$	Δq_{sea}	Other
1	0.0845	0.0022	0.0052	0.0000	0.0109
2	0.0254	0.0045	0.0098	0.0000	0.0113
3	0.0186	0.0107	0.0151	0.0000	0.0113
4	0.0643	0.0205	0.0135	0.0000	0.0137
5	0.0962	0.0340	0.0147	0.0000	0.0180
6	0.3128	0.0512	0.0116	0.0000	0.0278
7	0.5157	0.0721	0.1745	0.0000	0.0470

Table B.17: Contributions to the systematic uncertainty on the exracted $\frac{\Delta\bar{q}}{\bar{q}}$ distribution. "Other" includes contributions from the smearing, radiative and A_2 corrections as well as the uncertainty on $R(x, Q^2)$. See figure 7.7 for futher explanation.

References

[1] C.G. Callan JR. and D.J Gross, Phys. Rev. Lett., **22** (1969) 156.

[2] M. Gell-Mann, Phys. Lett., **8** (1964) 214.

[3] D. Griffiths 'Introduction to Elementary Particles', Wiley (1987) 272.

[4] M. Gluck, E. Reya, M. Stratmann and W. Vogelsang, Phys. Rev., **D53** (1996) 6100.

[5] V.N. Gribov and L.N Lipatov, Nucl. Phys., **15** (1972) 438.

[6] Y.L. Dokshitzer, Sov. Phys., JEPT **46** (1977) 461.

[7] G. Altarelli, G. Parisi, Nucl. Phys., **B126** (1977) 298.

[8] D. Adams *et al.*, Phys. Lett., **B336** (1994) 125.

[9] K. Abe *et al.*, Phys. Rev., **D58** 112003 (1999).

[10] P.L. Anthony *et al.*, hep-ex/9901006, (1999).

[11] M. Arneodo *et al.*, Phys. Rev, **D50** (1994) 1.

[12] R.K. Ellis, W.J Stirling and B.R Webber, 'QCD and collider Physics', Cambridge (1996) 149.

[13] Particle Data Group, Phys. Rev. **D54** (1996) 1.

[14] D. Adams *et al.*, Phys. Lett., **B412** (1997) 414.

[15] D.L. Anthony *et al.*, Phys. Rev. Lett., **71** (1993) 959.

[16] K. Abe *et al.*, Phys. Rev. Lett., **74** (1995) 346.

[17] K. Rith. Lectures at the workshop 'QCD and Hadron Structure', Kloster Banz (1992).

[18] M. Anselmino, A. Efremov and E. Leader, Phys. Rep., **261** (1995) 1.

[19] J. Ellis and R.L. Jaffe, Phys. Rev., **D9** (1974) 1444.

[20] M.J. Alguard *et al.*, Phys. Rev. Lett., **37** (1976) 1261.

[21] J. Ashman *et al.*, Nucl. Phys., **B328** (1989) 1.

[22] D. Adams *et al.*, Phys. Lett., **B329** (1994) 399.

[23] A. Airapetian *et al*, submitted to Phys. Rev. Lett. hep-ex/9907020 and DESY-99-071.

[24] P.G. Ratcliffe, Phys. Lett., **B109** (1987) 180.

[25] X. Ji *et al.*, Phys. Rev. Lett., **76** (1996) 740.

[26] P.G. Ratcliffe, Proceedings, Spin and polarization dynamics in nucl. and particle phys., Trieste (1988).

[27] M. Arneodo *et al.*, Nucl. Phys., **B321** (1989) 541.

[28] P. Geiger, Doktorarbeit, University of Heidelberg, (1998).

[29] R.D Field and R.P Feynman, Nucl. Phys., **B136** (1978) 1.

[30] B. Andersson *et al.*, Phys. Rep., **97** (1983) 31.

[31] T. Sjostrand, Comp. Phys. Comm., **82** (1994).

[32] H.A.McL. Tallini, Ph.D. Thesis, The University of Liverpool, (1998).

[33] H. Ihssen, Private communication, (1997).

[34] D. Von Harrach, Seventh Int. Workshop on DIS and QCD, Zeuthen, (1999).

[35] The RHIC Design Manual, http://acnsun10.rhic.bnl.gov/NT-share/rhicdm/index.html.

[36] A.A. Sokolov and I.M. Ternov, Sov. Phys. Dokladi, **8** (1964) 1203.

[37] K. Ackerstaff *et al.*, Phys. Rev. Lett, **82** (1999) 1164.

[38] W. Lorenzon HERMES report 95-023.

[39] H. Weidemann, "Particle Accelerator Physics", Springer (1993).

[40] S. Barrow *et al*, HERMES report 96-002.

[41] K. Lee *et al.*, Phys. Rev. Lett. **70** (1993) 738.

[42] K. Lee *et al.*, Nucl. Instr. and Meth. **A333** (1993) 294.

[43] J.Stewart, Seventh Int. Workshop on Pol. Gas Targets and Pol. Beams, Urbana-Champaign, (1997).

[44] C. Baumgarten, SPIN98 - The 13th International Symposium on High-Energy Spin Physics, IHEP, Protvino, Russian Federation (1998).

[45] K. Coulter et al, HERMES Technical Design Report, **DESY PRC90/01** (1990).

[46] K. Ackerstaff *et al.*, NIM **A417** (1998) 230.

[47] W. Wander, PhD thesis, Friedrich Alexander Universitat Erlangen-Nurnberg, (1996). (English translation: HERMES report 97-013).

[48] J. Stenger, Doktorarbeit, University of Erlangen-Nurenberg, (1995).

[49] R. Fernow, Introduction to Experimental Particle Physics, Cambridge, (1986) 178.

[50] J.V. Emerson, B.sc. Thesis, McGill University, (1993).

[51] J. Wendland, MSc Thesis, Simon Fraser University, (1999).

[52] K. McIlhany, Private communication, (1997).

[53] A. Airapetian *et al*, Phys. Lett. **B442** (1998) 484.

[54] N. Akopov *et al*, HERMES report 97-007.

[55] B. Bains *et al*, HERMES report 99-015.

[56] SMC results and systematic errors,
http://na47sun05.cern.ch/results/results_a1.html.

[57] K. Ackerstaff *et al*, Phys. Lett. B (in press),
Eprint numbers: hep-ex/9906035 and DESY-99-048.

[58] M. Ferstl, Doktorarbeit, Fridrich-Alexander-Univ. Erl.-Neurnbergs, (1997).

[59] G. Ingelman, A. Edin and J. Rathsman, DESY report 96-057.

[60] H.L. Lai *et al.*, Phys. Rev.**D55** (1997) 201.

[61] CERN Program Library Long Writeup W5013, CERN (1993).

[62] M. Duren. HERMES report 97-027.

[63] D. Adeva *et al*, Phys. Lett. **B420** (1998) 180.

[64] B.E. Tipton , Ph.D. Thesis, Massachusetts Institute of Technology, (1999).

[65] K. Ackerstaff et al, Phys. Rev. Lett.25, **vol. 81** (1998) 5519.

[66] J.L. Frier *et al*, Phys. Lett. **B244** (1990) 373.

[67] J.L. Frier, Phys. Rev. **C42** (1990) 2310.

[68] M. Lacombe, *et al* Phys. Rev. **C21** (1980) 861.

[69] B. Desplanques, *et al* Phys. Lett. **B203** (1988) 200.

[70] M. Duren, Habilitation, University of Erlangen-Nurenberg, (1995).

[71] M. Duren, Private communication, (1999).

[72] K. Abe *et al*, Phys.Rev. **D58** (1998) 112.

[73] W.H. Press *et al*, Numerical Recipies in C, Cambridge University Press (1995).

[74] T. Gehrmann and W.J. Stirling, Phys.Rev. **D53** (1996) 4775.

[75] M. Göckeler, *et al* Phys.Rev. **D53** (1996) 2317.

[76] J. Ellis and M. Karliner, hep-ph/9601280.

[77] M.A. Funk, PhD Thesis, Hamburg University, (1999).